Applied Research Laboratory

Technical Report

A Switchable Magnetic Low-Index Metamaterial for Use in a Dynamically Reconfigurable Beam-Scanning Lens Antenna With a Single Feed

by

Jeremiah P. Turpin, Dr. Douglas H. Werner and Dr. Douglas E. Wolfe

PENN STATE

1 8 5 5

The Pennsylvania State University
The Applied Research Laboratory
P.O. Box 30
State College, PA 16804

A Switchable Magnetic Low-Index Metamaterial for Use in a Dynamically Reconfigurable
Beam-Scanning Lens Antenna With a Single Feed

By

Jeremiah P. Turpin and Dr. Douglas E. Wolfe

Technical Report No. TR 14-008
December 2014

REPORT DOCUMENTATION PAGE

Form Approved
OMB No. 0704-0188

1. REPORT DATE (DD-MM-YYYY)	2. REPORT TYPE	3. DATES COVERED (From - To)
06-18-15	Technical Report	December 14-June 2015

4. TITLE AND SUBTITLE	5a. CONTRACT NUMBER
A Switchable Magnetic Low-Index Metamaterial for Use in a Dynamically Reconfigurable Beam-Scanning Lens Antenna With a Single Feed	
	5b. GRANT NUMBER
	5c. PROGRAM ELEMENT NUMBER

6. AUTHOR(S)	5d. PROJECT NUMBER
Jeremiah P. Turpin	
Douglas E. Wolfe	5e. TASK NUMBER
	5f. WORK UNIT NUMBER

7. PERFORMING ORGANIZATION NAME(S) AND ADDRESS(ES)	8. PERFORMING ORGANIZATION REPORT NUMBER
Applied Research Laboratory The Pennsylvania State University PO Box 30 State College, PA 16804	TR 14-008

9. SPONSORING/MONITORING AGENCY NAME(S) AND ADDRESS(ES)	10. SPONSOR/MONITOR'S ACRONYM(S)
Defense Advance Research Projects Agency Tactical Technology Office 675 N. Randolph Street Arlington, VA 22203-2114 Attn: Kevin Massey	DARPA
	11. SPONSOR/MONITOR'S REPORT NUMBER(S)

12. DISTRIBUTION/AVAILABILITY STATEMENT
Approved for Public Release: distribution unlimited

13. SUPPLEMENTARY NOTES

14. ABSTRACT
See attached

15. SUBJECT TERMS

16. SECURITY CLASSIFICATION OF:			17. LIMITATION OF ABSTRACT	18. NUMBER OF PAGES	19a. NAME OF RESPONSIBLE PERSON
a. REPORT	b. ABSTRACT	c. THIS PAGE			Douglas E. Wolfe
Unclassified	Unclassified	Unclassified	UU	153	19b. TELEPHONE NUMBER (include area code) 814-865-0316

The Pennsylvania State University

The Graduate School

A SWITCHABLE MAGNETIC LOW-INDEX METAMATERIAL

FOR USE IN A DYNAMICALLY RECONFIGURABLE

BEAM-SCANNING LENS ANTENNA WITH A SINGLE FEED

A Dissertation in

Electrical Engineering

by

Jeremiah Paul Turpin

Submitted in Partial Fulfillment

of the Requirements

for the Degree of

Doctor of Philosophy

December 2014

The dissertation of Jeremiah Paul Turpin was reviewed and approved* by the following:

Douglas H. Werner
Professor of Electrical Engineering
Dissertation Advisor

Pingjuan Werner
Professor of Electrical Engineering

Victor Pasko
Professor of Electrical Engineering

Douglas Wolfe
Associate Professor of Material Science and Engineering

Kultegin Aydin
Professor of Electrical Engineering
Department Chair

*Signatures are on file in the Graduate School.

Abstract

Metamaterials and Transformation Optics (TO) have been used to design and implement many novel electromagnetic devices that can achieve effects not possible using conventional materials. Compact high-gain antennas are one of the more popular and successful emerging applications for the new TO and metamaterial design approaches. This dissertation details an extension of uniaxial near-zero-index metamaterial lenses through the incorporation of a tunable or reconfigurable metamaterial as a replacement for the static metamaterial of the original antenna.

A design is presented for a beam-scanning TO lens that allows an arbitrary number of beams at controlled magnitudes to be dynamically synthesized from a single omnidirectional source, unlike the equivalent antenna constructed using an array. A cylindrical slab of zero-index magnetic metamaterial controls the radiation pattern by altering the effective shape of the lens through switching of selected regions 'off' to emulate free-space conditions. A design for a switchable metamaterial is presented that allows for digital control over its bulk properties, from near-zero-index to near-free-space at the targeted operational frequency. Extensive modeling and simulations were performed for the design of the lens and metamaterial and during the analysis of measurement results. Initial prototypes of the tunable metamaterial were fabricated and characterized to confirm the original measurements, and the design updated to incorporate the measured data. These measurements were performed using custom test fixtures manufactured specifically for this project. Finally, a simplified prototype lens was manufactured and characterized in an anechoic as a proof-of-concept for the design.

This dissertation presents the lens and metamaterial specifications, as well as the design process and considerations that were determined for practical tunable and reconfigurable metamaterials. Although the focus is on the particular example of the beam-scanning reconfigurable antenna, the analysis and modeling methods presented here are applicable to any reconfigurable metamaterial application.

Table of Contents

List of Figures

xi

Acknowledgments

My largest thanks go to my advisor, Dr. Douglas Werner. As my thesis advisor, my dissertation could quite literally not have been finished without his approval and signature, but his advice and support have been invaluable throughout my time in graduate school. Thank you for being a strong mentor to me, both as a scientist and as a manager and principal investigator, and always challenging me to do more and better than I could before. Your example as a scientist, researcher, and professor have been instrumental to my own professional development.

Dr. Pingjuan Werner is responsible for my pursuit of a Ph.D., rather than leaving for industry with my Master's degree. Thank you, Ping, for pushing me to stay for my Doctorate, even after I had initially declined. I am grateful for your friendship, and your forceful and accurate advice.

I wish to thank Clinton Scarborough for being such a good friend both before and during graduate school. Our discussions on technical topics have been invaluable, even though we rarely worked on the same projects. I have leveraged his company countless times to sound out new ideas and to refine my own thoughts through conversation.

I thank Lloyd Scarborough for our lunch conversations together with Clinton which have ranged through all areas of science, politics, religion, and philosophy, and in general gave an excellent break in the middle of the day from thinking about simulations or antennas.

I am grateful for the excellent undergraduate education that I received at Grove City College, and for the dedicated professors who pushed us so hard to succeed. Thank you to Dr. Timothy Mohr, Dr. Mike Bright, and Dr. William Birmingham for encouraging me to apply to graduate school. In particular, I thank Dr. Cavicchi for his extremely challenging and under appreciated senior classes; those classes laid a strong foundation for my future graduate classes, but I could only appreciate their true value several years after completion. I also thank my friends Johnathan Jessen, Clinton Scarborough, Jeff Kiser, and Jason Okerman for the many hours during homework sessions and projects that we encouraged and competed with

one another; that atmosphere of strong collegial competition was very valuable to me.

Dedication

This dissertation is dedicated to my wife, Caitlin, for her continued love and support throughout my time at Penn State. Thank you for your time, patience, and for your occasional demands for me to stop working so hard, even though it seems as though I never really listened to those.

But supposing, as is generally supposed, vector algebra is something "awfully difficult," involving metaphysical considerations of an abstruse nature, only to be thoroughly understood by consummately profound metaphysicomathematicans, such as Prof. Tait, for example. Well, if so, there would not be the slightest chance for vector algebra and analysis to ever become generally useful; and I should not be writing this, nor should I have, for several years past, persisted in using vector algebra in electromagnetic theory-a prophet howling in the wilderness. It will readily be concluded, then, that I believe that the vector analysis is going to become generally used in scientific work, and that what is needed is not "awfully difficult." There was a time, indeed, when I, although recognizing the appropriateness of vector analysis in electromagnetic theory (and in mathematical physics generally), did think it was harder to understand and to work than the Cartesian analysis. but that was before I had thrown off the quaternionic old-man-of-the-sea who fastened himself on my shoulders when reading the only accessible treatise on the subject—Prof. Tait's Quaternions. But I came later to see that, so far as the vector analysis I required was concerned, the quaternion was not only not required, but was a positive evil of no inconsiderable magnitude; and that by its avoidance the establishment of vector analysis was made quite simple and its working also simplified, and that it could be conveniently harmonized with ordinary Cartesian work. There is not a ghost of a quaternion in any of my papers (cxcept in one, for a special purpose). The vector analysis I use may be described either as a convenient and systematic abbreviation of Cartesian analysis; or else, as Quaternions without thc quaternions, and with a simplified notation harmonizing with Cartesians. In this form, it is not more difficult, but easier to work than Cartesians. Of course you must learn how to work it. Initially, unfamiliarity may make it difficult. But no amount of familiarity will make Quaternions an easy subject. [...] "Quaternion" was, I think, defined by an American schoolgirl to be "an ancient religious ceremony." This was, however, a complete mistake. The ancients—unlike Prof. Tait—knew not, and did not worship Quaternions.

—Oliver Heaviside, Electromagnetic Theory, Vol. I, April 10, 1899, pp. 134, 136.

Chapter 1

Introduction and Previous Work

With traffic congestion increasing on popular terrestrial microwave communication bands, the development of reconfigurable antennas is quite compelling due to the possibility of placing pattern nulls or peaks at desired locations in real time so as to reduce interference, power consumption, and system complexity. Every aspect of radio and communication technology, except for the antenna, has been greatly advanced in recent years through the application of inexpensive high-speed computing technology, which allows digital circuitry to replace more and more of the expensive analog RF devices within a system. An increasing fraction of the analog and RF hardware within radios is being replaced by digital signal processors, and "Software Defined Radio" aims to use digital signal processing in the place of conventional final transmitter power amplifiers and receiver filters. These changes make the entire communication system more flexible by removing the physical design constraints of limited space for multiple RF front-ends. "Smart Antennas" have been imagined, but not yet implemented, to serve as a more dynamic component of such a communication system. With features such as automatic interference rejection, beam-scanning to focus energy on other stations so as to reduce power and increase battery life, dynamic frequency adjustment, and (of course) allowing for compact and lightweight implementation, such a "smart antenna" would indeed make an enormous impact on the widespread application of radio and microwave communication technology.

Reconfigurable antennas and electromagnetic devices provide frequency, channel, and/or application diversity within a system. Whether constructed using

deformable geometry [1], tunable circuit elements [2], or the interaction of multiple feeds (array antenna), making small changes to the system configuration can be designed to have a large change in the resulting behavior. Adding configurable material properties to this list of options significantly increases the range of achievable responses. Spatially-reconfigurable materials offer even stronger benefits, as selectively changing the material parameters throughout the structure effectively offers simultaneous control over both the geometry and the material parameters.

Materials and geometry form an inseparable pair when working with electromagnetic devices; wave propagation is affected by both materials and their geometric interfaces. The design of antennas, waveguides, filters, and resonators consists of a material forming a specialized geometry in order to create a prescribed electromagnetic field behavior in either the time or frequency domains. Until the advent of metamaterials, geometry could be considered the more useful of the two tools, as the designer would only have absolute control over the geometry of a design, not the media; materials with natural properties could be combined in various ways, but a medium with arbitrary electromagnetic properties could not, in general, be synthesized. Ultimately, however, materials and geometry are generally equivalent in capabilities - any field pattern or EM behavior may be implemented in different ways depending on the selected structure and media. Tuning or deforming a geometrical structure may be corrected by adjusting the material properties of the device, and vice versa.

The introduction of metamaterials to the electromagnetics community has provided engineers with new analysis and design tools that have been proven useful for solving difficult problems. The field of antenna design, in particular, has been greatly enriched by the influx of new ideas, with metamaterials being used to enhance gain [3] and bandwidth [4]–[7], reduce antenna size [8]–[10], and construct new types of collimating lenses [11]–[13]. Although the ideal smart antenna has not yet been constructed, Metamaterials and Transformation Optics (TO) [14], [15] offer electromagnetics engineers new tools for the development of such a technology in stages. This dissertation describes the development of a dynamic, reconfigurable metamaterial lens that allows complex beam steering and control over the azimuthal-plane radiation pattern, thus making progress towards satisfying one aspect of the "Smart Antenna" design problem.

Metamaterials are collections of subwavelength structures engineered to create interesting electromagnetic interactions, often enabling properties without parallels in natural materials. Although the science of metamaterials is still developing, many applications have been proposed or demonstrated where their use facilitates some kind of novel behavior. In particular, the design techniques that have been introduced by Transformation Optics (TO) [14] rely on the use of metamaterials for the construction of novel devices within which EM waves may be controlled with a high degree of design flexibility. Application of TO and metamaterial-based devices to antennas for the augmentation of the radiation performance or reduction of antenna dimensions is a productive field of current research. Metamaterial lenses designed with TO techniques have been presented for use in compact, high-gain [16], [17] and multibeam [3], [18] antennas. The general inhomogeneous and anisotropic material parameters required by the TO material specification equations can for some designs be reduced to much simpler structures, including implementation by homogeneous slabs of uniaxial zero-index metamaterials (ZIM) [17]. The infinite effective phase velocity within a homogeneous ZIM slab with an embedded excitation source leads to near-uniform phase and amplitude at the exterior faces of the medium. Using metamaterial and Transformation Optics technology, lenses can be constructed that allow the number, direction, and relative strength of the beams to be chosen arbitrarily during lens design through the appropriate selection of the lens shape. Each face of the lens acts as a radiation aperture and produces a collimated beam with directivity relative to the face size. These antennas offer an alternative beamforming technique with some advantages over conventional antenna arrays, as all of the beams from the lens are driven by a single feed without requiring complex multielement phase-shifting and impedance-matching networks.

Prototypes of selected metamaterial lenses have confirmed the predicted performance and thereby validated the TO/metamaterial design method [3], [17], [19] and the use of metamaterial lenses for antenna pattern control. However, the radiation pattern of these lenses is fixed during design and fabrication, limiting the usefulness of these TO-based metamaterial antennas compared to conventionally-designed dynamic phased arrays. Conventional phased array antenna systems are electrically steerable and capable of producing nearly arbitrary beam patterns with

high gains, given a sufficient number of elements. Arrays are not always suitable, though, for the cost and feed structure complexity increase rapidly with the size of the array. Reflector antennas such as parabolic dishes can also generate beams with very high directivity and may be mechanically manipulated for real-time beam scanning, also with a single feed. Unfortunately, the possible scan rate is limited by the mechanical actuators and such systems will generally be limited to a single beam for each reflector or feed. An electrically-scanned antenna (compared to mechanically-steered reflectors or other radiators) would be much better for high-speed adaptive communication, radar, and sensing systems. In comparison to arrays and reflector antennas, the single feed required for a multibeam metamaterial lens is attractive, but the static radiation pattern greatly limits their application.

The game-changing innovation is a reconfigurable TO lens that is based on advanced tunable metamaterial technology and high-efficiency magnetic antennas to enable novel beam-scanning behavior. The previously described collimating ZIM lens examples can be modified to create a dynamic beam-steering lens that can form and scan an arbitrary number of beams in real time through the use of tunable or switchable metamaterials. This innovation pushes the state-of-the-art in metamaterials technology to allow the effective shape of the lens to be controlled with state changes of blocks of metamaterial unit cells. The metamaterial may be constructed using printed circuit board techniques more inexpensively than the precision RF phase-shifters or independent transceivers for a phased array. In the same way as the shape of the static ZIM antenna determines the number and relative intensity of the radiated beams, tuning regions of the dynamic TO lens between near-ZIM to near-free-space conditions can change the beam count, strength, and direction. With the potential to replace adaptive phased arrays in many applications due to the ease of control and simpler feed structure, the reconfigurable TO metamaterial lens is an exciting development.

Reconfigurable metamaterials alter their effective bulk electromagnetic properties in response to external stimuli, and have found applications in antennas, transmission-line devices, free-space filters, and more [20]. The ability to change the material properties (permittivity, permeability, anisotropy, dispersion) of a constituent material within some structure is a novel capability that is only just

now starting to be widely applied. One could consider using a material with controlled dielectric constant as the substrate of a patch antenna, or setting the focal length of a dielectric lens by varying the refractive index in real time.

Tunable radio-frequency (RF) metamaterials have been previously demonstrated using MEMS switches, varactor and PIN diodes, structural changes, or liquid crystal as the active component [21]–[23]. The previously published techniques and mechanisms are, however, unsuitable for a large, spatially-tunable array of resonators. The trouble when constructing a large slab of an actively-controlled metamaterial is apparent when power and control signals must be provided to each unit cell. For a lens to allow arbitrary beam configurations, individual control is required over each unit cell or at least small groups of unit cells. Wireless control and power is impractical, which leads to the requirement that wires or printed circuit board (PCB) traces be used to interconnect each metamaterial element. The presence of metal traces within a metamaterial structure may alter the desired EM field interactions, and must be accounted for within the design so as to minimize the effect on the desired metamaterial operation. Since long circuit traces will primarily interact with the electric field, using a magnetic metamaterial can reduce the effect of any detrimental interactions. Also, the polarization of the feed antenna and the orientation of the metal traces can be chosen so as to further minimize the interactions with the electric field.

High-speed beam scanning (5 μs beam switching, potentially less) is enabled by the complete lack of moving parts; all control and scanning is enabled by solid-state digital electronics. The design can be adapted to the frequency, directivity, power, and switching speed requirements of an individual application. The reconfigurable lens described in this dissertation combines the multi-beam dynamic scanning capability of phased arrays with the power over wave propagation granted by TO techniques. Combining state-of-the-art metamaterials, magnetic antennas, and TO designs promises to produce exciting results in the near future.

1.1 Reconfigurable Antennas and Limitations

Reconfigurable antennas provide frequency, spatial, and functional diversity for their host systems by dynamically altering their behavior and performance in re-

sponse to a control signal or the environment. The addition of tunable elements [24] or materials [25], [26] to a base structure can vary the input impedance or current distribution to adjust the resonant frequency [27] or radiation pattern [28] to meet real-time requirements. For this work, dynamic control over the radiation pattern (direction and number of high-directivity beams) is the primary motivation. Although this goal can be met in antennas with single feeds, such as reflectors, patch, and wire antennas, phased arrays can be considered as the most capable of the pattern-reconfigurable antennas. An array with a large enough number of elements can be used to generate an almost arbitrary radiation pattern, subject to frequency limitations and the overall physical size of the array. However, the required phase delay and power division circuits or independent transceivers for each array element add complexity and expense to a system, which can be difficult to justify in many cases. The best examples of single-feed pattern-reconfigurable antennas offer much less beamforming capability; such antennas will either offer a small number of beam configurations, or in the case of the reflector, may direct a single beam in arbitrary directions a mechanically-limited slew rate. An antenna that combined single-feed topology with the arbitrary pattern control of a large phased array would have many advantages for the construction of inexpensive, high-performance communication systems. Metamaterial-based reconfigurable transmitarray [29] or reflectarray [30] antennas demonstrate this desirable behavior, but both examples are based around end-fire operation; azimuthal scanning would not be supported.

1.2   Metamaterials

Because of the myriad interactions of matter with electromagnetic waves, materials are vitally important to the field of electromagnetics. The unique properties of new dielectrics and material substrates have been used to create better lenses, antireflective coatings, radar-absorbing coatings, and more efficient antennas. Even the rapid development of material science cannot work miracles, and even the most advanced materials will be limited in their properties and applications by what nature has provided. Engineering some composite material, homogeneous or inhomogeneous, to meet specific electromagnetic performance constraints can

be a greatly superior option to simply selecting a material from a library of available products. An inhomogeneous engineered material that may be characterized in its electromagnetic interactions as possessing some effective electric permittivity and magnetic permeability created through the use of structures arranged in a specific geometric pattern is called a metamaterial. Metamaterials derive their properties from their subwavelength structure, not the material composition alone. Electromagnetic metamaterials are quite useful tools for the development of new antennas, filters, waveguides, transmission lines, and lenses, allowing more compact, broadband, and potentially low-loss operation. Although still in the early stages of development, metamaterials show great promise for influencing designs and common practices for all of electromagnetics.

A metamaterial is a structure composed of a collection of artificial engineered molecules designed to behave as a homogeneous material within some frequency band of interest with electromagnetic wave interactions that are uncommon or impossible to achieve with an ordinary 'real' material. A structure defined in this way emulates the electromagnetic field interactions with actual materials, where the atomic, molecular, and inter-molecular resonances and interactions determine the response of a material to an electromagnetic impulse, as illustrated by Fig. 1.1(a). Most metamaterials use periodic arrays of identical molecules for simplicity of analysis and construction, where the molecules are macro-sized structures that are still much smaller than a wavelength at the desired operational frequency band. Since the periodic structures are on a macro scale, the electromagnetic field is clearly inhomogeneous inside the metamaterial. However, the fields may be homogenized for analysis and design by using small unit cells, thus allowing the wave interactions of the electromagnetic field and the metamaterial to be approximately specified by an effective electric permittivity and magnetic permeability as in Fig. 1.1(b). Although metamaterials are considered here only for electromagnetic waves, they may also be defined and constructed for other physical systems governed by wave equations, such as surface waves on a liquid [31] and longitudinal acoustic waves [32], [33].

The work detailed in this dissertation deals only with metamaterials in the microwave band. Metamaterials for applications in the terahertz, infrared, and optical bands would use different materials and fabrication techniques than dis-
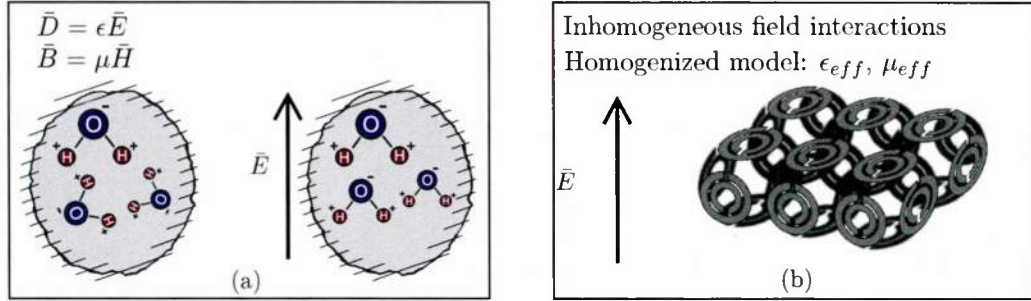
Fig. 1.1: (a) The electromagnetic interactions of a real material can be expressed in terms of a relative ϵ_r and μ_r. (b) The structures that compose a metamaterial, although larger than the molecular and atomic-scale effects of a real material, can, in many circumstances, be used to compute an averaged electromagnetic response and the assignment of an effective ϵ_r and μ_r.

cussed here, and must be considered separately. Although, to a basic approximation, an RF metamaterial could be simply scaled in size to work similarly at either extremely short or very long wavelengths, practical considerations prevent this from being a reasonable design strategy. It is, in general, not possible to find optical materials with equivalent properties to those in the RF, and the fabrication tolerance, precision, and considerations are completely different. At low frequencies (below several hundred megahertz), the size of the unit cells becomes large, and it becomes physically challenging to construct an electrically large metamaterial device. The microwave frequency range is convenient for metamaterials, and tunable metamaterials in particular, since the length scales are amenable to standard printed-circuit board fabrication techniques, and measurements may be conveniently performed.

Although academic metamaterial research has begun recently within the last 10-15 years, there are more isolated examples of metamaterial-like devices much earlier. Wire-mesh plasma media, which can be considered a precursor of modern metamaterials, were introduced as grids for antenna beam collimation by W. E. Kock in 1946. A group at the Stanford Research Institute [34] designed and constructed a Luneburg lens-type device from a wire-mesh structure in 1961. Many metamaterial applications grew out of advances in artificial photonic band-gap (PBG) structures; although photonic or electromagnetic band-gap (EBG) materi-

als are generally not considered to be metamaterials, there are similarities in their design and construction.

The Split Ring Resonator (SRR) was introduced by Pendry et. al. [35] and almost immediately seized upon by the metamaterial community at large as a valuable building block for the creation of magnetic metamaterials, including negative-index (left-handed materials) [36], [37] and zero-index materials [3]. Several examples of published SRR designs are included in Fig. 1.2.

Although the SRR is the probably the single most widely used metamaterial element, it is only used as a magnetic-field-coupled element. One common electric metamaterial element is the Electric LC resonator (ELC), introduced by Schurig et. al. [38], which has replaced the wire mesh medium for some negative-index material implementations [37]. The Complementary SRR (CSRR) [39] and the volumetric End-Loaded Dipole (ELD) [17] elements are also electric-field coupled elements. These elements are also depicted in Fig. 1.2.
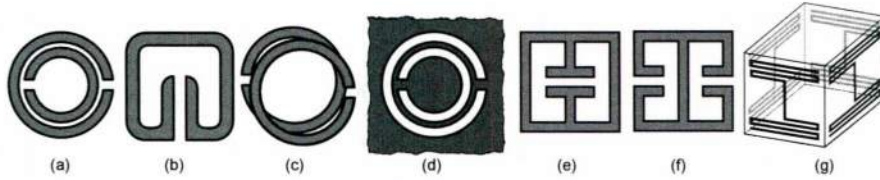
Fig. 1.2: Various metamaterial unit cell designs from the literature (a) Original Pendry SRR [35] (b) Schurig SRR [38] (c) Marques SRR [40] (d) CSRR [39] (e) Single-capacitor ELC [38] (f) Dual-capacitor ELC [37] (g) Volumetric end-loaded dipole [17]

For the reconfigurable lens antenna, a near-zero uniaxial permeability condition is required, for which an SRR array modified with tuning structures is well suited. A zero-permeability lens (rather than a zero-permittivity lens) is selected so that the control traces inherent to such a tunable design would minimally interact with the desired field vector. Although the SRR has been primarily presented as a negative-index resonator, Negative Index (or left-handed) metamaterials (NIMs) will also possess Low-Index Metamaterial (LIM) properties at a higher frequency. While NIMs operate in the resonance region where the permittivity and permeability are simultaneously negative, a ZIM/LIM implementation will function in the high-frequency resonance tail near the zero-crossing of the resonance, where

the absorption losses are low and greater bandwidth is achievable. This approach was used to design the meta-liner presented in [4] to achieve octave bandwidth and negligible loss, as well as for the design of a broadband TO multi-beam focusing lens [3].

1.3 Transformation Optics

The transformation optics (TO) design methodology allows for unprecedented flexibility in creating new electromagnetic and optical devices. Introduced in [14], [41], the technique relies on the form-invariance of Maxwell's equations under a spatial coordinate transformation. Maxwell's equations, when evaluated under a transformed coordinate system, are valid and their solutions can be interpreted in the original coordinate system as solutions of the equations with permuted material parameters $\bar{\bar{\epsilon}}_r(x, y, z)$ and $\bar{\bar{\mu}}_r(x, y, z)$. Given a desired field behavior described by a coordinate system transformation, the permittivity and permeability can be determined for a physical structure within which the waves will propagate according to the transformation. The required permittivity and permeability are computed as

$$\bar{\bar{\epsilon}}_z = \frac{A \bar{\bar{\epsilon}}_\omega A^T}{|A|} \tag{1.1}$$

$$\bar{\bar{\mu}}_z = \frac{A \bar{\bar{\mu}}_\omega A^T}{|A|} \tag{1.2}$$

where A is the Jacobian matrix corresponding to the transformation from the $\omega-$ to the $z-$domain (the transformed domain). The permittivity and permeability gradients in the transformation medium force the electromagnetic fields to behave as though they were subject to the desired spatial mapping.

The electromagnetic cloak is one of the most well-studied applications enabled by the new transformation optics techniques [42]–[45], but other novel devices have been considered including beam collimators and shapers, field concentrators, and ideal far- and near-field focusing lenses [15], [46]–[48]. A specialization of the near-field focusing lens converts a diverging cylindrical wavefront to a highly directive collimated plane-wave beam [3], [18], [49].

Despite the recent advances in metamaterial design and synthesis, most of the existing transformation optics designs remain firmly in the realm of academic exercises, with material parameters too complex to implement practically. Applications of the transformation optics design techniques have typically led to highly anisotropic and inhomogeneous solutions for the required permittivity and permeability of a device. Some papers have studied the effects of simplifying the material parameters for easier fabrication, such as the electromagnetic cloaks explored in [50], [51] but these approximations often lead to significantly degraded performance. Another approach leverages transformation techniques to reduce the size of simply-shaped near-field focusing lenses through basic transformations that are easier to implement [52]. Others have chosen quasi-conformal or conformal transformations to minimize either the anisotropic or inhomogeneous elements of the required material [51], [53] in order to maximize the practicality of the design.

TO designs that can be easily constructed using simple metamaterials or an all-dielectric gradient-index (GRIN) profile, both of which may be implemented using current technology and support a reasonable bandwidth of operation, are possible in some cases through approximating the results of a more complex transformation. However, it can be better to restrict the allowable class of transformations to those that naturally create the desired characteristics. Using a conformal or a quasi-conformal mapping (qTO) as the transformation instead of transforming between arbitrary coordinate systems as allowed by the general TO procedure produces a material specification that may be implemented by an all-dielectric GRIN device [54]. The all-dielectric GRIN lenses are inherently wideband, unlike metamaterial-based approaches, and can be designed such that any material dispersion that is present is used to perform color-correction for a wavelength-independent response. Although (quasi)-conformal mappings in the complex plane are inherently 2D, 3D GRIN lenses may also be designed by rotating a lens profile through a cylindrical region or stacking the gradients of multiple qTO mappings in sequence.

1.4 Metamaterial and Transformation Optics-based Antennas

A variety of metamaterial-enhanced antennas have been introduced in the literature with a number of interesting features, such as improving bandwidth [5], increasing gain and effective area [3], [17], reducing undesired inter-element coupling [55], and reducing the antenna profile [56] compared to more conventional implementations. High-gain small-volume metamaterial antennas in particular have seen many successful demonstrations. For high-gain antenna purposes, most lens designs have operated in the low-index or near-zero-index metamaterial regime rather than rely on the extremely narrowband negative-index response of the perfect optical imaging lenses. The zero-index metamaterial (ZIM) lenses have broader bandwidth than might be expected for a resonant structure because the devices are tuned to operate in the tail of the resonance where the slope of the permeability or permittivity vs. frequency is small. The selection of the specific ZIM resonators can assist in broadening the bandwidth, as well. In general, ZIM-based designs use a metamaterial lens or superstrate above or surrounding a feed antenna in order to increase the effective aperture efficiency and thus improve the gain. In this way, the application of metamaterials allows the use of a simpler and more compact feed antennas which in other circumstances might require a much larger aperture or the implementation complexity of an array.

Examining the various RF lens designs that make use of uniaxial metamaterials and zero-index materials in particular, several broad categories may be inferred; the geometries of these categories are illustrated in Fig. 1.3. In the first two cases, the antenna is embedded in the metamaterial, which commonly has an homogeneous or graded effective low index of refraction or behaves as an artificial plasma medium [16], [18], [57]–[59]. Alternatively, the metamaterial layer or slab may be used as a collimating superstrate placed over some feed antenna[60]–[64] (Fig. 1.3(c)). All methods have been used with purely metamaterial or FSS designs as well as with the general inhomogeneous TO approach. Most of the antennas that have actually been constructed use homogeneous materials, or at least roughly homogeneous materials, simply for simplicity of fabrication. Of course, simulations are not limited by what would be convenient to construct, and regularly make use

of complex anisotropic and inhomogeneous materials.
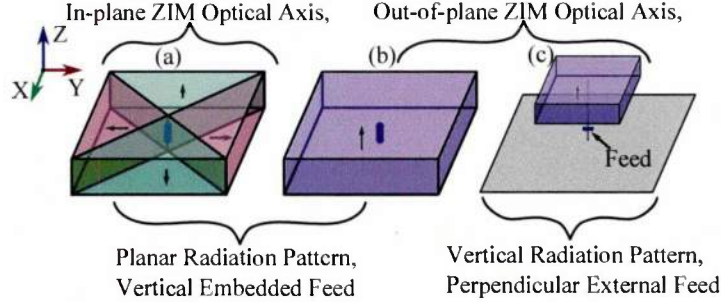
Fig. 1.3: Illustration of three categories of Uniaxial ZIM lens antennas. In these antennas, either the permeability or the permittivity, but not both, are near zero and are uniaxial with the optical axes aligned as indicated by the arrows drawn within each region. (a) Parallel (in-plane) optical axis to direction of propagation and planar beamforming with a vertical feed; radiation pattern controlled by optical axis. (b) Perpendicular (out-of-plane) optical axis to direction of propagation and planar beamforming with a vertical feed; radiation pattern controlled by shape of ZIM slab. (c) Parallel (out-of-plane) optical axis to direction of propagation and vertical beamforming with a horizontal feed and ground plane; radiation pattern controlled by optical axis and feed properties.

Most Transformation Optics-based collimating lenses, such as those proposed by Kwon and Werner [11], [15], [47], [49], [65], will demonstrate extreme inhomogeneity and anisotropy unless specifically designed otherwise. The goal of the collimating transformation is the conversion of a cylindrical or spherical phase profile to a planar (or nearly-planar) phase profile. This is most commonly accomplished through the explicit transformation of a some circular or spherical surface to a planar surface and applying simplifications to the resulting material map to allow fabrication [6], [18], [49].

Uniaxial near-zero-index metamaterials have been used in several different collimating lens implementations. Analyzed as a homogeneous slab with effective permeability and permittivity extracted from the unit cell response, near-ZIM lenses have interesting properties for antenna design. A wave propagating inside an isotropic slab with near-zero refractive index will have a near-infinite phase velocity and near-infinite wavelength. The infinite effective wavelength indicates that the behavior of a device of any finite size would operate in a quasi-static

way; the metamaterial lens itself has zero effective electrical size, and the phase is uniform within the structure and across all outer faces. The uniform phase across the surface generates radiating plane waves at each surface, resulting in high-directivity beams. The extreme impedance mismatch between such a material slab and free space will reduce its efficiency as an antenna unless a matched magneto-dielectric metamaterial or some other impedance matching mechanism is implemented, however. Isotropic metamaterials are challenging to construct; uniaxial structures are much more convenient, due to the geometry and orientation of most common resonant unit cells.

Uniaxial ZIM metamaterials are typically constructed with either magnetic [3]] or electric [7] resonators to minimize the fabrication complexity, but occasionally both [17], [66] are required. Metamaterials with magnetic, electric, and combined magneto-electric near-zero material parameters each have their uses, as well different orientations of the optical axis. Depending on the orientation of the incident waves, the effective index is either near-zero, if the field vector is aligned with the optical axis of the metamaterial, or near-free-space, if the field vector is normal to the optical axis. Such metamaterial slabs offer two collimation modes for metamaterial antennas. The first (perpendicular mode, [13]) functions the same as the isotropic lens by propagating the waves in the plane perpendicular to the optical axis, such that the metamaterial slab behaves as a ZIM. The second (parallel mode) propagates the wave parallel to the optical axis, such that the waves experience a near-free-space matched index and are unaffected by the ZIM properties. Waves that are not exactly parallel to the optical axis are refracted towards the optical axis by the anisotropic near-ZIM component of the slab, demonstrating a collimating effect.

When considering a thin slab of uniaxial ZIM embedded in free space, it can be analyzed as an angular-selective filter - plane wave components at near-normal incidence are transmitted, but waves incident at angles greater than some cutoff are reflected. Lenses operating in the perpendicular mode will use an embedded feed antenna to reduce the effects of the impedance mismatch, but parallel-mode lenses will generally have an acceptable impedance match by their construction, and so operate well with either embedded or external antennas, behaving respectively as a dielectric resonator or a collimating dielectric lens. Uniaxial ZIM lenses as

described above have been used to demonstrate beamforming in high-directivity single-beam end-fire configurations [7], [17], [66] as well as for arbitrary multi-beam operation [6], [13], [67], through an appropriate choice of optical axis and excitation polarization.

Using the perpendicular mode for beam collimation, where the optical axis is perpendicular to the direction of wave propagation, allows flexibility in selecting the radiation pattern by forming a one-to-one mapping between the geometry or shape of the lens and the resulting radiation pattern. However, the poor impedance match of the perpendicular mode can limit the bandwidth of such a lens due to the resonant effects required to achieve radiation, despite the wideband near-zero-index metamaterial properties.

Directing the optical axis of either a uniaxial zero-permeability or zero-permittivity metamaterial parallel to the direction of wave propagation presents a good impedance match to the feed antenna [3], [6], [7]. Combining both zero permeability and permittivity enhances the off-axis performance of the lens to form more better beams when used with symmetric feeds, and enables use as a superstrate antenna over multiple polarizations, forming a Fabry-Pérot cavity [17], [68]. These metamaterial lenses can operate over relatively wide bandwidths of 20% or more, based on the inherent wideband properties of near-zero index materials and the near-matched index of the metamaterial, which prevent the need for strong resonance effects for efficient operation.

Out of the described options, only the antenna with excitation polarization parallel to the optical axis is suitable as the base design for a reconfigurable planar-beamforming lens. Unlike the first and third examples from Fig. 1.3, only the second option has complete control over the in-plane radiation pattern merely by altering the shape of the homogeneous, uniaxial slab [13]. Although deforming the physical lens in real time without perturbing the refractive index is not practical, the same effect can be achieved by altering the effective medium properties of subregions of the lens. Switching subregions between low- and high-index states changes the effective shape of the ZIM lens, enabling beam scanning. Conveniently, this scanning approach allows each unit cell to be switched in a binary fashion between two states. Control over the material properties in continuous or any more granular fashion would require a higher degree of tuning and bias signal

complexity.

Array antennas do have an advantage in that, with the addition of phase and magnitude control circuitry to the feed lines, the radiation patterns can be reconfigured for nearly arbitrary beam scanning. The radiation patterns of the previously introduced metamaterial antennas are fixed during design, with no capability for dynamic reconfigurability. This limitation restricts the possible applications for which these metamaterial antennas may be targeted.

1.5   Original Contributions of This Work

The original contributions of this work to the fields of electromagnetics, metamaterials, and reconfigurable antennas are described in the following list.

- Designed a volumetric reconfigurable metamaterial unit cell that is capable of being tiled to form an arbitrarily-sized metamaterial panel without detrimental effects due to the tuning and control circuitry.

- Studied different options for distributing control signals for a spatially-reconfigurable volumetric metamaterial.

- Modeled and confirmed behavior of metamaterial with all control and biasing circuitry.

- Measured the behavior of the metamaterial unit cells with included control and biasing networks.

- Created control circuitry for independent spatial control over the state of each metamaterial unit cell.

- Integrated metamaterial and system-level constraints to produce design synthesis rules for spatially-reconfigurable metamaterial lens antennas.

- Developed design for azimuthally-scanning electrically-controlled metamaterial lens antenna.

- Extended lens antenna design to support elevation-plane scanning with multiple uniform phase and magnitude feeds.

Chapter 2

Reconfigurable Metamaterial Lens Antenna

Extending the previously mentioned metamaterial antennas through the use of a switchable or tunable metamaterial can allow for a beam-scanning antenna system. Such a structure may be implemented as a cylindrical anisotropic near-zero-index metamaterial (ZIM) slab in which regions of the slab may be independently switched from ZIM back to dielectric or near-free-space properties. A uniaxial zero-index metamaterial (ZIM) slab can collimate energy from an embedded source when the E-field (H-field) is polarized parallel to the zero-permittivity (zero-permeability) optical axis [13], [69], [70]. In this collimation mode, only the shape of the slab and the relative position of the feed to the face determine the number, relative magnitude, and direction of the beams. Contrasted with the parallel ZIM collimation mode, where the direction of the optical axis determines the direction of radiated energy, the perpendicular mode is more flexible for construction of a reconfigurable lens, as illustrated in Fig. 2.1. Single-dimensional control (effective index magnitude) is simpler to achieve than dual-axis control (direction of optical axis in the plane).

As described in [13], the physical shape in the azimuthal plane of a uniaxial ZIM slab determines the resulting radiation pattern, as a single high-directivity beam will be radiated from each face of the lens. Wider faces, as they present a larger aperture, produce a higher-directivity beam. In addition, the beam strength from each face is inversely proportional to the relative distances of the faces from

the feed point. Changing the effective shape of the lens by switching the material state of specific regions so as to change the location and length of the facets of the near-zero-index slab then changes the radiation pattern.

This chapter focuses on the design of the metamaterial lens itself, and assumes the use of homogeneous effective material parameters in simulations and analyses. Since the exact metamaterial design affects the lens specification and vice versa, some of the metamaterial design characteristics and considerations are briefly described or summarized in this chapter. A detailed discussion of the spatially-reconfigurable metamaterial design and related considerations is included in Chapter 3.
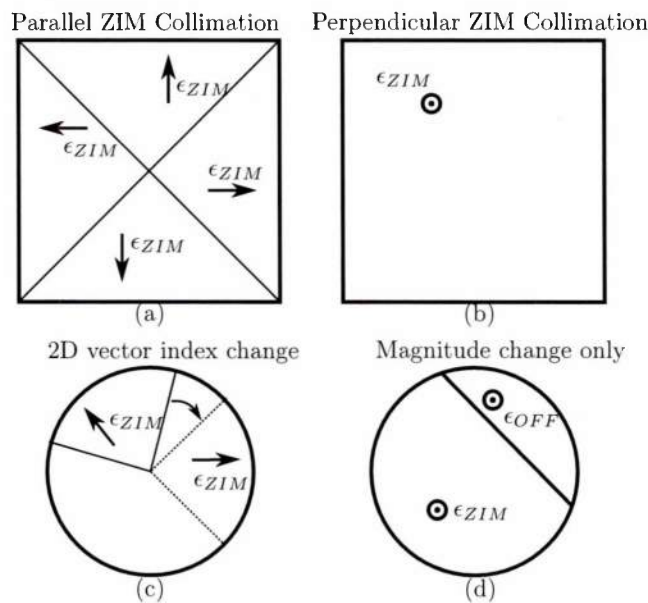
Fig. 2.1: (a) The parallel ZIM collimation mode requires the direction of the optical axis to be changed (c) in order to change the direction of beam propagation, requiring two dimensions of control over the index. (b) The perpendicular ZIM mode requires only an on-off, one-dimensional control over the index (d) to change the shape or boundary contour of the lens in order to change the radiation pattern.

2.1 qTO-derived near-ZIM lens

The lens design begins with the near-zero-index uniaxial TM-mode lens introduced in [13] (Fig. 2.2 and Fig. 2.3). This lens used an electric near-ZIM implemented by a wire-mesh metamaterial with a single dipole feed. For this lens, the extraordinary axis of the metamaterial is oriented in the z-direction, parallel to the E-field and normal to the direction of wave propagation. For single-polarization operation, waves in the material behave as though the structure is isotropic. The number and relative magnitude of the beams are determined by the shape of the lens; a beam radiates from each planar face of the lens. The possible radiation patterns using this lens design principle are shown in Fig. 2.2 and Fig. 2.3, and a rendered diagram of the zero-permittivity plasma-type wire-mesh metamaterial lens is shown in Fig. 2.4.

(a)　　　　(b)　　　　(c)　　　　(d)
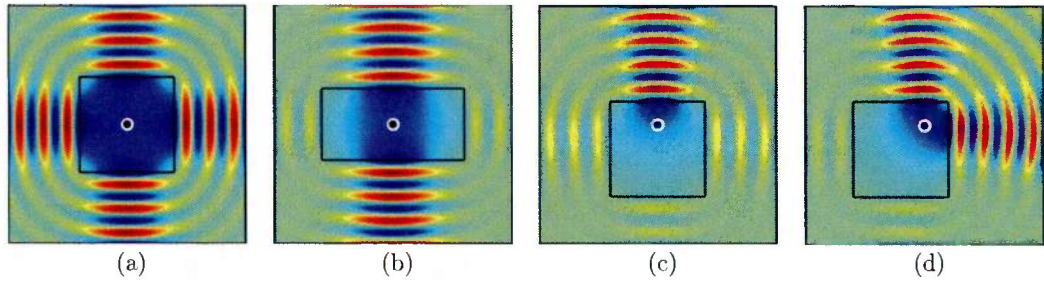
Fig. 2.2: Changing the lens dimensions changes the radiation pattern.

(a)　　　　(b)　　　　(c)　　　　(d)
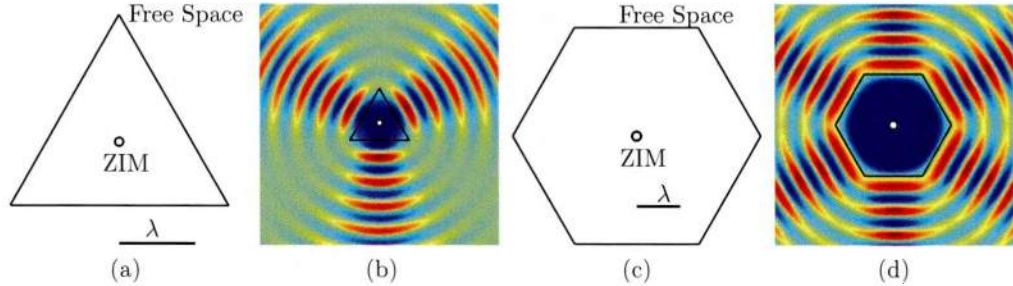
Fig. 2.3: A beam is radiated from each face of the structure. Sufficiently large lenses can successfully resolve beams at small angular increments.
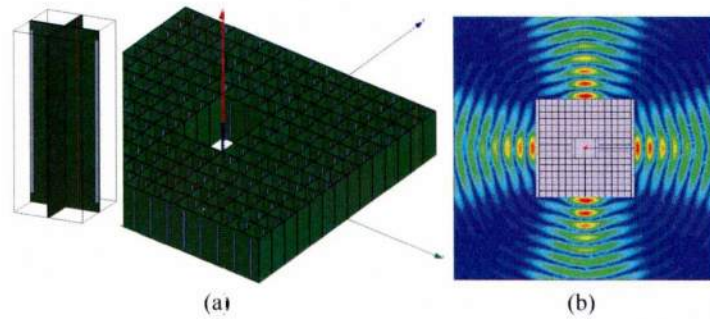
Fig. 2.4: Early simulation of a wire-mesh dipole array near-zero index metamaterial lens.

As discussed previously, the lenses in Fig. 2.2 and Fig. 2.3 have a radiation pattern that is fixed at design time, but the design concept may be extended to allow reconfigurability. Instead of changing the physical shape of the lens to control the beams, a reconfigurable metamaterial could be used to change the effective shape of the lens. ZIMs are narrowband (although quite broadband when considering other metamaterial structures), resonant metamaterials; a small change in an internal impedance of the unit cell, perhaps caused by a state change in a MEMS switch or varactor diode, is capable of shifting the resonance frequency away from the lens operational band so that the metamaterial behaves in a quasi-free-space mode. Selectively switching exterior regions of the lens 'on' and 'off' between ZIM and near-free-space conditions changes the effective shape of the ZIM subregion of the lens and, thus, the number and magnitude of the beams, as illustrated in Fig. 2.5 [69]. In this example, a switch is opened in the middle of each wire-mesh unit cell in an outer rectangular region of the lens to eliminate the ZIM resonance, thus creating a face closer to the feed of the lens and enhancing the radiation from that face compared to the other sides. With a dynamically-switchable z-oriented anisotropic ZIM metamaterial controlled in real time, only on/off control for each pixel of the lens is required to allow completely dynamic control of the effective lens shape.

A cylindrical slab composed of a reconfigurable metamaterial that may be switched between near-free-space and near-ZIM conditions is ideal for a dynamically controlled lens, since the symmetry of the structure allows equivalent oper-
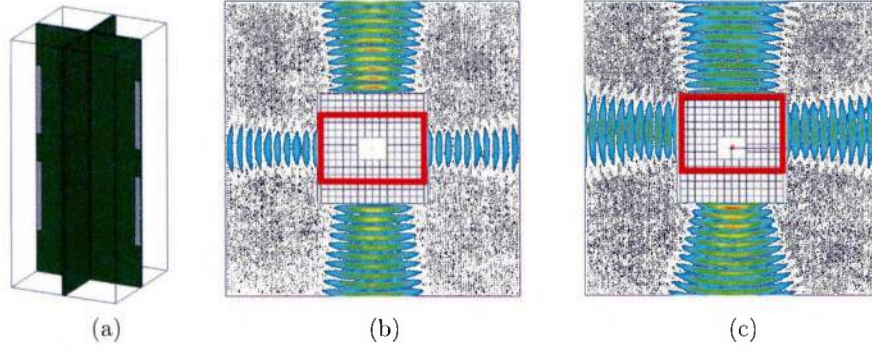
Fig. 2.5: Introducing an switch into the metamaterial array and opening the switch in different regions of the metamaterial successfully reconfigures the radiation pattern.

ation in any direction. The diagram in Fig. 2.6 shows the tuning concept for a cylindrical lens, which with a spatially reconfigurable metamaterial may be set to generate one, two, or more independent beams.
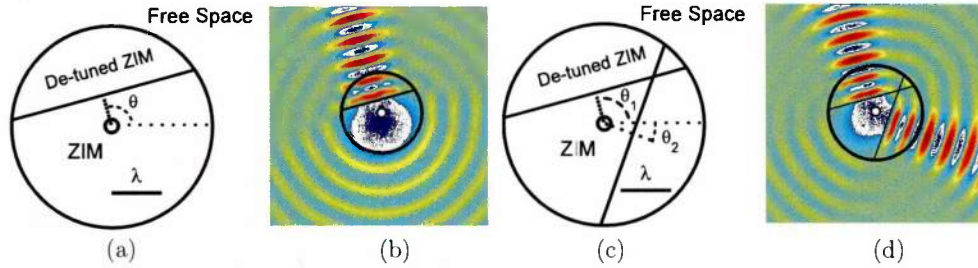
Fig. 2.6: Using a cylindrical, reconfigurable ZIM slab allows for beam scanning.

2.2   Cylindrical magnetic lens

When using a lens with finite thickness (instead of the infinite thickness assumed by 2D simulations [17], [68]) then the lens becomes a dielectric resonator that requires the dimensions and exact value of permeability or permittivity to be selected to promote a radiating mode rather than an internally resonant mode. Some choices of dimensions (r,h) and material parameters will produce a non-radiating dielectric resonator instead of an antenna, but these modes may be eliminated through

proper design. Fig. 2.7 shows the difference between these two modes; the two field plots show the effects of small changes in geometry (the radius and thickness of the lens in Fig. 2.7(b) are 7% larger than those in Fig. 2.7(a)). The physical change in dimensions can also be interpreted as a change in frequency, which affects the available operational bandwidth of the antenna independent of any dispersion in the material properties. The dimensions for a radiating mode are dependent on the material geometry and the effective material parameters of the metamaterial in both on and off states; as the effective index increases significantly above zero, the behavior of the lens degrades. Larger lenses that provide higher directivities also require that the refractive index remains small throughout the operating band. This places an effective limit on the usable bandwidth of the lens, due to the index dispersion of the metamaterial. PEC plates are required at the top and bottom of the lens to form an additional mode constraint against the parallel ZIM collimation mode which would generate strong axially-directed beams, as illustrated in Fig. 2.9. These geometrical constraints on the size of the lens for good operation at a given frequency, along with the narrow bandwidth of a metamaterial implementation, will limit the overall operating bandwidth of the reconfigurable lens.
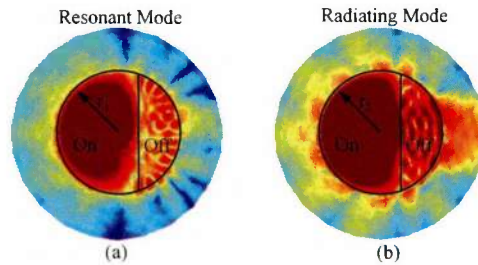
Fig. 2.7: Magnitude plots of the fields within finite reconfigurable ZIM lenses with PEC top and bottom plates (Fig. 2.9) and (a) dimensions are selected to create an internally resonant mode. (b) dimensions are selected to create a radiating mode.

2.2.1 Material Parameters

For the purposes of design using a bulk metamaterial lens simulation, some assumed material parameters must be selected. The uniaxial, dispersive permittivity and permeability used in the selection of the appropriate lens dimensions and in

simulations are provided in (2.1) and (2.1), where $\mu_{zz}(f)$ in the on and off states is defined in Fig. 2.8.

$$\bar{\bar{\epsilon}} = \begin{bmatrix} 2.5 & 0 & 0 \\ 0 & 2.5 & 0 \\ 0 & 0 & 1 \end{bmatrix} \qquad (2.1)$$

$$\bar{\bar{\mu}} = \begin{bmatrix} 1 & 0 & 0 \\ 0 & 1 & 0 \\ 0 & 0 & \mu_{zz}(f) \end{bmatrix} \qquad (2.2)$$
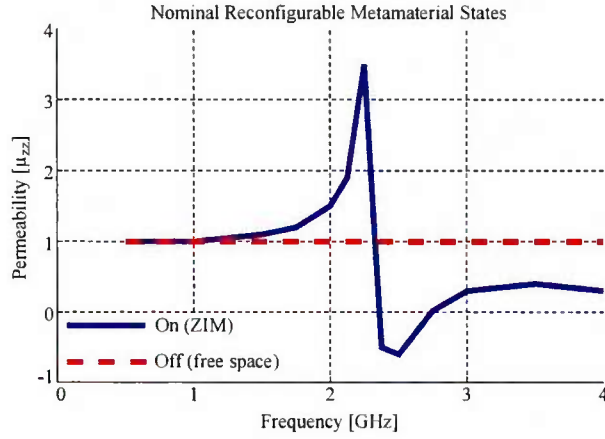
Fig. 2.8: Extraordinary uniaxial component of permeability used in lens simulations for the on and off states.

2.2.2 Design Process

Designing the lens by parameter study has been the most effective technique. The maximum refractive index is specified by the expected metamaterial dispersion, and selecting a desired directivity drives the initial selection of the radius and thickness of the lens to meet the required aperture size. Initial simulations are performed with non-dispersive material properties until the resonance is located at the operational frequency, at which time the dispersive materials may be applied to gauge the effect on operational bandwidth, radiation pattern, and impedance

characteristics. The lens height and radius are then adjusted together until a reasonable operating mode is achieved, considering the input impedance, radiation pattern, and the bandwidth. Operational bandwidth of the reconfigurable metamaterial lens antenna is not expected to be large since the desired behavior is only available by overlapping multiple narrowband physical effects (dielectric resonator, feed antenna, dispersive material). A possible improvement to the bandwidth may be achieved by allowing tuning of the metamaterial ZIM band across the lens via the externally-applied global bias levels; the instantaneous bandwidth would remain narrow, but the channel frequency could be shifted within a more reasonable range.

A spatially-tunable metamaterial implemented using printed circuit board (PCB) technology will require interconnections and control signals passing between unit cells as electrically long traces, complicating the design of the metamaterial. Any extraneous metal within the lens will tend to distort the local fields and possibly degrade the quality of the desired focusing effect. To minimize the effects of the control traces, this lens uses magnetic metamaterial and magnetic dipole feed, the dual design to the previously proposed reconfigurable structure [13]. The effects of the magnetic metamaterial will be less affected by the long, electrically-connected traces, which would primarily affect the electric field. Simulations of the lens can use an electrically-small loop as an approximation to a magnetic dipole source, but the final lens will employ an efficient TE10 source, such as the electrically-small magnetic dipole antennas introduced in [71], [72] or a magnetic slot antenna.
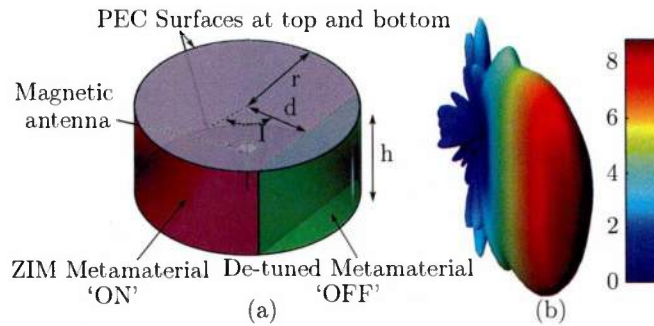
Fig. 2.9: (a) Model illustrating lens construction using tunable ZIM slab with PEC plates at top and bottom. (b) Directive fan-shaped radiation pattern [dB] for r = 1.8λ, h = 0.48λ, and d = 0.6λ.

2.2.3 Excitation Considerations

The reconfigurable lens antenna in the perpendicular mode requires that the excitation be aligned with the optical axis of the metamaterial. For a magnetic metamaterial, a vertically-polarized magnetic dipole source is required. When using the vertically-polarized magnetic field with a vertically-oriented magnetic current excitation, image theory allows the insertion of a vertical ground plane through the middle of the lens without changing the lens behavior. Using a half-cylindrical lens rather than a full cylinder restricts the beam scanning range, but also simplifies the construction and implementation details for the metamaterial as well as the feed antenna. An additional approximation may be made for the sake of simpler design by replacing the half-cylinder by a half-hexagon. A hexagonal (or half-hexagonal) outline is convenient for unit cells in a periodic hexagonal close-pack arrangement, and is an acceptable approximation to the symmetric cylindrical lens. Nominal device geometries of a full cylindrical lens, half-cylindrical lens, and half-hexagonal lens are illustrated in Fig. 2.10. Representative radiation patterns using the dispersive, anisotropic material parameters defined above at different scanning angles from the half-hexagonal lens (Fig. 2.10(c)) are shown in Fig. 2.11.

2.2.4 Metamaterial Selection

Dynamic, non-passive non-mechanical spatial control over the material properties is the largest challenge for the implementation of a reconfigurable volumetric metamaterial, since the control circuits cannot be simply hidden behind a ground plane, as for a reconfigurable metasurface or reflective/absorptive FSS. Since the metallic control traces will affect the response in any case, the metamaterial must be designed so as to minimize their effects on its desired operation. The use of a magnetic metamaterial simplifies the design of the reconfigurable elements, since planar loops may be created using printed circuit board (PCB) technology. Using an array of split-ring resonators (SRR) where RF switches are placed in the gaps and controlled by an array of shift registers creates a metamaterial that can be spatially tuned. The spatial reconfiguration requires that control traces propagate throughout the lens to distribute data and power to the control circuits and set the metamaterial state at all locations within the lens. The switch properties and
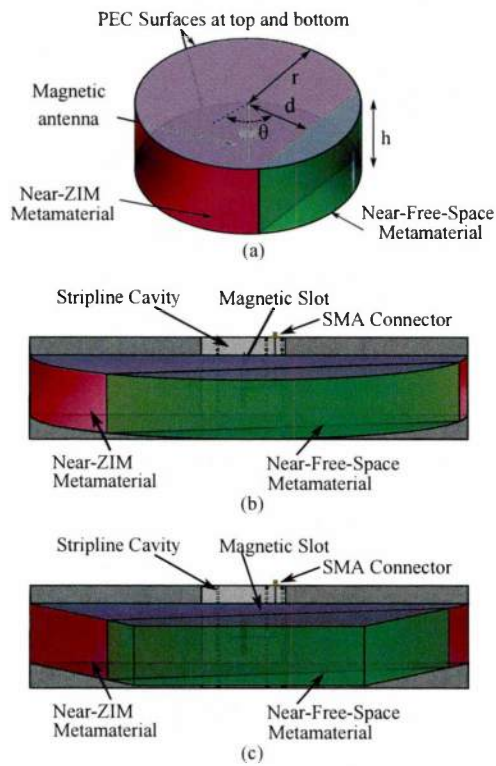
Fig. 2.10: (a) Cylindrical lens magnetic loop feed with 360 degree azimuthal coverage. Restricting 180 degrees of azimuthal scanning allows reduction of the design to either a (b) half-cylindrical lens with magnetic slot feed or a (c) half-hexagonal lens with magnetic slot feed.
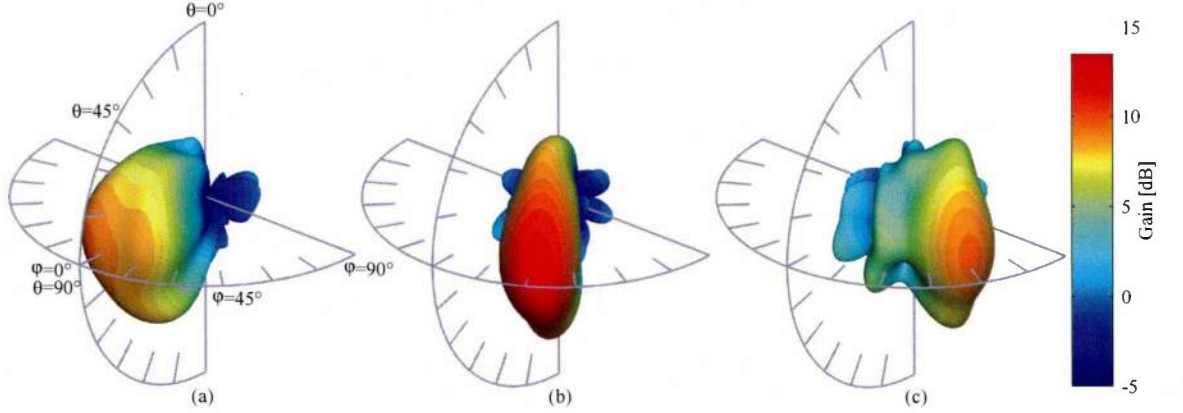
Fig. 2.11: Representative three-dimensional gain patterns at 2.7375 GHz of the reconfigurable lens steered to (a) $\phi = 0$ deg, $\phi = 30$ deg, and $\phi = 60$ deg. Each example shows a narrow, high-directivity beam centered at the desired scanning angle, with a broad-fan-shaped elevation-plane pattern.

SRR dimensions are chosen to induce a strong magnetic resonance just below the desired operating band when the varactor is in one state and to eliminate the resonance for the other. Operating at a frequency just above the resonance yields a low-index, near-ZIM effective medium due to the Lorenzian permeability response of the SRR. A metamaterial prototype satisfying these requirements is described below.

An array of wire loops loaded with lumped capacitance or inductance in the plane of the lens produces a magnetic response that may be trimmed to resonance by the loop dimensions, substrate properties, and lumped element values. It is desirable for the number of lumped elements in the design and the control traces to be minimized to reduce their effect on the metamaterial response.

2.2.5 Control Signal Distribution Topology

A hexagonal spiral control signal topology was selected over several competing topologies for distributing the required control signals throughout the lens based on several design constraints. These design constraints are specifically based on metamaterial implementations in the low microwave range (1-4 GHz) that assume self-contained planar metamaterial panels with some small number of control signal

inputs, where feature sizes in the design are limited by standard planar PCB manufacturing capabilities. At lower frequencies (100-500 MHz), where individual unit cells may be several centimeters large, then the relative size of the control traces becomes small relative to the metamaterial, and many of these constraints may be weakened. At higher frequencies, different fabrication techniques may be necessary, which also changes the possible trace sizes, switching methods, and materials. The ultimate constraint on the control circuitry is that it minimally affect the desired metamaterial response and that all unit cells throughout the lens be tunable. That constraint may be decomposed into the following more specific requirements:

- Minimize the number of control traces and the PCB area which they cover

- The control signal distribution topology should be as homogeneous as possible, so that the number of special-case unit cells to be designed and implemented are minimized.

- The board area and number of components used by the control circuitry should be minimized.

- The effect of the control circuitry on the beamforming should be independent of the direction or magnitude of beam scanning.

- The control traces must reach every unit cell in the lens.

- The control signal topology must be extendable for simple construction of different-sized reconfigurable metamaterial slabs.

Several options or general design strategies may be applied to ensure that these constraints may be met. The requirement for the control traces reaching every unit cell implies, combined with the requirements for homogeneous topology and minimal control trace area, that some form of sparse, space-filling curve is required. Sharing control circuitry between adjacent unit cells as much as possible also reduces the required trace density over the case where each unit cell has independent circuits.

Considering a Cartesian distribution of unit cells, as in the conventional meta-material, leads to a rectangular grid or table configuration of control signals; however, such a situation does not allow for a cylindrical (or other non-rectangular) lens to be easily constructed as there is no logical control signal path that allows for near-isotropic behavior, and such a situation would not appear isotropic for beam scanning in different directions away from ninety-degree increments. A cylindrical lens with Cartesian unit cell distribution is illustrated in Fig. 2.12(a).

Several options appear when considering a distribution of unit cells in polar coordinates, including radial and spiral control traces.

Radially-propagating TE^R/TM^R waves in cylindrical coordinates have no field components in the radial direction, which would imply that radially-directed wires for control traces would not greatly affect the beam propagation. However, the goal of the cylindrical lens is to convert from a cylindrically-propagating wave into a plane wave, which is no longer TE^R/TM^R at all locations within the lens. A radial control signal distribution also presents logistical problems with the varying unit cell densities; it is not possible for a single radial control line to give control signals to all unit cells within any finite angular sector for an arbitrarily-size lens. For this reason, the number of control traces would increase rapidly for larger lenses, and the control trace density would be much greater at the center than the outside of lens, affecting the homogeneity of the metamaterial response. For these reasons, radially-directed control traces were not considered further; such a configuration is shown in Fig. 2.12(b).

Cylindrically-distributed unit cells can be uniform, but not periodic. As illustrated in Fig. 2.12(c), such a configuration is possible, but requires out-of-plane wiring or jumps between rings to introduce the control signals throughout the lens.

Control traces that form a spiral space-filling curve around the lens have several desirable features for construction of a control system for a reconfigurable metamaterial slab. Although such traces are tangential to the wave propagation and guaranteed to interact with either the electric or magnetic field, they have the advantage of at least approximate rotational symmetry; beams directed in any direction through a cylindrical lens would see approximately the same environment, as far as the control traces are concerned. Logarithmic spirals, similarly to radial distributions, don't allow for uniform unit cell distributions throughout the

lens due to the nonequal spacing between the spiral arms. Archimedean spirals may be selected, however, that have uniform spacing between adjacent lines, so that unit cells throughout the lens could be nearly identical and approximately uniformly distributed. Using an Archimedean spiral would allow equi-spaced unit cells throughout the lens. In either case, a spiral would require the curvature of the control traces within each unit cell to be adjusted based on the radial distance of each unit cell from the origin, making the design more complex. Fig. 2.12(d) and Fig. 2.12(e) show spiral unit cell distribution patterns.
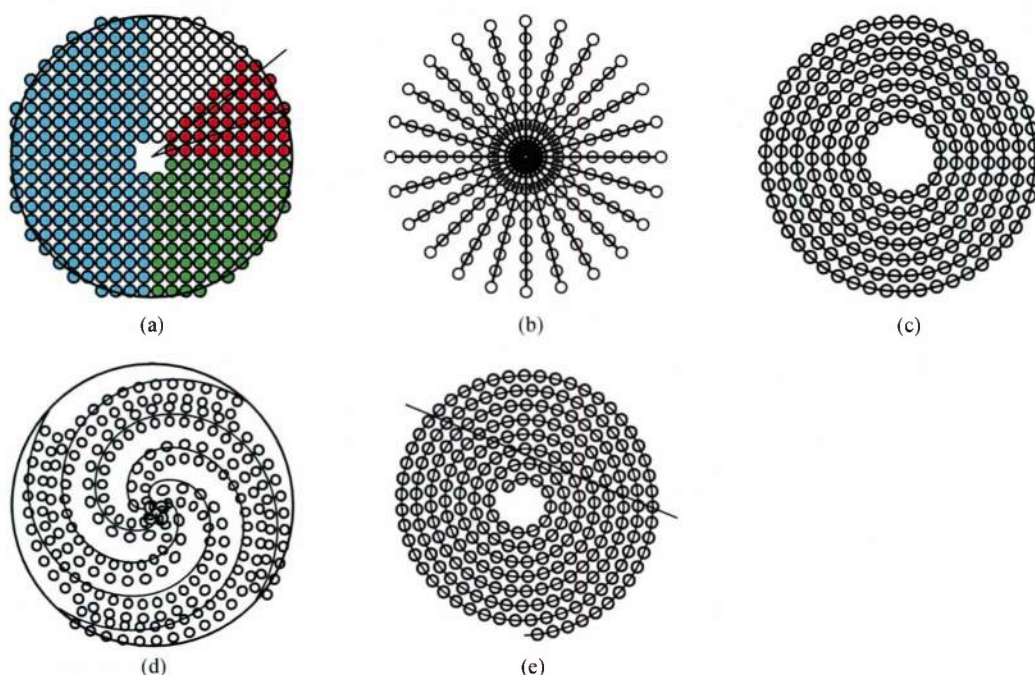
Fig. 2.12: (a) Unit cells distributed in a Cartesian grid do not have a logical and extendable control signal distribution method. (b) Radially-directed control signals cannot be used to control uniformly-distributed unit cells. (c) circular control traces are possible, but signals must be introduced independently to each closed ring. (d) Care must be taken with any spirals to be sure that uniformly-spaced unit cells may be implemented. Logarithmic spirals, in particular, leave nonuniform gaps between adjacent lines (e) Carefully-designed Archimedean spirals can construct uniform distributions of unit cells, but in this configuration, no sharing of control circuitry is possible, and control traces are relatively dense.

The hexagonal spiral is the best implementation. It has the advantages of the spiral curves over Cartesian or radial unit cell and control signal distributions in that chained hexagons can be treated as a space-filling curve with one or a low number of starting points. The advantage over logarithmic or constant-curvature spirals is that the distribution of unit cells when tiled hexagonally is uniform and periodic, although non-rectangular. Only two unit cells are required to be designed: a hexagonal element with parallel input and output signal lines, and a hexagonal element with input and output signal lines offset by 60 degrees. Finally, multiple unit cells (six is a logical choice for a hexagon) may be grouped to form a single hexagon and share some of their control and switching circuitry, thus reducing the relative percentage of the board consumed by control circuitry relative to that used by metamaterial. The hexagonal design pattern is shown in Fig. 2.13.

Since each ring resonator should be independently controlled and addressable, using an array of shift registers treated as a series-to-parallel converter is a good implementation choice. The resonators with their associated switches were grouped into hexagons in sets of six to share an 8-bit shift register, of which 1 bit is unused, and 1 bit serves as the input to the next cascaded unit cell. The hexagonal unit cells (hexes) were cascaded in a hexagonal spiral in order to provide power, data, and clock lines to each unit cell. In this configuration, every loop is individually addressable to allow for arbitrary tuning of the effective shape of the lens. Fig. 2.13 shows the design concept of hexagonal groups of split-ring resonators tiled into a spiral for propagating control and data signals throughout the lens.

2.3 Possible Feed Antennas

The original ZIM lens examples used an electric dipole or monopole source with a Z-oriented wire mesh electric metamaterial that was infinitely periodic in the vertical direction. A magnetic metamaterial and feed antenna were chosen as the most practical solution for a tunable lens, since the magnetic field would not be as affected by extraneous control traces as would an electric metamaterial. The topology of typical magnetic metamaterials is more convenient for manufacturing, as well, since a Z-oriented magnetic metamaterial may be constructed using continuous, horizontal PCB panels, without the requirement for wine-crate-type
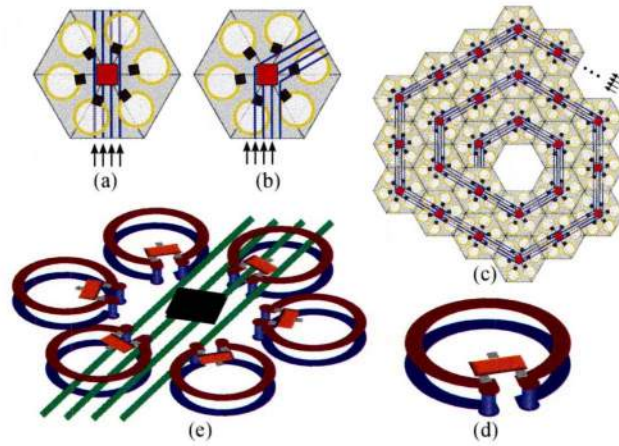
Fig. 2.13: Preliminary vision for lens metamaterial implementation (a) Straight and (b) angled hex cell designs. (c) Hexagonal unit cell tiling as an approximation to a circular cylinder. (d) Dual-loop stacked SRR with common-cathode varactor. (e) Hex unit cell model with control traces included.
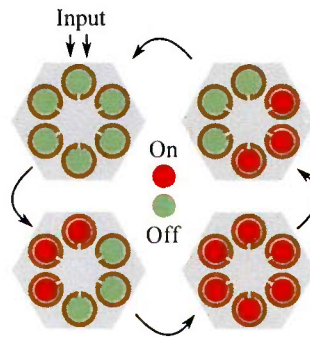
Fig. 2.14: Operation of hexagonal unit cells with shift registers for controlling split-ring resonator states.

assembly and more complex control circuitry as would be necessary for an electric metamaterial implementation.

An electrically-small electric dipole radiates a TM-mode wave. An equivalent magnetic antenna would radiate a TE-mode wave. The typical example of a magnetic dipole antenna would be the electrically-small loop, but these are inefficient and difficult to feed properly. Homogeneous lens simulations performed in HFSS have used a simple electrically-small magnetic loop antenna placed in a small air cavity as the feed, which is simple to model but a very poor radiator with low efficiency, and only serves as a loose approximation to a magnetic dipole antenna. Electrically larger loops do not have a magnetic dipole pattern, since phase variations will be present over the loop and directional radiation will occur. The radius of a loop antenna must be less than $\lambda/6$ (6 mm @ 2.4 GHz) to maintain a primarily magnetic-dipole pattern, and although the radiation resistance and radiation efficiency may be increased by using a multiple-turn loop or a ferrite core, these options also increase the winding resistance and loss of the antenna. The only redeeming factor of the electrically-small loop for simulations is the modeling simplicity. However, this low-efficiency antenna would be replaced in a prototype lens by a more efficient and flexible TE-mode magnetic dipole antenna such as the Folded Slotted Spherical Helix[71], Spherical Split-Ring antenna [72] or an aperture slot antenna [73].

The Spherical Split-Ring (SSR) antenna consists of a vertical stacked array of split-ring resonators with spherically-tapered radii and splits that alternate orientations by 180 degrees with each layer. The antenna is excited by a circular center-fed dipole along the circumference of the containing sphere. The independent feed and radiating structures mean that the radiation and impedance characteristics of the antenna may be tuned roughly independently, making this antenna a good choice for radiating to the electrically hostile environment of a zero-index slab. The antenna may also be implemented using planar traces on stacked printed circuit boards, allowing a simple avenue for fabrication.

Magnetic slot antennas will also produce a magnetic dipole TE-mode radiation pattern with relatively high mode purity. A bidirectional slot antenna would be functional for a full cylinder, and if a half-cylinder of magnetic metamaterial is backed by a PEC ground plane, then a single slot antenna would be sufficient.

A substrate-integrated waveguide (SIW)-fed slot antenna may be a good option, due to the ease of construction and the degree of control allowed over the fields, compared to a slotted ground plane antenna fed by an open-circuit microstrip line.

2.4 Vertical scanning

Although the cylindrical lens can perform beam scanning only in the azimuthal plane, the fan-shaped radiation pattern with broad elevation-plane coverage would allow multiple independent reconfigurable ZIM antennas to be stacked together to form an array with beamforming capability. In this simple array, the feeds for each element would be fed with identical magnitude and phase, and the scan direction controlled only by the spatial configuration of the metamaterial in each slab. Fig. 2.15(b) illustrates a three-element vertical array of ZIM slabs, where the off-state metamaterial regions are chosen to create an angled effective aperture that produces the directive radiation pattern in Fig. 2.15(d). The beamforming is accomplished through changes in the metamaterial settings alone. Since the three elements are fed with identical phase, and the ZIM has an effectively infinite phase velocity, the difference in switching radii between the three elements introduces the phase offset required for phased-array beamforming. Note that for this array, no phase-delay circuitry is required, only a fixed equal-phase corporate feed network. Representative elevation- and azimuthal-plane scanned radiation patterns for the three-element system are illustrated in Fig. 2.16. The broad elevation-plane element pattern yields a 60° field of view with only 2.5dB squint, as shown in Fig. 2.17. The metal plates on top and bottom of the elements, which would seem to constrain the off-normal performance, actually help by broadening the elevation-plane element pattern, thus yielding a wider available scanning range. Additional vertical scanning range may be achieved by increasing the number of lens elements and/or changing the resonant characteristics of the individual lenses to make them shorter, and thus broaden their elevation-plane radiation pattern.

The metamaterial lens may be inexpensively constructed using PCB technology, which offers a great deal of design flexibility. This lens is superior to existing metamaterial lenses in that the radiation pattern is not fixed at the design stage, and may be competitive in performance and capabilities with conventional phased
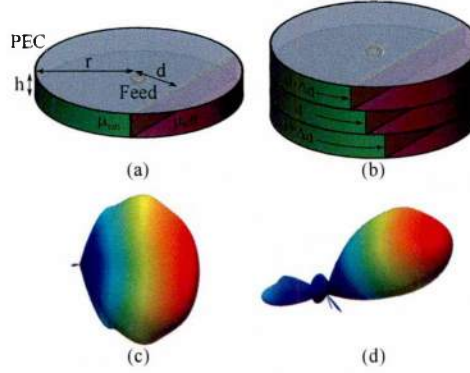
Fig. 2.15: (a) Cylindrical ZIM slab with PEC bounding plates forming a reconfigurable lens antenna. The left (green) region of the lens is in a ZIM state, and the right (purple) in a near-free-space state. (b) Stack of three reconfigurable lenses with the switching radii of the lenses adjusted for beam scanning. (c) Directivity pattern [dB] of the cylindrical metalens. (d) Directivity pattern [dB] of the stacked array of cylindrical metalenses.
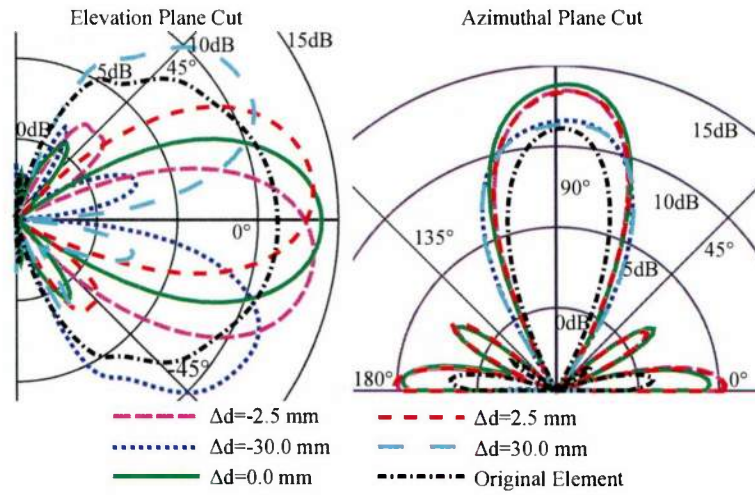
Fig. 2.16: Elevation and Azimuthal plane cuts of the original single-element pattern and five configurations of the three-element array.
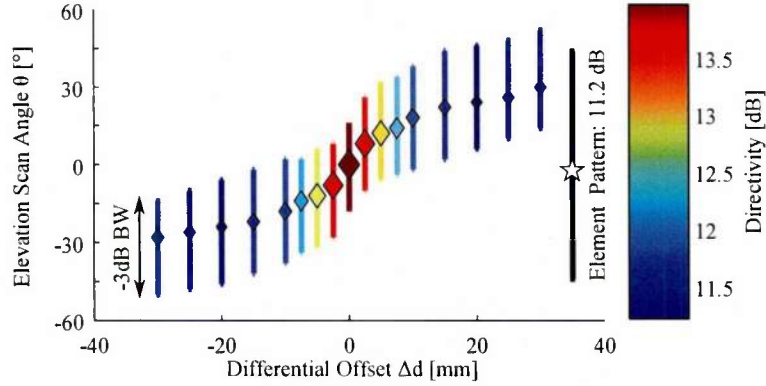
Fig. 2.17: Elevation-plane scan angle versus lens switching radius offset. The size and color of the diamonds indicates the peak directivity of the array, and the HPBW is illustrated by the height of the bars.

array antennas for some applications. The implementation for the elevation-plane scanning lens simply requires several copies of the azimuthal lens, which allows a single prototype design to be used in multiple antenna configurations.

2.5 Upper Hemispherical Beam Scanning

As an extension to the vertical scanning example introduced previously, a vertical stack of half-cylindrical antennas separated by PEC plates may be compressed into wedges to form a hemispherical lens, as illustrated in Fig. 2.18. By changing the metamaterial state in each component lens independently and feeding each of the wedge lenses with the uniform magnitude and phase, then a similar beam-forming procedure may be performed using the same beam-scanning concept as used previously. Creating an artificial aperture with phase and magnitude control throughout the sphere will allow a beam to be directed throughout the upper hemisphere. The asymmetric nature of this approach means that the beamforming quality will be limited as $\theta \to 90°$ near the ground plane, but electrical switches at the shared feeds could be used to enable or disable individual lens elements as required.

The complexity of the upper hemispherical lens for fabrication and assembly is significantly greater than that of the single lens, although the structure of the

individual lens elements is largely based on the original cylindrical design, and the operating concept is a simple extension of the three-lens array. The wedge-shaped metamaterial slabs complicate fabrication and assembly, and the lack of a completely symmetric layout introduces preferred directions to the beamforming rather than allowing completely arbitrary scanning. Preliminary simulation results have indicated, however, that the wedge shapes of the lens elements help to promote radiating modes rather than resonant modes, as were dominant in the cylindrical lenses.

The feed antenna presents additional complications for the upper hemispherical lens. Each of the wedge antennas, if using uniaxial magnetic metamaterials as in the original designs, requires theta-directed H-fields as the excitation. Tiling the lens elements, each of which would require an independent magnetic dipole feed, means that the overall excitation would behave like an electric dipole, with linear electric field polarized parallel to the hole in the center of the lens, and the theta-polarized magnetic field tangential to the surface of the cylindrical hole at all points. An explicit dipole feed, however, presents many challenges; primarily, the difficulty of getting the dipole excitation to efficiently couple into the metamaterial.

Since no existing antenna would exactly meet the requirements, several options were explored to determine what might be feasible. An explicit cavity antenna that generates the required field patterns in a narrow theta-directed slot such that each wedge was excited in the exactly analogous way to the original cylindrical configuration (i.e., a slot antenna radiating a magnetic dipole-type pattern at the center of the wedge) would be best, as it allows the excitation and the lens to be separately tuned. Selecting a spherical or cylindrical cavity is the first step based on the constraint for a cylindrical theta-polarized H-field. Based on the analysis of the resonant modes of concentric spherical cavities [74], a modified cavity was constructed as the region between two concentric hemispherical conducting shells with a 1 mm slot cut for $-85° \leq \theta \leq 85°$ at $\phi = 0°$. Exploratory simulations with a delta-gap excitation across the slot as suggested by [75] showed that the second-order resonant mode of this structure, as desired, demonstrated a theta-polarized magnetic field parallel to the slot antenna, but with a very poor mode coupling efficiency from the initial excitation method. Analysis of the field patterns within the cavity showed symmetric regions of solonoidal magnetic fields at the resonant

frequency, as seen in Fig. 2.19. Applying an electric delta-gap excitation (a coaxial probe connected to the outer shell and grounded to the inner shell for an actual implementation) in the center of the solonoidal magnetic field produced a much better, albeit narrow, impedance match to the second-order mode.
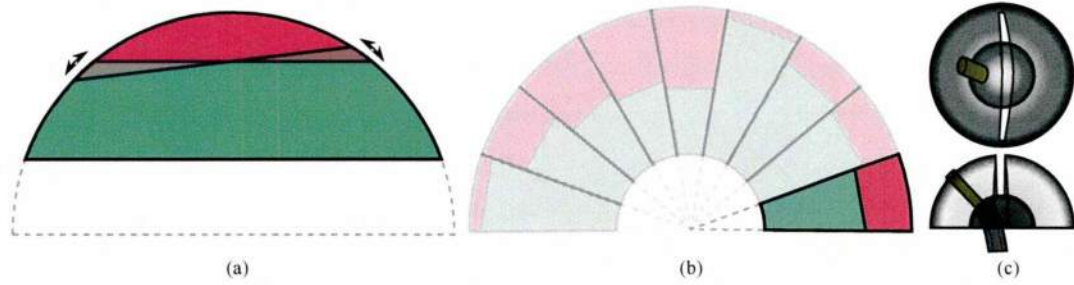
Fig. 2.18: (a) Single wedge-shaped ZIM lens (b) Array of wedge-shaped lenses arrayed in a sphere for upper-hemisphere beam scanning (c) Concentric spherical cavity magnetic slot antenna for use as a feed in the cylindrical gap at the center of the spherical lens, itself excited by a coaxial probe from the inner spherical surface.
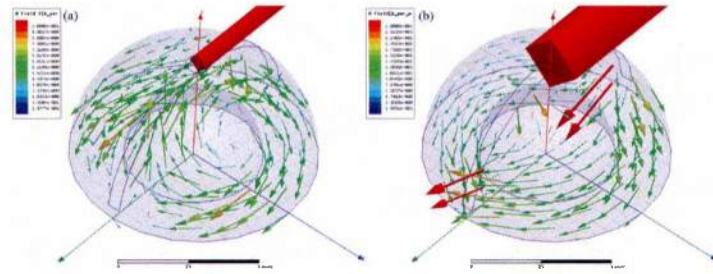
Fig. 2.19: Magnetic field patterns for the two lowest-order resonance modes. The second-order mode (b) demonstrates H-fields aligned with the slot, and shows a solonoidal magnetic field pattern for excitation by an electric probe.

The concentric hemispherical cavity antenna as described above was used to excite the hemispherical lens. After adjusting the cavity and slot dimensions to account for the difference impedance environment when radiating into the lens rather than in free space, an acceptable return loss was obtained for the demonstrated beam scanning pattern.

Initial simulation results of a basic model of the upper hemispherical lens are shown in Fig. 2.20. The upper hemispherical beam-scanning lens concept is still

in the early development stages, but offers some promising early results.
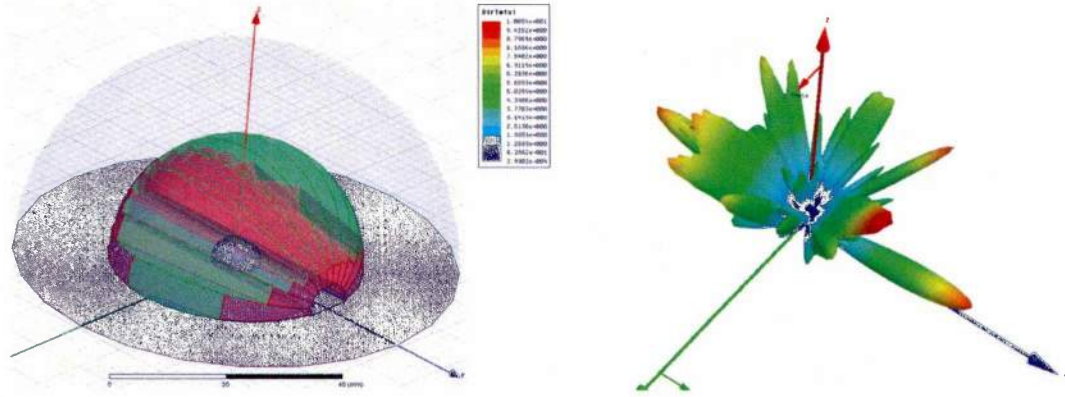
Fig. 2.20: Simulation model and resulting radiation pattern for a spherically-segmented ZIM lens excited by a concentric cavity-backed magnetic slot antenna. The many large sidelobes are due to the lack of design optimization, as this simulation is intended to show proof of concept, not a finished design.

2.6 Summary of Selected Prototype Lens Design Approach

A full circular cylinder is only one of the possible design configurations. Since a magnetic feed and metamaterial is employed, a vertical ground plane can be used with a half-cylinder lens to allow beam-scanning over up to 180 deg of the azimuthal plane. A magnetic slot antenna excited by a substrate-integrated waveguide (SIW) [7], [76] can be built into, and much of the power and support circuits hidden behind the ground plane, thus simplifying the implementation details and reducing the expense for a prototype. Compared to the previous descriptions, the semicircular antenna in Fig. 2.22 is simpler and cheaper to construct as a proof-of-concept device than the full cylinder. Also, a substrate-integrated magnetic slot feed in Fig. 2.21 is simpler to model and fabricate than a design based on a Spherical Split-Ring radiator [72].

The lens consists of a semicircular slab of metamaterial mounted against a ground plane in which a slot aperture has been placed in the center of the lens.

The top and bottom faces of the slab must be PEC to force the energy to only radiate in the plane of the lens rather than along the axis, parallel to the optical axis of the metamaterial. Since the uniaxial low-index slab may be viewed as a radiating dielectric resonator, the dimensions of the slab must be carefully chosen to promote radiating rather than merely resonant modes. In general, the lens will be a short disk with a large radius to increase the gain and front-to-back ratio.

Given the present impracticality of a purely optical control and switching method (for example, a system including an independently-excited optical fiber that illuminates an optically-sensitive semiconductor junction for each unit cell [77]), metallic power and control traces must be routed to each unit cell. The most effective topology for the lens is a hexagonal spiral for a circular lens, or a set of concentric hexagonal rings of unit cells for the semicircular lens. Using hexagonal unit cells of six resonators each with shared control circuitry requires only two unit cell configurations (straight and angled) to be designed, characterized, and tiled to construct the entire lens. To accommodate the hexagonal unit cells, the semicircular lens is approximated by a half-hexagon.

The entire lens antenna is matched to a 50Ω generator by the tapered line and adjustments to the size of the SIW cavity and slot, which are shown in Fig. 2.21. The antenna was designed independently of the lens. The narrow operating bandwidth may be improved in practice by using a slightly tapered or wider slot aperture, or by a nonlinearly-tapered microstrip transition. However, the narrow bandwidth of the current metamaterial implementation does not necessitate a wideband feed.

A homogeneous model of the half-hexagon metamaterial lens was evaluated using Ansoft HFSS, including the SIW slot and tapered microstrip impedance transformer. The resonance frequency of the SIW antenna can shift slightly with the loading effects of the ZIM slab. The hexagonal lens is chosen to be the smallest regular hexagon that covers a 225mm radius cylinder, and the height is 60 mm . An illustration of this antenna and radiation pattern is given in Fig. 2.22 with a 70 mm switching radius and a beam steered to 10 deg from broadside.
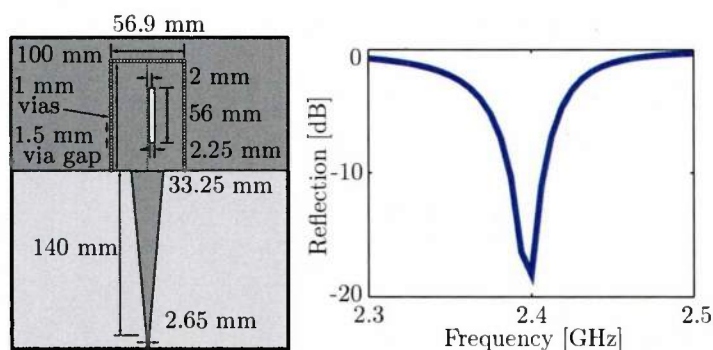
Fig. 2.21: (left) Dimensions and structure of the SIW slot antenna with associated
impedance-matching taper to a 50 ohm microstrip line. The antenna is fabricated
on a 0.78 mm (31 mil) Rogers RO5880 RF substrate with a solid rear ground plane.
(right) Reflection coefficient at the microstrip feed for the SIW antenna, showing
a good match at 2.4 GHz , but only a small bandwidth.
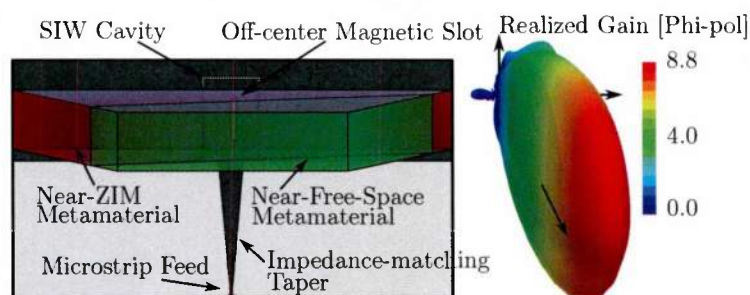
Fig. 2.22: Illustration of the hexagonal near-zero-index anisotropic lens with re-
configurable metamaterial slab, fed by a magnetic slot antenna constructed with
a SIW, with associated radiation pattern.

Chapter	3

Metamaterial Design and Measurements

Dynamic, non-passive control is the largest challenge for the implementation of a reconfigurable volumetric metamaterial, since the control circuits cannot be simply hidden behind a ground plane as would be allowed for a reconfigurable metasurface or FSS. Since the metallic control traces will affect the response in any case, the metamaterial must be designed so as to minimize their effects on its desired operation. The use of a magnetic metamaterial simplifies the design of the reconfigurable elements, since planar loops may be created using printed circuit board (PCB) technology. Using an array of split-ring resonators (SRR) where varactor diodes are placed in the gaps and controlled by an array of shift registers creates a metamaterial that can be spatially tuned. The spatial reconfiguration requires that control traces propagate throughout the lens to distribute power to the control circuits and data to determine the metamaterial state at all locations within the lens. The varactor properties and SRR dimensions are chosen to induce a strong magnetic resonance just below the desired operating band when the varactor is in one state and to eliminate the resonance for the other. Operating at a frequency just above the resonance yields a low-index, near-ZIM effective medium due to the Lorentzian permeability response of the SRR. A metamaterial prototype satisfying these requirements is described below. Several design iterations were performed in order to account for discrepancies in the simulation model and to refine the metamaterial design prior to manufacturing a bulk lens.

3.1 Reconfigurable Metamaterial Design Considerations

When designing a spatially reconfigurable metamaterial, all of the questions and factors for its static counterpart still apply. What is the frequency and polarization of operation? What is the desired electromagnetic behavior? The frequency of operation drives the dimensions of the metamaterial, the fabrication technique, and the available tuning mechanisms, while the polarization and desired behavior will help to specify the required unit cell. What is the tuning mechanism, and is it continuous or discrete? How is the tuning mechanism controlled? The different requirements of a binary vs. a multivalued or continuous (analog) control system can significantly change the complexity of the metamaterial design. In all cases, the effects of any additional traces, components, or design modifications on the metamaterial behavior (other than the desired tuning response) should be minimized. The answers to these interrelated questions will jointly determine the required unit cell configuration and associated complexity of the control system.

Many of the common volumetric unit cells for microwave frequencies (splitring resonators [22], [35], [78], electric LC resonators [50], end-loaded dipole [17] elements) provide an anisotropic effective medium response. Although isotropic metamaterial responses may be engineered through a combination of multiple resonator elements in different orientations, such a configuration introduces additional challenges when considering tuning and control. In comparison, a collection of parallel, planar metamaterial panels simplifies fabrication. Nonresonant metallodielectric metamaterials may be used as reconfigurable elements, but it is likely that the effect of the additional traces for control and biasing will produce a larger relative effect on the response of the structure than if a resonant behavior is the desired response. In addition, the behavior of a sharp resonance will be tuned and controlled by a smaller change in active component properties than will that of a nonresonant design.

3.1.1 Viable Tuning Mechanisms

Allowing full control over the effective response of subregions of a metamaterial slab ultimately requires that the actuators themselves be independently controlled, as well. Physically tuning a unit cell's geometry, for example, by adjusting the position of the top of a resonator relative to its base, is practical for a large panel but not a viable option for individual unit cells. Electrical control mechanisms are the only practical option for a spatially-tunable metamaterial implementation.

MEMS-based switches, varactor diodes, and PIN diodes are the most common tuning elements for RF and microwave circuits. Packaged MEMS devices are presently very expensive, require high actuation voltages that are not compatible with CMOS-level logic circuitry, and, for these reasons, are not suitable for bulk usage (i.e., one switch per 5mm unit cell in a 20x20x5 grid). Reverse-biased varactor diodes act as variable capacitors, which makes them useful for controlling resonance frequencies. As voltage-controlled devices, power consumption, even for an array of many elements, is minimal. At higher frequencies, varactors become lossy, with parasitic impedances overtaking the desired capacitance change. GaAs varactors have better frequency responses than Si varactors, but are less widely available. PIN diodes act as electrically-controlled potentiometers, with RF conductance changing from high to low as the current through the diode is adjusted. The DC current requirements will become significant for an array of hundreds or thousands of unit cells, however, and RF losses from the resistive properties of the device may be impractical for transmission-based metamaterial devices. Both varactor and PIN diodes may be configured based on their bias settings to behave in binary, multilevel discrete, or continuous tuning modes, while MEMS switches are typically discrete in nature. Other tuning options such as packaged RF switches and transistors have been investigated and found impractical for our designs.

Despite the increasingly poor frequency response above 1 to 2 GHz, varactors (specifically, Skyworks SMV1247-074LF common cathode varactor diodes, with effective capacitance ranging from 0.8 to 7pF for applied bias voltages from 0 to 5v) were determined to be the best selection for the example ZIM / free-space reconfigurable metamaterial. The relatively large power consumption of the PIN diodes would have added significant complexity to the power regulation circuitry, and likely a substantial increase in trace sizes would have been necessary to sup-

port the current, compared to a varactor-based design. In order to obtain accurate models of the metamaterial performance, two-port scattering parameter measurements of the varactors as a function of the applied bias voltage were performed using a network analyzer and included in the simulation models, since the circuit models provided in the data sheets were not found to be accurate at our operational wavelengths.

3.1.2 Control Circuits

Controlling the properties of a bulk metamaterial slab generally consists of changing the bias voltage or current on a single or small number of signal lines. In this case, the circuitry within the metamaterial is limited to the bias distribution lines and, potentially, isolating chokes or inductors. The interconnecting bias traces can in some cases be integrated directly into the metamaterial unit cell design, such as in the case of a slot-based structure [79]. Since the entire board is tuned together, and the control signals may be generated off-board, it is simple to produce binary, multilevel, and continuous (analog) ranges of command signals.

Extending to a spatially reconfigurable metamaterial design introduces additional complexities: generating bias signals in a distributed fashion, distributing control and power signals to the bias generators, and balancing the complexity of the control signals against the complexity and electrical size of the decoding circuits for the bias generators. For this discussion, it is assumed that each unit cell (or perhaps, small groups of unit cells) are tuned independently and require a separate bias signal. For a large (greater than a wavelength) volumetric metamaterial slab, there are too many unit cells for each to have an independent externally-provided bias signal (except possibly in the case of the optical fiber-based configuration). Thus the bias signals must, for any practically-sized metamaterial slab, be generated within the metamaterial slab itself, leading to a system of distributed bias control circuits, which must be independently addressable. An off-board controller (such as a microcontroller or laptop computer) is assumed to generate the command signals that are provided to the on-board bias generation circuits, which interpret the command signals to produce the direct bias levels for the metamaterial. Placing the bias generation circuitry within the metamaterial itself adds a

constraint on the complexity of the bias signal, both from the physical size of the circuit as well as the number of digital or analog control lines necessary to encode the desired metamaterial state. The constraints become more stringent at higher frequencies, where a single surface-mount lumped element or IC component may consume a significant fraction of a unit cell's area. Most implementations of a bias generation circuit will also require ground and supply voltage traces in addition to the control signals themselves. This represents a fundamental trade-off - the more traces are directly provided from the external controller, the simpler the bias generation circuitry may be, but the more effect the control lines will have on the operation of the metamaterial.

It would be possible to implement an analog control system with only two wires (signal and ground) for a frequency-multiplexed control signal - each unit cell would be addressed by a specific audio-frequency tone, implemented by narrow band-pass passive filters. The magnitude of the selected tone, after rectification and low-pass filtering, would then be applied as the bias signal to the unit cell. Such a scheme may be implemented with relatively simple bias generation circuits at the unit cell level, but requiring a separate analog band-pass filter for each unit cell produces a complex system-level design that would be very difficult to test and verify.

Similarly, a two-wire (voltage supply with multiplexed binary signal and ground) digital control interface with analog bias outputs could also be devised that separates the voltage supply and control signal by filtering, and listens for specific digital commands to change the bias outputs for a given unit cell. Such a system would require a physically large and complex circuit if implemented using discrete components and single-function microchips, but may offer very sophisticated bias outputs (including binary, multilevel, or analog outputs) if implemented in a custom microchip (or possibly a small microcontroller). This approach could be beneficial in a mass-produced metamaterial structure, but would be very expensive otherwise.

Allowing the number of control signals to increase to five and restricting to binary bias levels between an externally-provided low- and high-voltage range allows a much simpler bias generation circuit. Such a circuit could be implemented by choosing an SPI (serial peripheral interface)-based communication protocol (power (VDD), ground (GND), data, clock) and providing one additional negative volt-

age level (VBIAS). The bias signals provided to the unit cell would switch between VDD-VBIAS and GND-VBIAS with no voltage dividers or power regulation within each bias generation circuit. Each unit cell (with associated bias generator) would be connected in sequence and provide a single-bit serial-to-parallel shift register, so that unit cells are independently addressable by their position in the array. A circuit diagram for such a unit cell design is included in Fig. 3.1. This plan was seen as a good trade-off for a prototype design between minimizing the number of external control signals and minimizing the complexity of the distributed bias generation circuits. Since most shift register ICs have multiple bits, several metamaterial resonators could be grouped into a single unit cell, each with a separate output from the 4-, 6-, or 8-bit shift register; this would also reduce the fractional area required by the bias circuitry relative to the resonators. A simple 8-bit microcontroller is sufficient to compute the command signals for an entire lens, which take the form of a bit string with the encoded state of each unit cell within the lens. Control signals are only required when the metamaterial state is changed, although the voltage levels must be maintained at all times to preserve the shift register state. A disadvantage is that the entire array of unit cells must be reset in order to change the state of a single resonator; a high clock speed (100kHz-10 MHz) can mitigate the time delay associated with the state reset throughout the array.

The number of control traces of this scheme could be reduced by using a self-synchronized communication scheme (RS-232/UART) or regenerating the clock (e.g. phase-locked loop) from the data line, or by including additional voltage regulation within the bias generator; these changes would significantly increase the complexity and board area required by the bias generation circuits. Another modification of this design would be to allocate multiple bits of the distributed shift register to each unit cell, so as to provide multilevel bias signals and more granular control of the metamaterial behavior. This would only be limited by the available area for the bias circuitry on the metamaterial panels and the number of available bits in the shift register. These two approaches may be beneficial at lower frequencies (100-700 MHz range) where the unit cell dimensions are large enough to include the additional circuitry.

With any digital control method, the noise on the clock and data lines must be
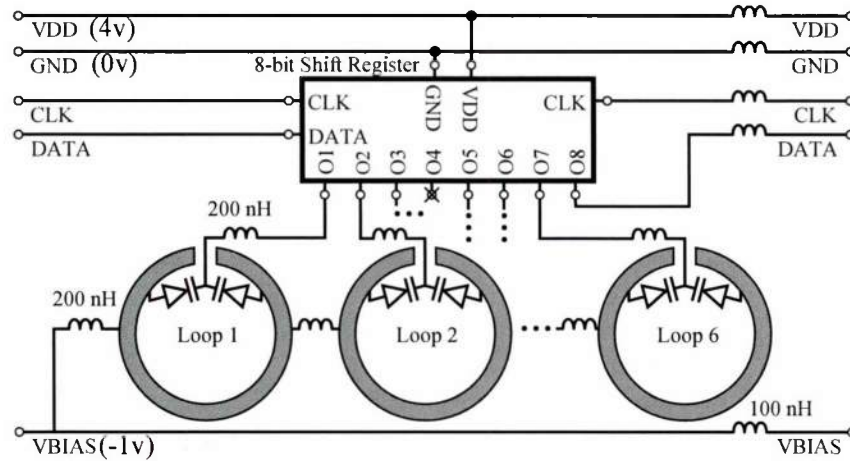
Fig. 3.1: Circuit diagram for a single hexagonal unit cell showing the bias and control lines of a shift register-based control system for the resonator state.

managed to avoid errors in the data transmission. Although CMOS logic, with its very low current draw, can support a large fanout from a single logic output, the rise and fall times of a pulse can be greatly extended by the excess capacitance of long traces, as well as by any lumped inductance added between unit cells to break up the long wires. Some early prototypes of a metamaterial panel with hundreds of unit cells in sequence were found to be very sensitive to noise on the clock lines. Some of the results included multiple clock signals being interpreted from a single rising edge of the clock due to jitter at the transition level - ultimately, the pattern of bits set in the lens was not the same as the commanded pattern. The control system was very sensitive to small, nearby static discharges, which commonly resulted in the addition of 10-100 bits of random data to the input of the distributed shift register. These effects were mitigated by including additional decoupling capacitors between the clock and ground lines and the supply voltage and ground, as well as by including Schmitt trigger buffers for the clock signal at selected points throughout the metamaterial slab to reduce the clock fanout and rise time.

3.1.3 Metamaterial Resonators and Unit Cell

The active element of the reconfigurable metamaterial must be selected for its ability to generate the desired metamaterial response as well as the ease of tuning. The narrow bandwidths of resonant elements can actually be useful in this circumstance, since a relatively small change in capacitance can produce a large change in effective medium response.

It is desirable that the metamaterial unit cells be selected in such a way that the addition of the bias lines and circuits will minimally affect the metamaterial response, but some disruption is practically inevitable. The addition of metallic wires and components will disturb the EM field, and thus change the response. One strategy to meet the goal is to minimize the area used by the extraneous circuits - in the limit, as the area used by the bias generation circuits decreases compared to the area covered in the metamaterial resonators, the effects of the extra circuits are reduced. This approach is limited by the size of the required circuit components, however. A second strategy involves the selection of the resonant element such that the targeted EM field effect is not directly influenced by the additional tuning circuits. For example, a planar magnetic loop element interacts with the normal magnetic field, which itself does not interact strongly with additional lengths of wire in the plane. In comparison, a planar electric resonator (dipole, end loaded dipole, or electric LC resonator) that interacts with the in-plane electric field will couple strongly with any other coplanar metallic structures. Keeping the control circuitry coplanar with the metamaterials and the tuning circuit allows for much simpler fabrication of a completed design. For this reason, planar magnetic resonators may be a better choice than planar electric resonators. An additional benefit of the magnetic design over the electric is that, for a given resonator size, the magnetic loop resonators produce a much stronger resonant response due to the increased field coupling area within the loop. This stronger response enables the metamaterial effect to be dominant over the spurious responses of the tuning circuits and allows the use of electrically smaller resonant elements, which in turn improves the homogeneity of the effective medium properties.

Choosing a specific resonator should also consider the tuning response to the selected actuator. For the varactor diode and split-ring resonator combination, a tunable capacitance will change the resonant frequency of the ring by modifying

the overall capacitance of the structure. However, the structure of the SRR must be selected such that the change in the varactor capacitance produces the maximum change in overall device capacitance. Ideally, the varactor should represent the dominant capacitance term within the SRR, in order to maximize the fractional change in resonant frequency compared to the fractional change in varactor capacitance. Several common SRR designs are depicted in Fig. 3.2. If the varactor is placed in series or parallel with comparable distributed capacitance terms introduced by the SRR geometry, then tuning will be more difficult. For these reasons, a variation of the single-split single-layer split-ring resonator (Fig. 3.2(b)) was selected for the prototype design.

(a)   (b)   (c)
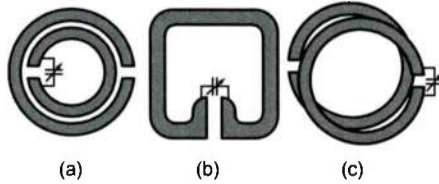
Fig. 3.2: The variable capacitors integrated into the three SRR designs will have different effects on the resonant frequency of the overall resonator for the same change in capacitance. The varactor in (b) has the potential for the largest effect, since the lumped capacitor is the dominant capacitance term in the resonator.

3.1.4   Unit Cell Interconnection

The selected control system for the prototype reconfigurable metamaterial lens relies on a single array of serially-interconnected unit cells, where the resonant metamaterial elements may be grouped to share control circuitry. The resulting slab should be created in an approximately semicircular shape, and the path of the control traces throughout the lens should be designed to interact minimally with the controlled fields or, at least, to interact with the fields in a homogeneous and symmetric fashion (this is very dependent on the selected polarization and the application of the resulting metamaterial). These constraints help to dictate the topology of the interconnections between unit cells.

For the nominal target application of a metamaterial lens antenna, the source is intended to be placed at the center of the semicircle with a vertically-polarized

magnetic field and the energy propagating radially outward. Any alignment of control traces with a rectangular grid would result in anisotropic in-plane electric material properties with a different material tensor orientation relative to the propagation direction for waves in different regions of the lens. A concentric spiral arrangement of the unit cells with spiral interconnecting control traces will also interact with the in-plane electric field, but in a way that is approximately independent of incidence angle. Note that for a different application and desired wave propagation, a rectangular grid of unit cells may be acceptable.

Metamaterials, as periodic structures, are described by their unit cells. This is convenient for design, as the geometry of only a single resonator must be specified, but is also convenient for simulation, as the properties of a slab may be extrapolated from the response of one or a small number of individual unit cells. However, periodic unit cells cannot be used to generate an interconnected circular spiral with a uniform resonator density; at the very least, the control traces would be different as the radius of curvature increased. Hexagonal unit cells may be used, though, to create a half-hexagonal tiling that is a good approximation to a circle, illustrated in Fig. 3.3. Two proto-tiles are required - one with a 180 degree separation between the input and output control traces, and one with a 120 degree separation. These two tiles, arranged in a spiral, form a space-filling curve that may be extended as large as is desired.

With hexagonal unit cells, it is convenient to place a single 8-bit shift register in a small, surface-mount package (SN74LV164) at the center of each tile, and to include six magnetic loop resonators to share the outputs. The centers of the loops are rotated by 20 degrees with respect to the vertices of the hexagon to obtain a more uniform distribution of resonators within the metamaterial. With this configuration, although the unit cells themselves may be slightly large to be considered a metamaterial (approximately $\lambda/6$), the resonators themselves are electrically small, approximately $\lambda/12$.

3.1.5 PCB Design and Layout Software

The vast majority of microwave and RF metamaterials are designed to be fabricated using printed-circuit board technology, which is widely available and rela-
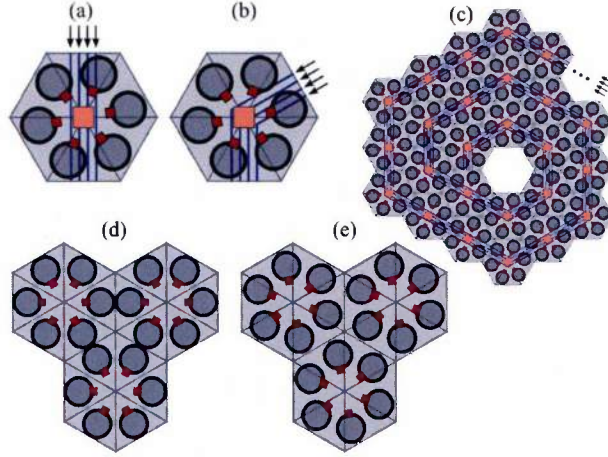
Fig. 3.3: Illustration of hexagonal unit cells and their combinations. Two variants, the (a) unit cell with straight connection and the (b) unit cell with a bent connection may be combined in a space-filling curve to form a (c) hexagonal spiral lens. (d) Orienting the resonators within each triangle yields a less desirable distribution than does (e) rotating the resonators within each unit cell by 20 degrees, which provides a more uniform distribution of resonators in an extended array.

tively inexpensive. The use of a PCB-based manufacturing approach is well-suited for extending to electrically-tunable unit cells, as the active components and control circuits may be easily included in the design and manufactured simultaneously. Some of the standard assumptions and practices in PCB design must be re-evaluated for use with reconfigurable metamaterials, however. The use of a blanket soldermask over the metamaterial according to standard PCB design practices, for example, produced a small but measurable distortion on its simulated performance, since the slightly lossy soldermask layer altered the resonant frequency of the loop. The effect of the losses was mitigated by only applying the soldermask to the regions immediately surrounding the component footprints, which allowed automated surface-mount assembly tools to operate normally. For simulation purposes, the soldermask was modeled as a 0.4mil layer of dielectric with ϵ_r=4.5 and tanδ=0.029. This parameterization produced close agreement with the measurement results when the soldermask was applied to the entire unit cell in an early prototype, and was used for the partial soldermask coverage in later designs.

The available design software that can handle the combination of the meta-

material unit cells with PCB traces and components is limited. Reconfigurable metamaterials for which the control circuits are very simple or integrated into the metamaterial structure itself may be simple to draw in AutoCAD or other non-specialized planar drafting tools, or to generate programmatically via a script. However, adding spatial control over the metamaterial properties will generally require more intricate circuitry for which a specialized software tool is more useful. Conventional PCB design software (for example, the gEDA design suite) does not typically support easy specification of the exact positioning and arbitrary curvilinear geometrical shapes required to implement a metamaterial unit cell. Common PCB design rules require that traces follow specified grid lines, and that components may only be rotated by 90 degree increments - these constraints are often undesirable for metamaterial geometries. These tools do save much time and effort by automatically generating valid soldermask and solderpaste layer specifications and the component placement listing to allow automated assembly and soldering of surface mount components, however.

Alternatively, microwave circuit design tools such as Ansoft Designer allow arbitrary placement and parameterization of nearly all geometrical elements on multiple layers. Their support for component footprints, automated trace routing, and editing of conventional circuit layouts is more limited in practice, though, increasing the difficulty in laying out the control circuit designs. All PCB drawings shown in this paper were created using Ansoft Designer together with custom Matlab scripts to generate the tiled copies of the periodic unit cells, as well as the supplemental design documents for automated PCB assembly (component placement and bill of materials files). The geometry was heavily parameterized, so that unit cell dimensions such as SRR loop radius and trace width could be changed without regenerating the entire layout.

Graphical design software for vector images such as Inkscape or Adobe Illustrator are much easier to use for creating exact, arbitrary 2D geometry and have many desirable features for drawing metamaterial layouts, including the ability to tile and clone unit cells to form a large panel. However, conversion tools are not available to easily convert from the native vector drawing formats to the required Gerber formatted files for fabrication.

3.1.6 Bias Supply Regulation and Board-Level Considerations

Voltage or current-biased components will be sensitive to variations in the supply levels. At a board level, the external power supply may be regulated to ensure that the power supplied to the board remains constant independent of load. The designer does need to be aware of current-related voltage droops within the interior of the metamaterial slab that may cause undesired detuning. Unlike most PCB designs, which allow for large ground traces or ground planes and separate layers for each power supply rail, the dimensions of the supply traces (ground and voltage rail) must be minimized as much as possible in the reconfigurable metamaterial.

In order to ensure proper voltage regulation, there is the option to either minimize the voltage droop due to current losses by reducing current and/or reducing trace resistance, or to include on-board voltage regulators near the unit cells. The first option, as a passive solution to the problem, is feasible for the shift register-controlled varactor diode configuration, due to the very low current requirements of the shift register. An initial unit cell prototype included a voltage reference and linear regulator on each unit cell to ensure that the varactor biases were uniform throughout the metamaterial slab, but this substantially increased the component count, manufacturing cost, and distortion in the effective material properties. Once measurements showed that the resonant frequency of the resonators was not as sensitive as expected to small variations in the varactor bias voltage, the on-board voltage regulators were removed from future designs.

3.2 Initial Metamaterial Design and Prototype

The first metamaterial design was created based on some of the considerations described above, and many of the remaining factors were determined through the fabrication and testing of this initial design. Choosing a resonant magnetic metamaterial at RF-microwave frequencies implies the use of some variant of the split-ring resonator, which may be modeled as resonant LC circuits. The resonant frequency will then be adjusted during design by changing either the inductance or capacitance of the structure, usually by altering the geometry (loop dimensions,

substrate thickness or material) of the structure. Geometric tuning is not an option for a reconfigurable metamaterial, however. For low frequency applications or those where the unit cell size is greatly constrained, lumped elements have been placed in the gap of simple SRR elements to add capacitance or inductance [80]. Using an electrically tunable variable capacitance or switch instead of a static, passive lumped element can allow for tuning the resonant frequency of the metamaterial. Varactor diodes are a practical choice; most specifically, the common-cathode varactor diode. Reconfiguring the metamaterial resonance frequency is achieved using Skyworks SMV1247 Hyperabrupt Silicon varactor diodes, which have a capacitance that changes from 8 pF to 0.8 pF for 1v and 5v reverse bias voltages, respectively. The silicon varactors have higher losses than high-performance GaAs diodes, but the performance is good enough for an initial prototype demonstration. An ideal implementation would use unpackaged GaAs varactor dies bonded directly to the PCB to eliminate parasitic impedances; this is impractical for the initial proof-of-concept device, however. A common cathode varactor diode pair in a single-split ring, as in Fig. 3.4(b), was found to be a more practical configuration than the use of a single varactor with a dual-split loop, as in Fig. 3.4(a). The dual-split loop with either a discrete or distributed (microstrip, interdigitated) second capacitor suffers a decreased tuning range of the effective loop capacitance due to the series combination of a fixed with a tunable capacitor. Using two discrete single-ended tunable varactors to create a dual-split loop would not reduce the tuning range, but increasing the component count is undesirable. Thus, the single split with a single common cathode varactor simplifies construction by requiring only a single tunable component while maintaining the maximum tuning range. For designs using either the single or common cathode packages, the reverse bias voltage must be applied to the varactor and loop through RF-isolating lumped inductors or chokes.

3.2.1 Control Signals

An array of shift registers was selected as the control method. The resonators with associated varactors and inductors are grouped into hexagons in sets of six to share an 8-bit shift register. The shift registers require power and ground references, as well as a control signal (data) clock line, and bias line. The hexagonal unit
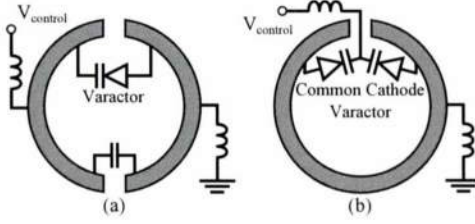
Fig. 3.4: Loop resonators employing both (a) individual varactor diodes and (b) a paired common cathode varactor diode. The common cathode configuration has better tuning range than a single varactor with second capacitive gap and does not require an additional lumped element.

cells (hexes) were cascaded in a hexagonal spiral as described in section 2.2.5 in order to provide the power, ground, data, and clock lines to each unit cell. In this configuration, every varactor is individually addressable to allow for arbitrary tuning of the effective shape of the lens.

The unit cell and resonator dimensions and properties are chosen by parameter study, since there is no analytical solution available for the fields in the metamaterial and the simulations are too lengthy to use global optimization algorithms. The metamaterial was designed with a Rogers RO4003 substrate, and was later changed to use FR403 as an inexpensive but slightly more lossy alternative. Simulations of the rings alone (i.e., ignoring the additional lumped elements and control traces) to reduce the simulation time are first performed to choose the appropriate loop dimensions for resonance. After an approximate design has been selected and the effective material response at the target frequency switches between near-ZIM and near-free space with the two varactor states, the additional traces are imported into HFSS from the PCB layout tool and the simulations repeated to confirm the results. Comparing the simulated effective permeability results in Fig. 3.5 and Fig. 3.6, it is seen that although the extra control circuitry does distort the metamaterial response, as expected, the primary magnetic resonance responsible for the ZIM behavior is still present.
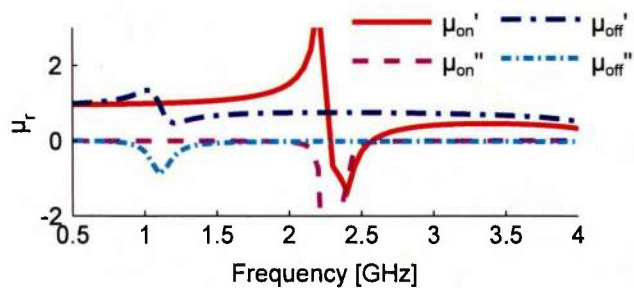
Fig. 3.5: Predicted permeability of the split-ring resonators and varactors alone.
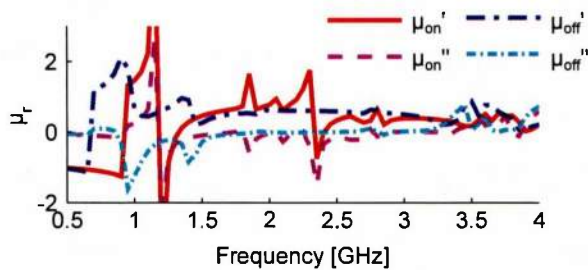
Fig. 3.6: Predicted permeability of initial prototype metamaterial including the effects of the control circuitry and additional lumped elements.

3.2.2 Control and Bias Circuitry

The circuit schematics for each hex cell are shown in Fig. 3.7 and Fig. 3.8. The circuit design shows headers for propagating the power, ground, data, and clock lines between unit cells, and the shift register for controlling the switch states within the unit cells. Decoupling capacitors were provided for the clock and data lines. The values were chosen to be small enough such that the distributed capacitance of the accumulated elements would not degrade the clock signal, yet large enough to prevent strong currents from circulating through the bias lines. The shift register is powered at $V_{DD} = 5v$, and the required 1v and 5v voltage levels are created using a resistive voltage divider for each loop (Fig. 3.8). One end of the voltage divider is tied to the +5v rail, and the other fed by the shift register, while the varactor bias level is taken from the center tap. By using a 4 : 1 ratio of resistances in the voltage divider, the bias level at the center will be 5v for a 5v control signal, and 1v for a 0v control signal. The varactor consumes very little or zero current, so relatively high resistor values may be chosen to reduce the quiescent current through the voltage divider. An alternative solution for generating the bias voltages using Zener diodes for each resonator in order to achieve increased bias voltage accuracy was investigated, but the Zener diodes increased the current requirements by an excessive amount, as well as the component cost, without greatly increasing performance over including a single voltage regulator within the hex to combat voltage droop throughout the lens.

The restricted widths of the current-carrying traces through the metamaterial and the estimated current requirements of the loops made voltage droop through the lens a valid design consideration. Due to the presumed sensitivity of the varactor diodes to small voltage variations and the requirement that the lens behave as a homogeneous structure, precision voltage sources were used in each unit cell to generate a 5v level relative to the provided 6-7v Vdd power supply rail. The voltage reference was achieved using a low-current shunt voltage regulator (LMV431) in a pseudo-Zener circuit configuration. Despite the choice of a low-current device, the voltage regulator still turned out to have the largest current requirements in the circuit design. Later measurements of the prototype demonstrated that the varactor sensitivity was not as extreme as expected, and the reduction of the current requirements from the voltage regulators would significantly alleviate the

voltage droop and allow consistent voltage references without the per-hex voltage regulators.
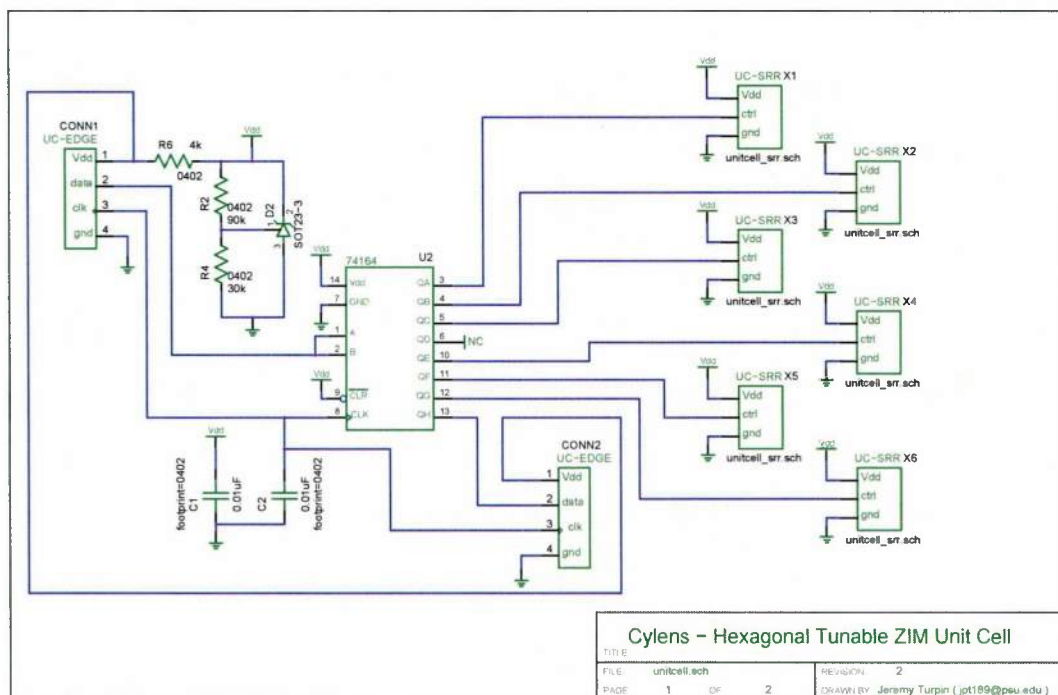
Fig. 3.7: Initial prototype unit cell circuit schematic.

3.2.3 PCB Layouts and Simulations

The PCB layouts of the unit cell design based on the schematics are shown in Fig. 3.9. This layout was created using the open-source gEDA PCB tool. The software tool was capable of performing the design, but was non-optimal for constructing a PCB layout in which precise positioning and rotation operations were required; future PCB designs were performed using Ansoft Designer.

Periodic simulations of the hexagonal unit cell, including the control traces and lumped elements, were performed in Ansoft HFSS for the full-wave simulations, and used the Matlab RF Toolbox to compute the effective response of the system including the effect of the tunable lumped varactors, which were incorporated into the simulation results using the RF port Substitution technique, which is il-
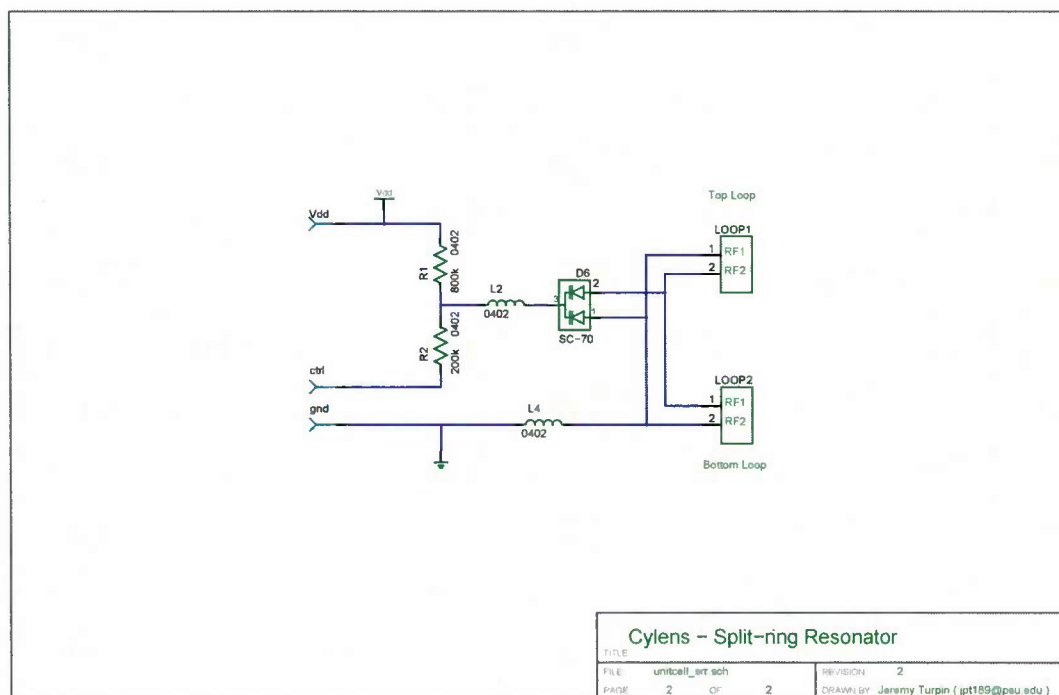
Fig. 3.8: Schematic of the each of the loop elements in the prototype unit cell.
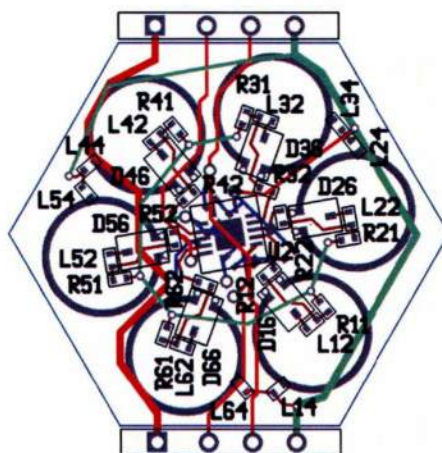
Fig. 3.9: Original Hex cell PCB layout.

lustrated in Fig. 3.10. HFSS does not support the inclusion of arbitrary circuit components (other than parallel RLC boundary conditions) into a simulation, but the effects of near-arbitrary 2-port network elements (with behavior determined by a frequency-dependent S-parameter matrix) on the scattering parameters of a larger structure may be incorporated by placing a single lumped port at the location in the simulation where the network effects should be inserted. The Matlab RF Toolbox contains functions for manipulating S-parameter matrices, but the functions required to perform the port substitution procedure may be easily rewritten based on network theory. The two-port representation of the network element is first terminated at one port by a short circuit. The requirement to short the second port means that simulations of shunt networks will not be accurate with this technique. The equivalent port in the N-port scattering matrix from the HFSS simulation results is then terminated by the impedance determined by the single-port scattering matrix of the shorted network element. The remaining (N-1)-port scattering matrix describes the behavior of the simulated system with the network elements inserted into their proper place in the circuit. This procedure may be repeated in order to include independent sets of network responses, as well. A limitation of Matlab's RF toolbox implementation is that all of the ports in the design must be normalized to the same impedance, which means that all of the lumped ports in the design will be generally normalized to 376 Ω when using a floquet port as the primary excitation. This limitation does not apply when using Ansoft Designer to perform the port substitution, as it does support the use of Touchstone (*.snp)-formatted files with nonuniform port impedances. Designer is simpler to use for extracting the effective simulation response when including arbitrary lumped elements, but Matlab is more well-suited for automating the data extraction and processing procedures.

3.2.4   Prototype Fabrication and Assembly

Several copies of the prototype metamaterial unit cell were fabricated on an inexpensive FR4 substrate in order to test accuracy of the simulation models. A quick-turn PCB vendor (Advanced Circuits) was used to fabricate the bare board design in Fig. 3.11, with the finished board in Fig. 3.12.
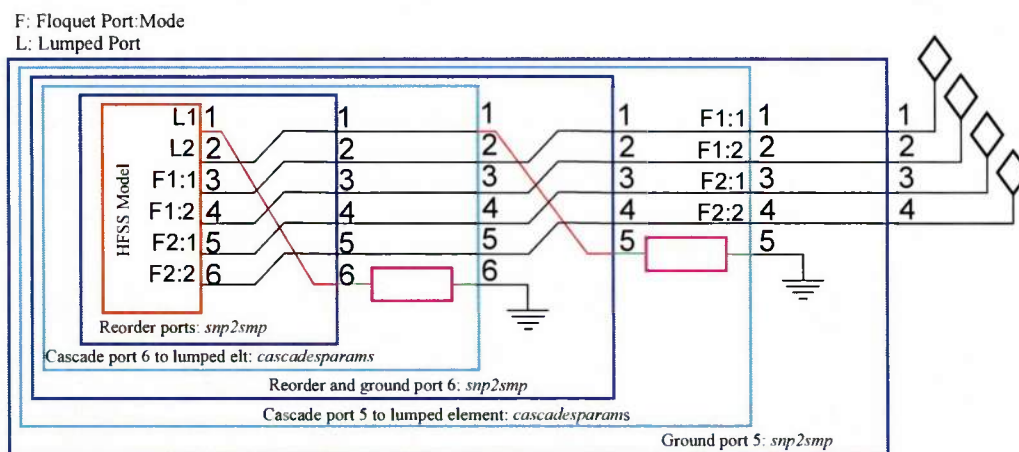
Fig. 3.10
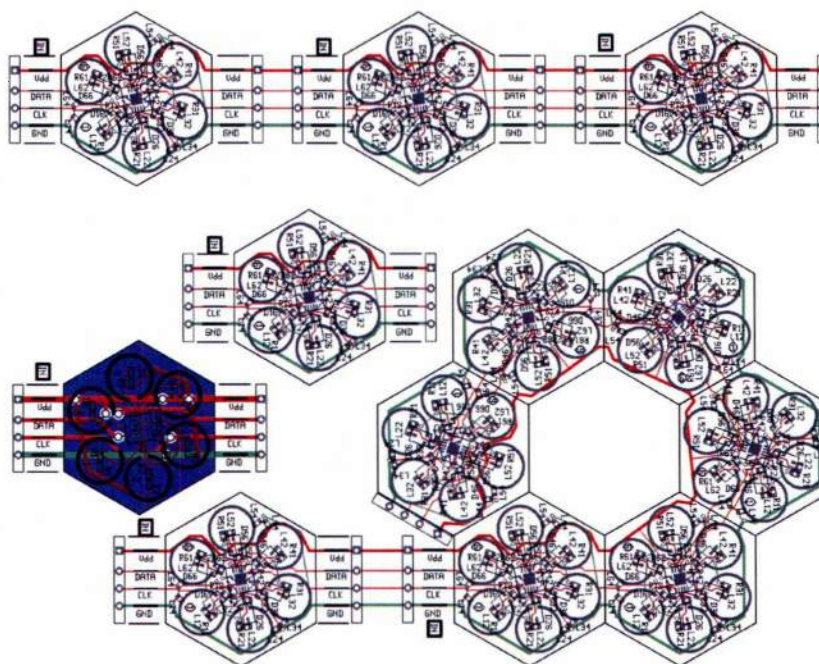
Fig. 3.11: Fabricated PCB board layout, designed using the gEDA open-source electronics design package.

Fig. 3.12: Fabricated PCB board as received from the manufacturer.

To reduce prototype expenses, the board was hand-assembled and soldered at Penn State. Individual hexes were removed from the PCB using a hacksaw and hand-populated with solder paste and components before being cycled through the reflow oven. Fig. 3.13 and Fig. 3.14 show photographs of the assembly process.

(a) Practice solder paste application on the varactor footprints.

(b) Practice solder paste application on the narrow-pitch shift register pads.
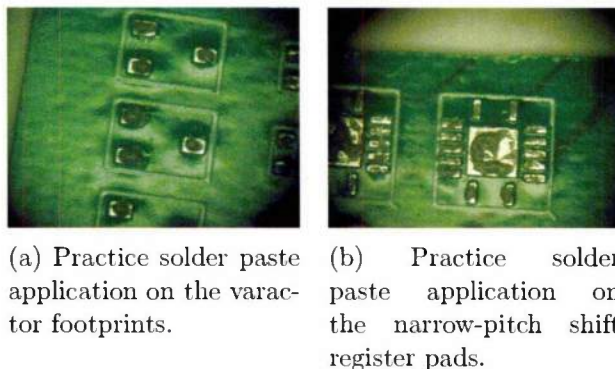
Fig. 3.13: Practice solder paste application.

(a) Reflow oven used for the assembly process.

(b) Top side of assembled unit cell.

(c) Bottom side of assembled unit cell.
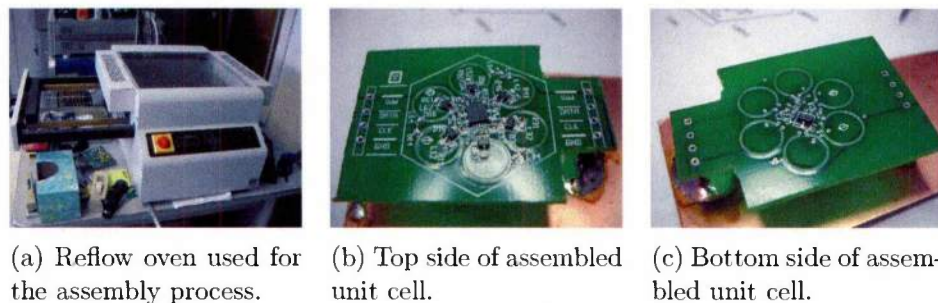
Fig. 3.14: Soldering and manufactured sample.

3.3 Initial Metamaterial Prototype Characterization

The fabricated and assembled unit cells, shown in Fig. 3.15, were measured and compared to simulation results in order to correct the measurement model and ensure a functional final design.
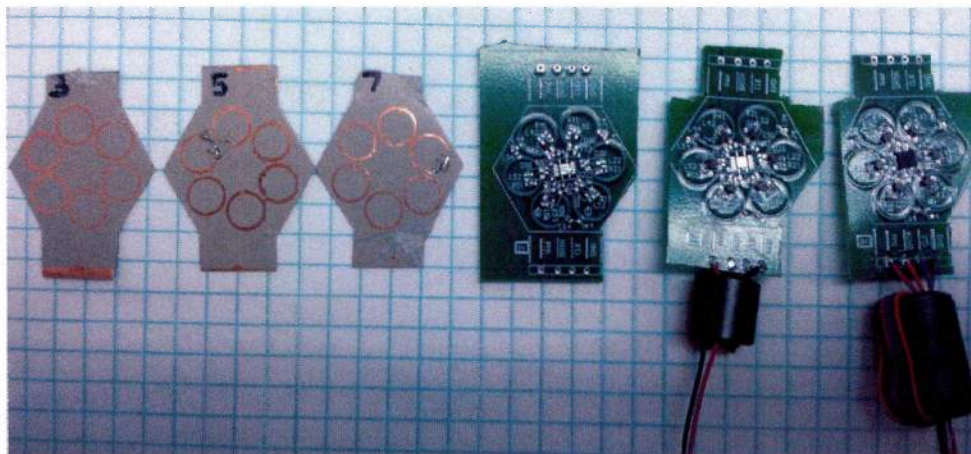
Fig. 3.15: From left to right, a dual-sided loops-only sample, a front loops-only sample, a back loops-only sample, an unpopulated board, a variable-bias sample with all varactors biased identically directly from the supply lines, and a full hex with independently-controlled varactors. Note the ferrite beads on the supply lines on the two rightmost samples that were required to prevent RF energy from coupling into the supply lines and distorting the measurements.

Measurements of the prototype unit cell yielded valuable information on possible simplifications for the final design. The individual voltage regulators in each unit cell had been included in order to minimize the de-tuning effect of voltage variations throughout the lens due to resistive losses in the PCB traces. However, the extremely low current requirements of the control circuitry limits the possible voltage droop throughout a reasonably-sized prototype lens, and measurements of the prototype metamaterial as well as the varactors showed that the RF response was not sensitive to small changes in supply voltage. The voltage regulator was removed in the revised unit cell design to reduce the number of components, vias, and traces. The resistive voltage dividers included in the original design to provide the 1v and 5v bias levels were also eliminated through the inclusion of an additional -1v supply in addition to +4v and ground. The extra supply line for a prototype not only reduces the component count for each unit cell, but is also beneficial for the ability to independently adjust the on and off bias levels of the varactors for real-time frequency tuning of the metamaterial resonance.

Since a free-space characterization technique was not available to measure the

response of the unit cells directly, two alternative measurement fixtures were fabricated, tested, and used to measure the unit cell response against simulations of the same configuration. The waveguide measurements allowed two-port analysis of the unit cell when exciting the structure with a perpendicular magnetic field the TE10 waveguide mode, and a metamaterial-loaded monopole antenna provided 1-port measurement data as an aid to confirming the simulation results of the waveguide. In addition, several additional microstrip test fixtures were designed and manufactured to assist in characterization of the varactor diodes to correct modeling errors due to insufficient data from the data sheets.

3.3.1 Waveguide test fixture design and construction

A waveguide is the closest configuration possible to the periodic unit cell simulations performed using HFSS without creating artificial magnetic conducting walls to create a more complete equivalent. The hexagonal unit cells may be inserted into the waveguide with the loops oriented perpendicular to the direction on energy flow so that the TE10 magnetic field interacts with the loops. The magnetic field of the lowest-order TE10 waveguide mode is nearly uniform in the center of the waveguide, making it a desirable test configuration. To be an effective measurement system, various geometric constraints exist on the waveguide dimensions. It is desirable that the height of the waveguide be close to or match the height of the hexagonal unit cell, so that the entire unit cell interacts with all of the energy in the waveguide. For this reason, the internal height of the waveguide was fixed at 26 mm . The width of the waveguide a determines the TE10 and the next higher TE20 mode cutoff frequencies according to 3.1.

$$(f_{c,TE})_{m0} = \frac{m}{2a\sqrt{\mu\epsilon}} \tag{3.1}$$

A width of 86 mm yields a cutoff frequency of $(f_c)_{10} = 1.7$ GHz , with $(f_c)_{20} = 3.5$ GHz , with a single-mode bandwidth of 1.7 GHz roughly centered at the 2.5 GHz metamaterial design frequency.

An 86x26 mm waveguide is not a standard waveguide dimension, nor close to a standard dimension of any metal tubes or rods. Thus, a custom-manufactured waveguide was required. Since calibration of the waveguide characteristics to an

internal reference plane would be required, a relatively conventional waveguide system would be required, including bolted flanges and coaxial transitions. The Learning Factory operated by the College of Engineering at Penn State provides students with tools and equipment for metal fabrication, including milling machines and welding equipment. For this project, I became certified for use on the metalworking and welding tools, obtained scrap plate aluminum from the learning factory, and manufactured the custom waveguide that was required for this project. Fig. 3.16 shows the waveguide construction plan and the different pieces required. Four waveguide components were manufactured; two 3.5 mm SMA coaxial-to-waveguide transitions, one short section with longitudinal slots for holding the circuit board, and one long section to be filled with lossy foam to serve as a matched load. The coaxial-to-waveguide transitions were designed using simulations to test the performance of different feed probe designs and locations within the waveguide. Since the waveguide is not of standard dimensions, there were no exact designs available for constructing the transition, which used vertical coaxial probes to excite the waveguide. Simulations showed high sensitivity to the exact position of the probe relative to the shorted termination of the waveguide, so the shorted end of the waveguide transitions were constructed with movable shorting plates that could be adjusted to fine-tune the electrical response of the transitions. The adjustment range was selected by simulations. The length of the coaxial probe was trimmed to give an acceptable response once the waveguide was fully manufactured and characterized using the network analyzer. Images of the construction and assembly process are shown in Fig. 3.17, Fig. 3.18, Fig. 3.19 and Fig. 3.20, and the completed waveguide components in Fig. 3.21. Fig. 3.22 shows the assembled waveguide test fixture with the feed connections and calibration planes for the measurements.
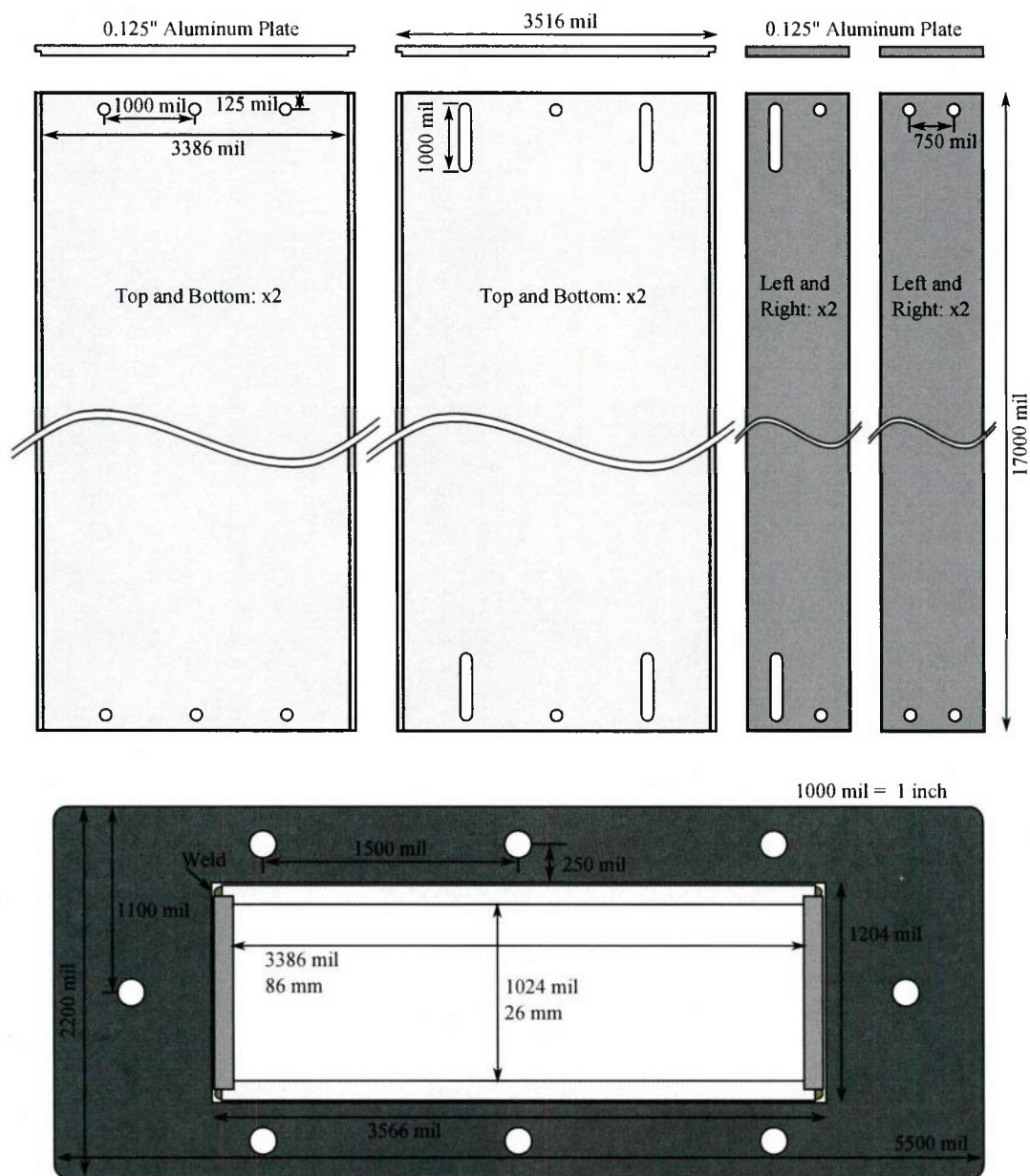
Fig. 3.16: Two pieces each of the top and side panels are needed to construct the four sections of waveguide. The cross-section of the waveguide, including the flange, is shown at the bottom.

(a) Tapping screw holes into the rectangular shorting plate.

(b) Milling out the center of the waveguide mounting brackets

(c) Squaring off the corners of the mounting brackets

Fig. 3.17: Photographs of the waveguide machining process.

(a) Collection of machined pieces, ready for welding.

(b) The four sides of the waveguide are attached to the shorting block by screws to maintain shape during welding.

Fig. 3.18: Photographs of the finished components.

(a) Initial small tack welds secure the waveguide sides without distorting the plates with excessive heat.

(b) After all four corners were tacked, a solid bead was made to finish each joint.

(c) The final waveguide tube has a clean interior, with no burn-through or visible heat-related warping.
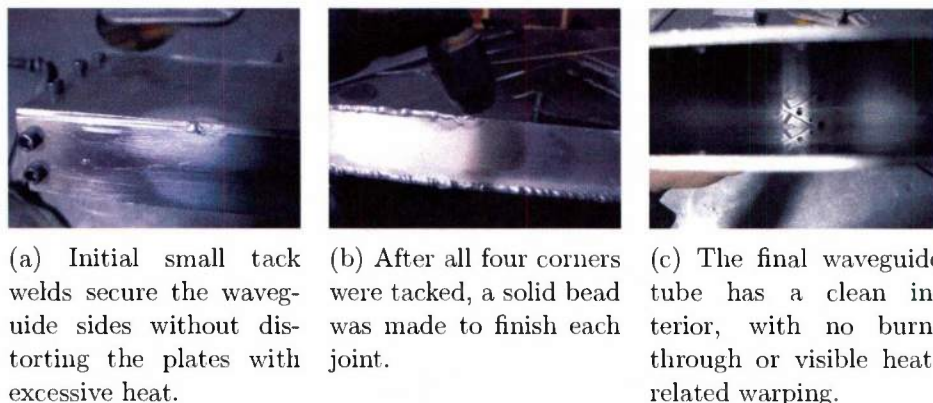
Fig. 3.19: Photographs of the waveguide welding process.

(a) After welding, the corners of the two pieces of waveguide were ground off and rounded.

(b) The two lengths of tubing were divided into four components: two feed sections, a matched load section, and a sample holder.

(c) The shorting block location is controlled with the screw and bracket mounted at the end of each feed section.
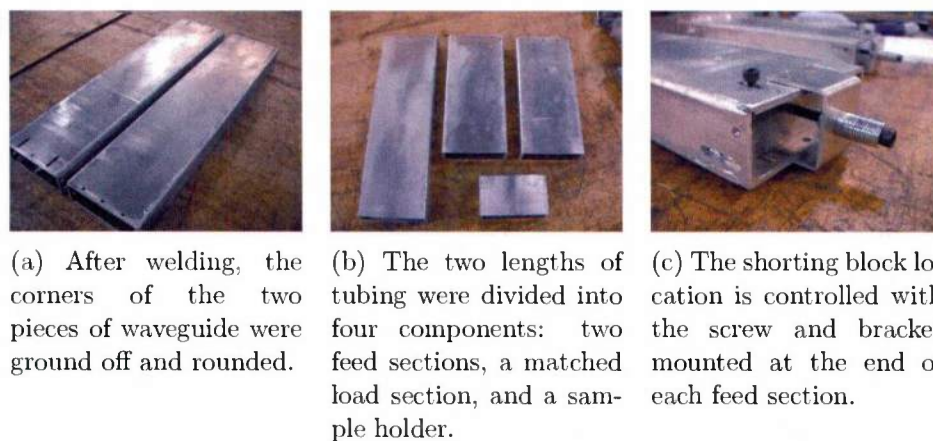
Fig. 3.20: Photographs of the waveguide assembly.

(a) The coaxial probes were extended using wire-wrap connectors to provide better coupling into the waveguide.

(b) The completed waveguide

Fig. 3.21: Photographs of the waveguide.

TRL Calibration Planes

Sample Slot

86 mm x 26 mm waveguide
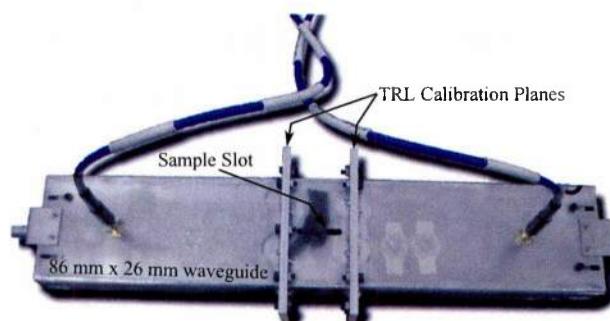
Fig. 3.22: Waveguide measurement configuration.

3.3.2   Monopole test fixture design and construction

Initial measurement results using the waveguide proved difficult to interpret and compare with the simulations until a proper calibration routine was implemented and improved varactor models included into the simulations. Meanwhile, a separate measurement fixture was constructed by loading a resonant monopole antenna with the magnetic metamaterial and comparing the measured and simulated return loss from the monopole. This test fixture was much simpler than the waveguide to design and construct, and easier for results comparison, but also provided less data than the two-port waveguide measurements.

The monopole fixture was constructed from a 140 mm x 140 mm $\frac{1}{16}''$ copper plate, which is approximately one free-space wavelength at 2 GHz . A hole was drilled in the middle of the plate for the probe of an coaxial SMA connector, which was screwed to the plate. Soldering with a conventional soldering iron (the original plan) was ineffectual, due to the massive heat capacity of the solid, thick copper. A 2 mm x 35 mm slot was cut into the plate adjacent to the probe for the metamaterial samples. A long copper wire was soldered to the SMA probe, and trimmed to resonate at 2.8 GHz . The measurements were then performed after performing calibration with the SMA standards. Fig. 3.23 shows photographs of the monopole measurement fixture.

(a)   Original, untrimmed monopole con- nected to network analyzer.

(b) Monopole trimmed to res- onate near the 2.5 GHz fre- quency band for maximum re- sponse

(c) Monopole with loops- only sample
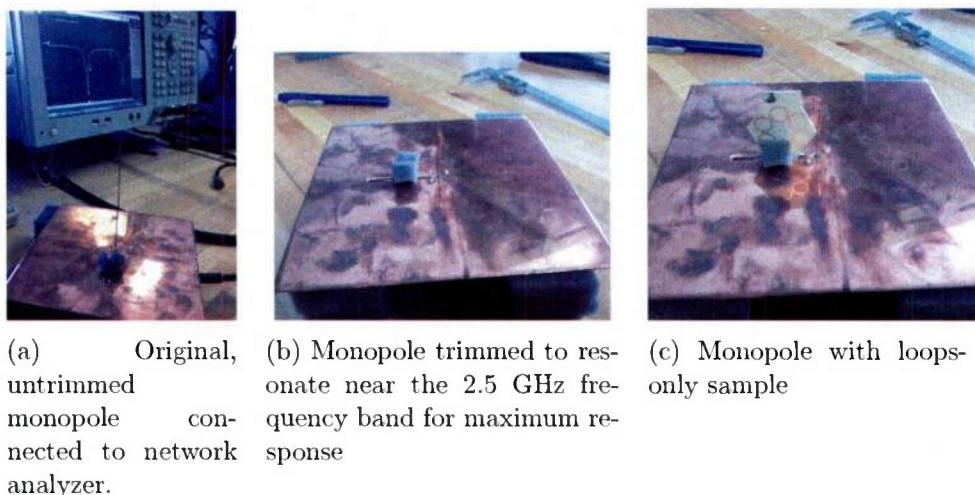
Fig. 3.23: Photographs of the monopole test fixture fabrication and use.

3.3.3 Microstrip bias tee design and construction

Circuit models of the varactors used in the prototype that were constructed using Ansoft Designer and SPICE with the circuit parameters as provided in the manufacturer data sheets were not found to be sufficiently accurate for predictive modeling of the metamaterial response. For this reason (and several other simulation discrepancies) the initial prototype metamaterial that was designed using this inaccurate varactor model did not have the predicted ZIM response when measured. To correct the discrepancy, a microstrip TRL calibration standard and a pair of wideband microstrip bias-tee junctions were designed and fabricated for the 2-3 GHz range. Measurements of the varactor response using these standards were then used for later modeling efforts. The measured scattering parameters of the varactors were incorporated into the HFSS results with the port substitution post-processing technique available using the Matlab RF Toolbox or Ansoft Designer.

In order to measure the varactor response using a microstrip test fixture connected to a network analyzer via SMA connectors, a DC bias needed to be injected into the RF signal. None of the network analyzers that were available included a built-in bias tee junction for that purpose, so a simple microstrip bias tee was designed in Ansoft Designer and fabricated from a piece of Rogers substrate. A bias tee is a three-port network device with ports 1 and 2 connected for RF, ports 2 and 3 connected for DC, and port 3 isolated from RF. They can be constructed from microstrip distributed elements or from lumped elements, but a mixed approach worked best for the relatively low microwave frequencies of interest around 2.5 GHz .

The microstrip design in Fig. 3.24 uses a quarter-wave section of high-impedance microstrip and a pair of fan-shaped wideband quarter-wave shorts to isolate the DC port from the RF lines. The traces were designed for a 31mil Rogers RO5880 RF substrate using Ansoft Designer to compute the trace widths for a good impedance match. Fig. 3.25 shows the predicted scattering response of the design, demonstrating the very high isolation from either of the RF ports to the DC port. The high isolation means that the impedance of the DC source connected to the third port will not affect the RF behavior. There is also very high transmission between the RF ports. A pair of bias tees as well as the microstrip test fixtures for the

varactors were etched on a Rogers substrate, with a photograph in Fig. 3.26, and the measured response of the bias tee shown in Fig. 3.27. There is very good agreement between the predicted response and the measurements, with low return loss surrounding the 2.5 GHz band of interest. The pair of manufactured bias tees was used to measure the varactor magnitude response by calibrating to the tips of the microstrip networks and injecting the same bias level into both sides of the varactor, and used together with the microstrip TRL calibration fixture in order to make accurate measurements of both the phase and magnitude response of the varactors.

During initial measurements of the manufactured bias tees and later of the varactors themselves, it was discovered that the measured response was sensitive to the strain exerted on the test fixtures through the coaxial cables, since the thin and flexible substrate was easily deformed by the stiff coaxial cables. The bias tees were stiffened to alleviate the measurement errors by attaching the substrates to small pieces of aluminum plate with screws.

3.3.4   Microstrip test fixture design and construction

Accurate measurement of both the phase and magnitude responses of the varactor diodes is essential for use of the measured data in the simulations. However, the simple measurement fixtures in Fig. 3.26 are not sufficiently accurate to obtain a good result. Since the calibration planes for the measurement are at the coaxial connectors, not at the pins of the varactor, the phase response is incorrect. Attempts to perform a pseudo-calibration by a simple de-embedding of the additional length of microstrip was not successful. A 50 Ω microstrip calibration fixture was designed and fabricated to correct this deficiency. Using the TRL calibration model, three microstrip standards (thru, reflect, and line) were required. The thru standard requires a microstrip line the same length as the two lines in the measurement fixture. An open (stub) microstrip line, the same length as one of the measurement fixture lines, suffices for the reflect standard. The line standard requires an additional length corresponding to an electrical length 20 to 160 degrees throughout the calibration band, which limits the bandwidth of the calibration standard. Fig. 3.28 shows the fixture design, which contains two mea-
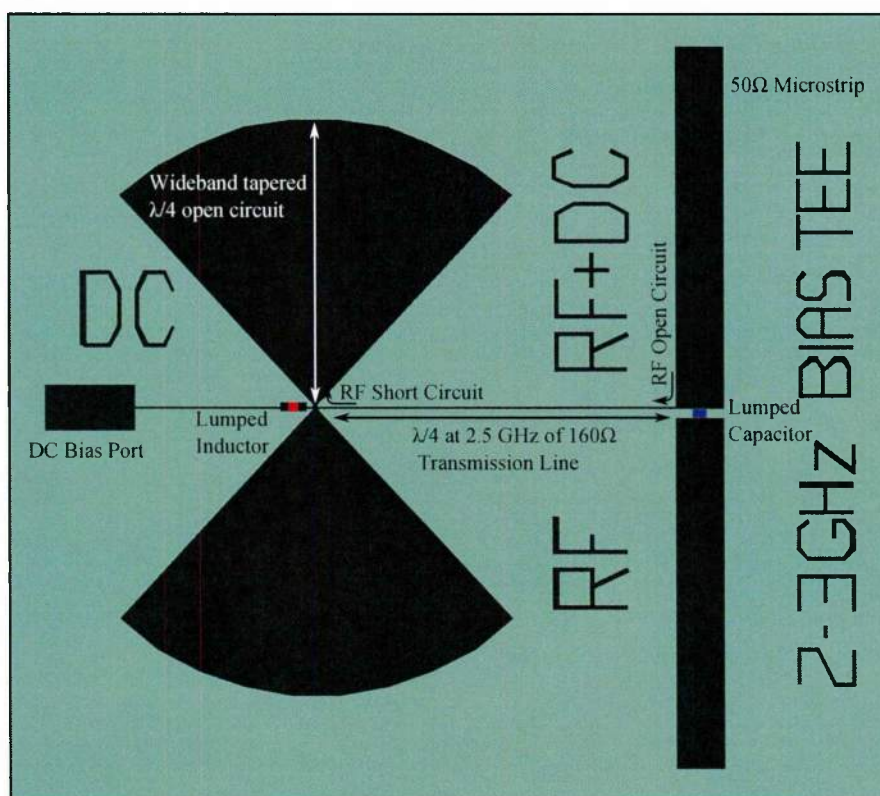
Fig. 3.24: Bias Tee layout and design.
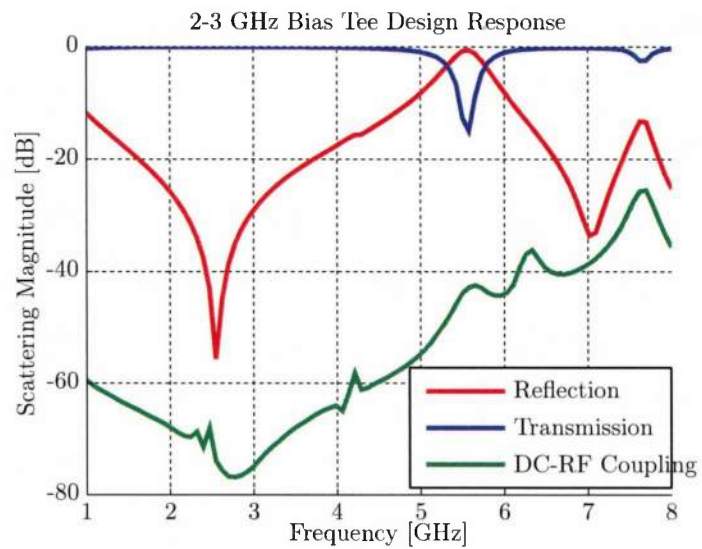
Fig. 3.25: Designed performance for the microstrip bias tee. Note the low insertion loss and extremely high isolation between the RF and DC ports.
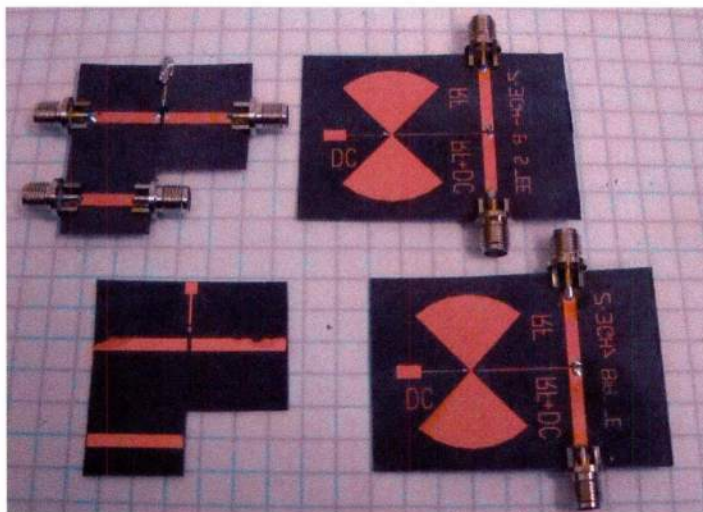
Fig. 3.26: Fabricated microstrip Bias Tee components and initial varactor measurement fixture.
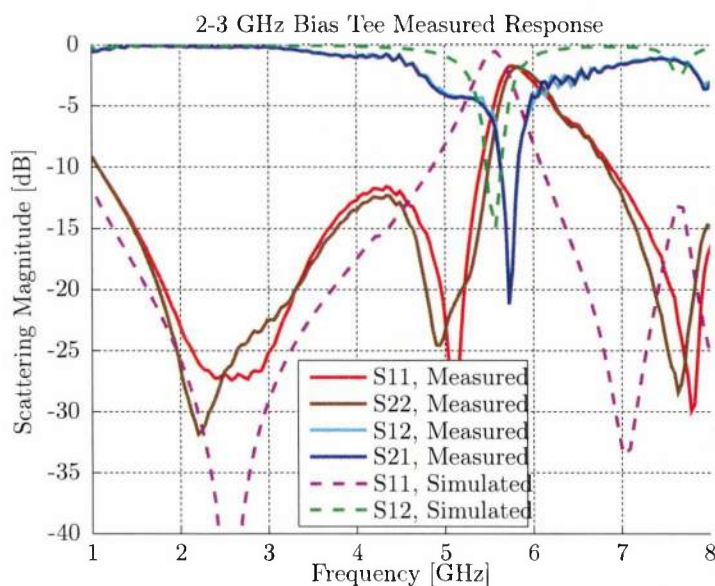
Fig. 3.27: Measured and simulated responses of the bias tee show good agreement and low insertion loss within the 2-3 GHz design band.

surement fixtures for the varactors, two open circuit standards, one line standard, and one thru standard. The design was etched onto a 31mil Rogers RO5880 RF substrate, with the finished structure shown in Fig. 3.29. An aluminum backing was constructed for the microstrip TRL standard to prevent measurement error and uncertainty due to flexing. The TRL standard, together with the previously-constructed bias tees, were used with the standard TRL program included with the network analyzer to accurately measure the scattering response of the varactor diodes.
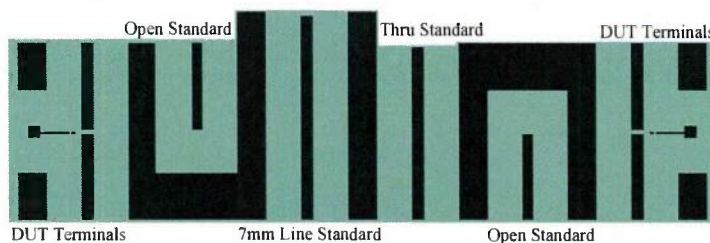
Fig. 3.28: Fabricated microstrip Bias Tee components and initial varactor measurement fixture.

(a) Etched

(b) Machined

(c) Assembled

(d) Measurement Setup
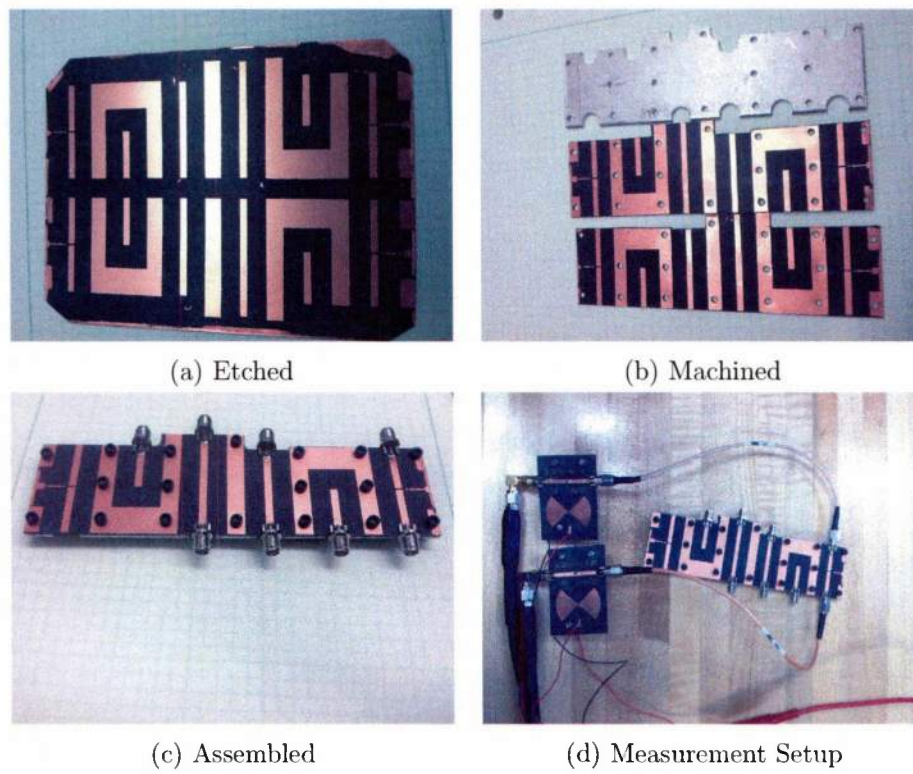
Fig. 3.29: Photographs of the microstrip test fixture fabrication and use.

3.3.5 Measurement and Simulation Deembedding and Calibration

Both the waveguide and the microstrip measurements required calibration for accurate measurements of the response of the metamaterial hex or varactor samples, in order to cancel out the response of the coaxial transitions and other fabrication inaccuracies. Examining the literature showed several possible calibration and pseudo-calibration techniques that had been used for improving measurement accuracy. Due to the simplicity of the mathematical and software implementations, the bisection method was the first attempted [81], [82]. However, this did not yield acceptable results.

The TRL (Thru/Reflect/Line) calibration technique proved to be the best option for calibrating the waveguide and microstrip measurements, in part due to the ability to use partially-characterized and roughly-fabricated calibration standards without loss of accuracy. The built-in TRL calibration routine was used for measurements on the Vector Network Analyzer (VNA), but a custom software implementation was developed for calibration of the simulation results for apples-to-apples comparison to the calibrated measurements. The calibration algorithm is described below. The VNA calibrations of the microstrip and waveguides required different Reflect standards, since an open is best for the microstrip case, and the short used for the waveguide. The original VNA settings expected a short circuit as the reflect standard, which resulted in a phase offset error for the first measurement of the varactor response.

3.3.5.1 TRL Calibration Algorithm

The outline of the following TRL algorithm was pieced together from several sources [83]–[86], none of which provided complete details. Much of the algebra and numeric tests determined during this work.

A VNA measurement M of some Device Under Test (DUT) with response A which is desired to be measured may be written as the cascade connection of three 2-port systems as illustrated in Fig. 3.30, consisting of the two adapter networks X and Y, which contain all of the network analyzer, cable, mounting hardware response, and the DUT. The VNA calibration problem may be expressed as finding

the network descriptions of the two adapters so that the DUT network parameters may be extracted. It is convenient to express the network parameters of the system as T-parameters, so that the cascaded systems may be represented as a product of matrices.

$$M = XAY \tag{3.2}$$

$$A = X^{-1}MY^{-1} \tag{3.3}$$

where the X and Y terminal responses have the form

$$X = \frac{1}{e_{10}} \begin{bmatrix} -\Delta_X & e_{00} \\ -e_{11} & 1 \end{bmatrix} \tag{3.4}$$

$$S_X = \begin{bmatrix} e_{00} & e_{01} \\ e_{10} & e_{11} \end{bmatrix} \tag{3.5}$$

$$Y = \frac{1}{e_{32}} \begin{bmatrix} -\Delta_Y & e_{22} \\ -e_{33} & 1 \end{bmatrix} \tag{3.6}$$

$$S_Y = \begin{bmatrix} e_{22} & e_{23} \\ e_{32} & e_{33} \end{bmatrix} \tag{3.7}$$

and

$$\Delta_X = e_{00}e_{11} - e_{01}e_{10} \tag{3.8}$$

$$\Delta_Y = e_{22}e_{33} - e_{23}e_{32} \tag{3.9}$$
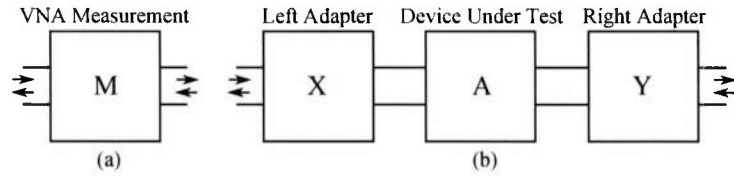
Fig. 3.30: The raw network analyzer measurement data (a) is equivalent to the expanded description in (b), where the original measurement is decomposed into two adapter networks and the DUT network, which is the desired measurement.

The basic calibration technique requires at least three observation of known

DUTs in order to characterize the adapters. Each adapter network has four unknowns, which means that at least eight observations of the system are required to solve the equations. TRL calibration (Thru-Reflect-Line), as the name specifies, requires observations of a Thru standard, a Reflect standard, and a Line standard. The Thru standard directly connects the two adapter terminals with an ideal electrical distance of zero, with T-parameter representation of the DUT called C_{THRU}, and provides four equations to the system.

$$C_1 = C_{THRU} = \begin{bmatrix} 1 & 0 \\ 0 & 1 \end{bmatrix} \tag{3.10}$$

The reflect standard, for which the only constraint is that the standard be highly reflective, typically either a short or an open, has the S-parameter representation $S_{REFLECT}$, which contributes two independent equations. A network with zero transmission does not have a nonsingular T-matrix representation.

$$S_{REFLECT} = \begin{bmatrix} R & 0 \\ 0 & R \end{bmatrix} \tag{3.11}$$

The line standard requires some length of matched transmission line to be inserted between the terminals where the length of the transmission line need not be specified. The line measurement has the representation C_{LINE} Variations of these standards are also possible, including matched loads and multiple line measurements.

$$C_2 = C_{LINE} = \begin{bmatrix} e^{\gamma L} & 0 \\ 0 & e^{-\gamma L} \end{bmatrix} \tag{3.12}$$

Measurements are then made of these three known standards to obtain the required number of observations.

$$M_1 = X C_1 Y \tag{3.13}$$

$$M_2 = X C_2 Y \tag{3.14}$$

$$S_{11}^R = e_{00} + \frac{e_{01} e_{10} R}{1 - e_{11} R} \tag{3.15}$$

$$S_{22}^R = e_{33} + \frac{e_{23} e_{32} R}{1 - e_{22} R} \tag{3.16}$$

These three sets of observations yield a system of 10 equations in 10 unknowns, which may be uniquely solved. Combining the Line and Thru measurements allows the X and Y matrices to be separated.

$$M_2 M_1^{-1} X = X C_2 C_1^{-1} \tag{3.17}$$

$$Y M_1^{-1} M_2 = C_1^{-1} C_2 Y \tag{3.18}$$

Allowing

$$M = M_2 M_1^{-1} \begin{pmatrix} m_{11} & m_{12} \\ m_{21} & m_{22} \end{pmatrix} \tag{3.19}$$

and expanding 3.17 yields

$$\begin{bmatrix} m_{11}x_{11} + m_{12}x_{21} & m_{11}x_{12} + m_{12}x_{22} \\ m_{21}x_{11} + m_{22}x_{21} & m_{21}x_{12} + m_{22}x_{22} \end{bmatrix} = \begin{bmatrix} x_{11}e^{-\gamma L} & x_{12}e^{\gamma L} \\ x_{21}e^{-\gamma L} & x_{22}e^{\gamma L} \end{bmatrix} \tag{3.20}$$

$$m_{11} + m_{12}\frac{x_{21}}{x_{11}} = e^{-\gamma L} \tag{3.21}$$

$$m_{22} + m_{21}\frac{x_{11}}{x_{21}} = e^{-\gamma L} \tag{3.22}$$

$$m_{11} + m_{12}\frac{x_{22}}{x_{12}} = e^{\gamma L} \tag{3.23}$$

$$m_{22} + m_{21}\frac{x_{12}}{x_{22}} = e^{\gamma L} \tag{3.24}$$

Allowing

$$a_1 = \frac{x_{11}}{x_{21}} = \frac{-\Delta_x}{e_{11}} = e_{00} - \frac{e10e01}{e_{11}} \tag{3.25}$$

$$a_2 = \frac{x_{12}}{x_{22}} = e_{00} \tag{3.26}$$

Now, 3.21 and 3.22 may be combined to form a quadratic equation in a_1, and 3.23 and 3.24 form an identical quadratic in a_2.

$$m_{21}a_1^2 + (m_{22} - m_{11})a_1 - m_{12} = 0 \tag{3.27}$$

$$m_{21}a_2^2 + (m_{22} - m_{11})a_2 - m_{12} = 0 \tag{3.28}$$

By duality and starting from 3.18, similar expressions may be written for the

terms of Y,

$$b_1 = \frac{y_{11}}{y_{12}} = \frac{-\Delta_y}{e_{22}} = \frac{e23e32}{e_{22}} - e_{33} \tag{3.29}$$

$$b_2 = \frac{y_{21}}{y_{22}} = -e_{33} \tag{3.30}$$

which, with the definition of

$$N = M_1^{-1} M_2 \left(\begin{smallmatrix} n_{11} & n_{12} \\ n_{21} & n_{22} \end{smallmatrix} \right) \tag{3.31}$$

, have the values defined by the solutions to the following quadratics

$$n_{12} b_1^2 + (n_{22} - n_{11}) n_1 + m_{21} = 0 \tag{3.32}$$

$$n_{12} b_2^2 + (n_{22} - n_{11}) n_2 + m_{21} = 0 \tag{3.33}$$

The two terms a_1 and a_2 (b_1 and b_2) are chosen to be the two distinct roots of the quadratic. Since a_2 (b_2) represents the transmission magnitude and phase of the X (Y) network, a_2 (b_2) is chosen to be the complex root whose magnitude is less than unity. Once a solution is found for a_1, the γL propagation term of the transmission line may be determined.

$$\gamma L = -\log m_{11} + \frac{m_{12}}{a_1} \tag{3.34}$$

Next, the measurements from the reflection standard as in 3.15 and 3.16 are incorporated into the system. These two equations may be rewritten as

$$S_{11}^R - e_{00} - e_{11} \left(S_{11}^R - e_{00} + \frac{e_{01} e_{10}}{e_{11}} \right) R = S_{11}^R - a_2 - e_{11} \left(S_{11}^R - a_1 \right) R = 0 \tag{3.35}$$

$$S_{22}^R - e_{33} - e_{22} \left(S_{22}^R - e_{33} + \frac{e_{23} e_{32}}{e_{22}} \right) R = S_{22}^R + b_2 - e_{22} \left(S_{22}^R + b_1 \right) R = 0 \tag{3.36}$$

$$R = \frac{1}{e_{11}} \frac{S_{11}^R - a_2}{S_{11}^R - a_1} \tag{3.37}$$

$$R = \frac{1}{e_{22}} \frac{S_{22}^R + b_2}{S_{22}^R + b_1} \tag{3.38}$$

Equating both expressions for R yields,

$$\frac{1}{e_{22}} = \frac{1}{e_{11}} \left[\left(\frac{a_2 - S_{11}^R}{a_1 - S_{11}^R} \right) \left(\frac{b_1 + S_{22}^R}{b_2 + S_{22}^R} \right) \right] = \frac{1}{e_{11}D} \qquad (3.39)$$

Next, the reflection from the first port for the Thru standard is incorporated.

$$S_1^{M_1}1 = e_{00} + \frac{e_{10}e_{01}e_{22}}{1 - e_{11}e_{22}} \left(1 - e_{11}e_{22} \right) \left(S_1^{M_1}1 - e_{00} \right) = e_{10}e_{01}e_{22} \qquad (3.40)$$

Then, applying 3.39, we obtain

$$\left(1 - e_{11}^2 D \right) \left(S_{11}^{M_1} - e_{00} \right) = \frac{e_{10}e_{01}}{e_{11}} e_{11}^2 D = \left(-a_1 + a_2 \right) e_{11}^2 D \qquad (3.41)$$

which may be simplified to yield

$$e_{11}^2 = \frac{1}{D} \frac{a_2 - S_{11}^{M_1}}{a_1 - S_{11}^{M_1}} \qquad (3.42)$$

$$e_{11} = \sqrt{ \left(\frac{a_2 - S_{11}^R}{a_1 - S_{11}^R} \right) \left(\frac{b_1 + S_{22}^R}{b_2 + S_{22}^R} \right) \left(\frac{a_2 - S_{11}^{M_1}}{a_1 - S_{11}^{M_1}} \right) } \qquad (3.43)$$

When implementing 3.43 in a numeric TRL algorithm over a frequency range, care must be taken to obtain the correct complex branch of the square root for each continuity in the transmission phase. It is recommended to compare both the positive and negative roots of 3.43 to the previous frequency point, and to choose the root that gives the smallest difference in a magnitude sense.

With a_1, $a_2 = e_{00}$, b_1, and $b_2 = -e_{33}$ known, e_{11} may be found by 3.43 and used in 3.39 to find e_{22}. Then, the products $e_{10}e_{01}$ and $e_{32}e_{23}$ are found by

$$e_{10}e_{01} = \left(a_2 - a_1 \right) e_{11} \qquad (3.44)$$

$$e_{32}e_{23} = \left(b_1 - b_2 \right) e_{22} \qquad (3.45)$$

$$\qquad (3.46)$$

Since e_{10} and e_{32} appear only as uniform scaling terms in X and Y, expressions for those values in isolation are not required. Thus, all terms necessary to construct the X' and Y' matrices have been obtained.

$$X' = \begin{bmatrix} e_{10}e_{01} - e_{00}e_{11} & e_{00} \\ -e_{11} & 1 \end{bmatrix} \tag{3.47}$$

$$Y' = \begin{bmatrix} e_{32}e_{23} - e_{22}e_{33} & e_{22} \\ -e_{33} & 1 \end{bmatrix} \tag{3.48}$$

$$\tag{3.49}$$

The correct scaling for the X and Y matrix may be corrected by computing the scale factor s

$$(X')^{-1}M_1(Y')^{-1} = sI \tag{3.50}$$

and X and Y are produced accordingly to yield a passive DUT system response.

$$X = \sqrt{s}X' \tag{3.51}$$

$$Y = \sqrt{s}Y' \tag{3.52}$$

The expressions as related above may be (and have been) implemented in a loop for computing calibration coefficients over an array of frequency points, while taking care when selecting the proper complex roots of the square root and quadratic expressions. The calibration constants may be preserved and applied to multiple measured data sets that use the same test fixture. The calibration is applied to individual frequency samples as

$$T_{DUT} = X^{-1}T_{MEAS}Y^{-1} \tag{3.53}$$

where the network responses T_{DUT} and T_{MEAS} are expressed as T-matrices. This procedure was applied to simulated waveguide responses using coaxial feeds and different models for the Thru, Line, and Reflect standards with reasonable success, which was evaluated through comparison to measured results with TRL calibration applied at the time of measurement by the network analyzer.

This represents a very simple TRL procedure; more sophisticated algorithms

exist that are capable of using more than three standards or incorporating redundant measurements to reduce error and the effects of noise.

3.3.6 Varactor Characterization

The SMV1247LF common-cathode varactors were characterized with the help of the manufactured bias tees and microstrip TRL calibration standards. The calibration was performed using the built-in VNA TRL calibration procedure and included the bias tees; Fig. 3.29 includes a photograph of the measurement setup.

The two-port responses of the common-cathode varactors are shown in Fig. 3.31. The single-port ground-terminated response, as required for the port substitution procedure, is included in Fig. 3.32.

In addition, the response of a single varactor was also measured, for additional confirmation of simulation results. The shorted response of the single varactor is included in Fig. 3.33. This response was used in some simulations that required the separation of the common cathode varactor into two pieces so that the electrical connection to the cathode pin could be accurately modeled.

3.3.7 Modeling refinements

Initial simulations of the hex in either the waveguide or monopole configuration did not demonstrate close agreement with the measurements. Partially, this was alleviated in the case of the waveguide measurements through the introduction of a working TRL calibration routine to both simulations and measurements, as previously described. The initial varactor model also had a large, detrimental effect on the modeled responses. However, even after calibration and the measured varactor models were incorporated there were still significant disagreements in the simulations compared to the measurements, manifested as frequency shifts, missing resonances, large magnitude response discrepancies, and missing phase response features. The simulation model was iteratively improved by starting with the unpopulated circuit board model next to the probe measurement fixture, and making changes to incorporate geometry features that had originally been ignored or deemed unimportant.
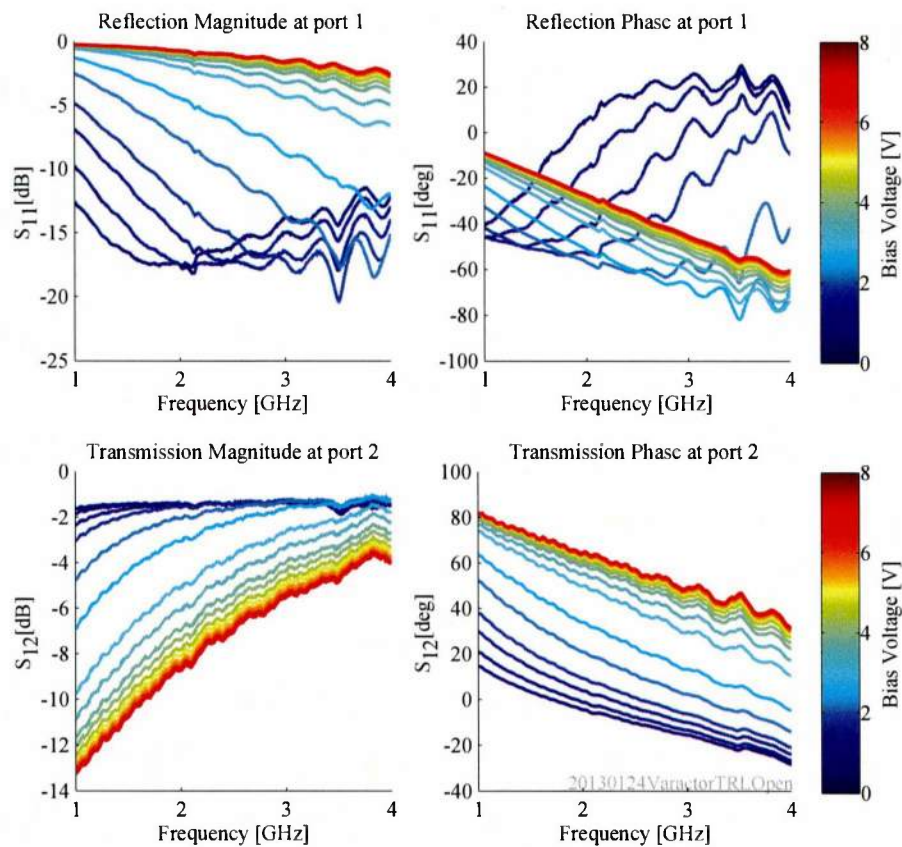
Fig. 3.31: Measured two-port scattering data for the common cathode varactor diodes, as measured using the bias tee, microstrip test fixture, and TRL calibration procedure on the network analyzer. The scattering from the second port is effectively identical.
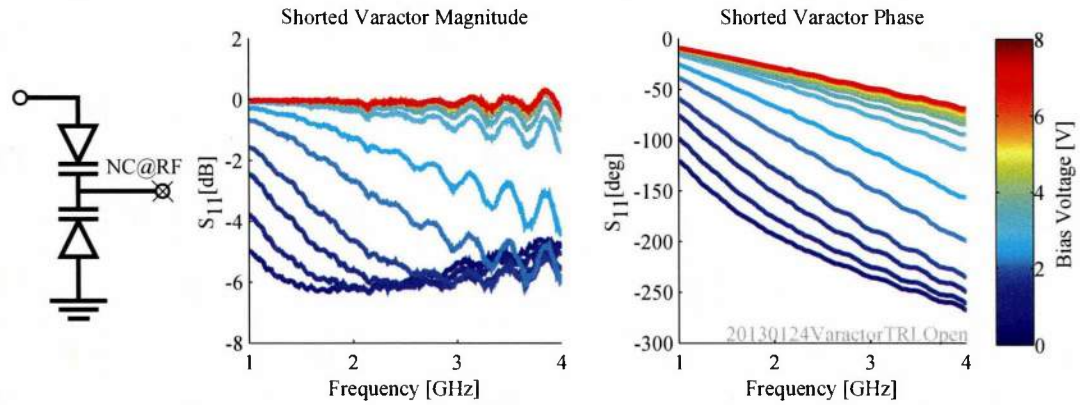
Fig. 3.32: Measured reflection magnitude and phase of the common-cathode varactor when the second terminal is shorted to ground, as required for application of the port substitution technique.
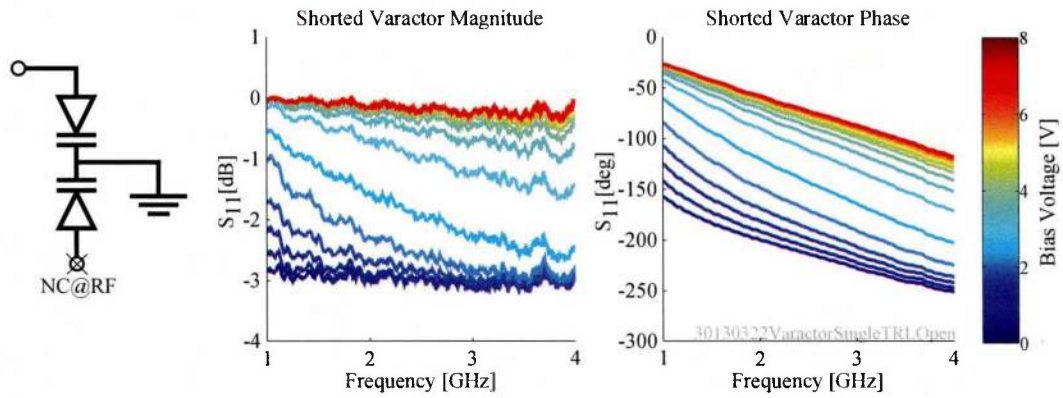
Fig. 3.33: Measured reflection magnitude and phase of the individual varactors when the second terminal is shorted to ground, as required for application of the port substitution technique.

3.3.7.1   Increase simulation resolution

The first step was to increase the mesh refinement condition to ensure that the adaptive mesh used by HFSS had converged. I increased the meshing tolerance significantly, but the results did not change significantly. This indicates that the results were converged in the original model.

3.3.7.2   Trace material

Although the dielectric was correctly modeled as lossy FR4, the traces were modeled as PEC impedance conditions. In many radio-frequency and microwave metamaterial simulation, PEC is a good approximation, but the additional slight loss given by modeling as finitely-conducting copper rather than perfectly conducting material did yield a change in the response, although not large enough to justify the original error in the modeled results.

3.3.7.3   Dielectric boundary

The models have always assumed a perfect hexagon of dielectric hosting the loops and control circuitry, with small tabs on top and bottom with the power and data lines. It had been assumed that the small amount of excess dielectric remaining when cutting the sample into a square rather than a hexagon would not affect the results, but it did. Since one corner of the hexagon had been cut (as in figure), I included the three corners of the dielectric into the model. This resulted in another small but significant shift in the response.

3.3.7.4   Soldermask

The soldermask quantity and properties proved to have one of the larger influences on the frequency shift. The thin layer of soldermask on the commercially produced circuit board has a lossy effect on the microwave signals, and also slightly changes the impedance, since the loops are now embedded in a layered dielectric media, rather than free space.

The tests started by adding a relatively thick soldermask ($50\mu m$); this was too thick, and shifted the response too low. The soldermask was modeled as a volumetric block of material. Thinner soldermasks could not be modeled accurately

as volumetric blocks, but instead were implemented using a surface impedance approximation method, as provided by the layered impedance model in HFSS. The original impedance model only placed soldermask over the dielectric regions, since the traces were already modeled as surface impedance boundary conditions. For this case, $25\mu m$ of soldermask material was required. Later, I used the HFSS layered impedance model to include both the copper traces and the soldermask above them. With the soldermask over the copper, only 10 μm of the soldermask was required to get good agreement with the measurements.

3.3.7.5   Hex cell orientation

The orientation of the unit cell relative to the feed probe turned out to be important. Since the hex is not rotationally symmetric due to the control circuitry and rotated loop orientation relative to the hex walls, the monopole probe interactions change slightly with the orientation of the sample. After re-checking the orientation of the hex that was used for the measurements, I changed the simulation and obtained much better agreement in the low frequencies below the main resonance.

3.3.7.6   Single-varactor measurements

The initial calibrated measurements of the common cathode varactor diodes used a test fixture that allowed biasing of the cathode pin while measuring the response between the two anode pins. It was assumed that, since the varactor characterization was performed in the same configuration as in the actual metamaterial, that this would be accurate. However, when performing a sensitivity analysis of the revised metamaterial response to the inductance between the loops, there was a significant effect for the inductance values that were used in the initial design. This implied that some of the current from the loops was leaking through the cathode port of the varactor past the blocking inductors, and could be affecting the metamaterial response. To test this theory, I numerically separated the measured varactor response (considered as T-matrices) into two halves, to obtain the effective response of the individual varactors, rather than the combination of both devices.

$$T_{CC} = T_{var}T_{var}^{-1} \qquad (3.54)$$

This equation was solved for T_{var}, the single varactor response at each frequency point, using a nonlinear solver in Matlab given the common cathode response T_{CC}. After converting the metamaterial model in HFSS to include a third pin to serve as the varactor cathode, I modeled each of the three-pin varactors as two separate ports, one for each individual varactor. This revised modeling approach showed substantially closer agreement to the measurements of the hex response. To confirm that the differences between the original single-port varactor simulations and the new simulation results were not artifacts of the numeric scattering response extraction, I measured the single-varactor response using the same calibration and measurement setup as before (response in Fig. 3.33) and obtained practically identical results to those of the numerically-separated varactor response. This result indicates that the single-varactor model should be used for the design of future metamaterial revisions, so as to incorporate the effects of unitcell-unitcell coupling through the cathode ports and blocking inductors.

3.3.7.7   Summary of changes

As a result of these studies, some new parameters or geometric features of the metamaterial are known to be very important in obtaining a good simulation model. First, the metals should be properly modeled, not left as PEC. The dielectric should be completely modeled, including corners and notches. The soldermask was critically important, and should be a controlled quantity for the full design to prevent additional frequency shifts and performance mispredictions. As much as is possible, the thickness and dielectric properties of the soldermask as well as the dielectric and trace material should be known for inclusion into the model. Measurements of the individual varactors should be used, instead of the series measurements through the anode ports, as in the initial measurements. Finally, the orientation of the asymmetric hex should be exactly matched in the simulations to the measurement configuration. These updates to the original model, in combination with the measured varactor properties and calibration procedure, allow for accurate predictive simulations to be performed for the metamaterial behavior.

3.3.8 Waveguide measurements

For accuracy, the waveguide simulations were performed using the single-varactor model, as discussed above. The simulations modeled the same waveguide structure and unit cell design as were measured by the network analyzer. Since the simulation cannot model the fabricated design exactly, especially the feed probes, due to manufacturing inaccuracies and errors, a two-port TRL calibration was performed on both the measured and simulated data to remove the effect of the cables and coaxial cable-to-waveguide transitions. Measurements were performed of the unpopulated unit cell, as well as the populated unit cell with variable bias voltage. It was found during the course of the measurements that the orientation of the unit cell in the waveguide makes a significant difference in the reflection response, and that this orientation must be matched in the simulations in order to obtain agreement in the results. The variable voltage measurements were performed by placing the sample in the waveguide slot, incrementally increasing the bias voltage by 1v intervals, and capturing data at each point. Lack of any hysteresis behavior was verified by comparing the response when increasing to the response when decreasing the bias level. The measured and simulated data are compared in Fig. 3.34, showing acceptable agreement between the prediction and measurements. The transmission measurements agree better than the reflection measurements.

Several iterations of prior waveguide measurements and simulations were performed, but are not shown here due to poor agreement with simulations. The addition of the TRL waveguide calibration procedure and the modeling refinements as described above yielded a much closer comparison between the measurements and simulations.

3.3.9 Monopole measurements

The test fixture was manufactured with a four-inch monopole, which was trimmed to a one-inch monopole by small increments while examining the single-port response of the fixture with the network analyzer. The monopole length was shortened to bring the return loss minima up to approximately 2.75 GHz , where there would be maximum interaction of the radiated field with the metamaterial sample
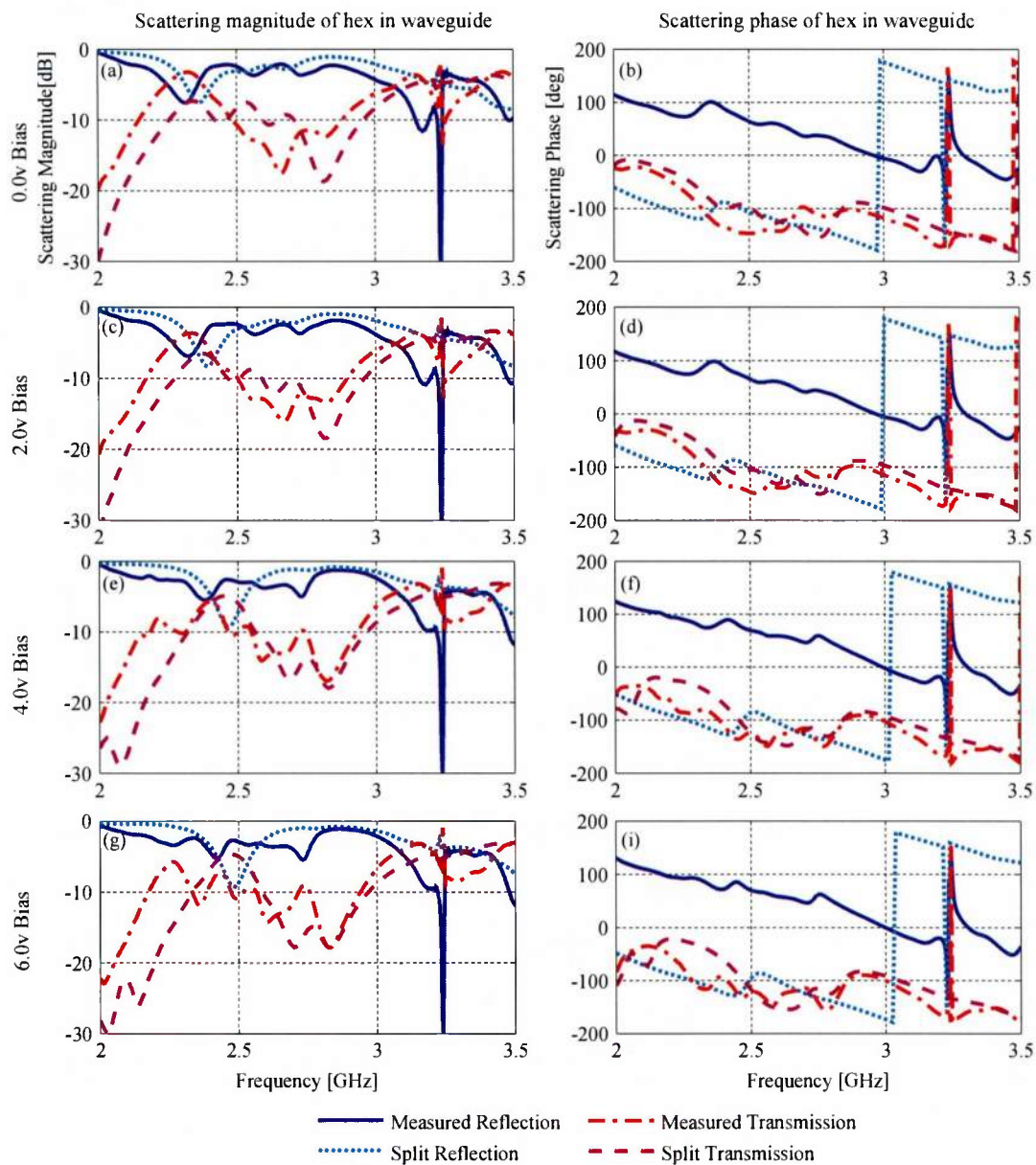
Fig. 3.34: Phase and magnitude scattering response of the populated hex prototypes in the waveguide test fixture, with acceptable agreement between the measured and simulated data.

under test. See Fig. 3.23 for the measurement configuration.

The measurements have a different electrical path length in the feed probe, which is accounted for by a shift of 18 degrees in the measured relative to the simulated results in all of the relevant figures. The phase shift correction was accomplished by comparing the measured to the simulated response of the monopole alone, and adding phase until the plots coincided, as shown in Fig. 3.35. With this sole correction, the response of the monopole in Fig. 3.35 agrees closely with the simulated response.

Three unit cell samples of the split rings alone were manufactured on a high dielectric constant (25 mil RO6010, $\epsilon = 10$) substrate (as described in Fig. 3.15) and used to confirm the simulation model for the monopole test fixture, with the measurement and simulation results shown in Fig. 3.36, Fig. 3.37, and Fig. 3.38. The measurements show good agreement with the simulations, given the coarse fabrication tolerances achieved, and several important factors relating to the measurement system were determined. The first sample with dual-sided loops in Fig. 3.36, for example, required the model to match the orientation of the measurement, and it was found that the front and back sides of the copper on the sample were not precisely aligned. Placing a linear offset between the front and back of 0.7mm improved the simulated response compared to the original simulation. Fig. 3.37 and Fig. 3.38 demonstrated sensitivity to measurement position, and there were tendencies in all of the simulations to miss narrow secondary resonances with small changes in modeling parameters. Through the simulations, it was determined that using copper rather than PEC to model the traces was required for maximum accuracy, which was not expected to be important for the operational frequency range.

Measurements and simulations of the populated and unpopulated prototype metamaterial hex showed good agreement, thanks in part to the tighter fabrication tolerances of the externally-produced samples. Fig. 3.39 shows very close agreement for phase and magnitude of the measured and simulated response for the unpopulated hex made with copper traces and including the soldermask effects. The comparison for the populated and voltage-biased boards in Fig. 3.40 is also quite close, showing that the model revisions and corrections have been successfully applied.
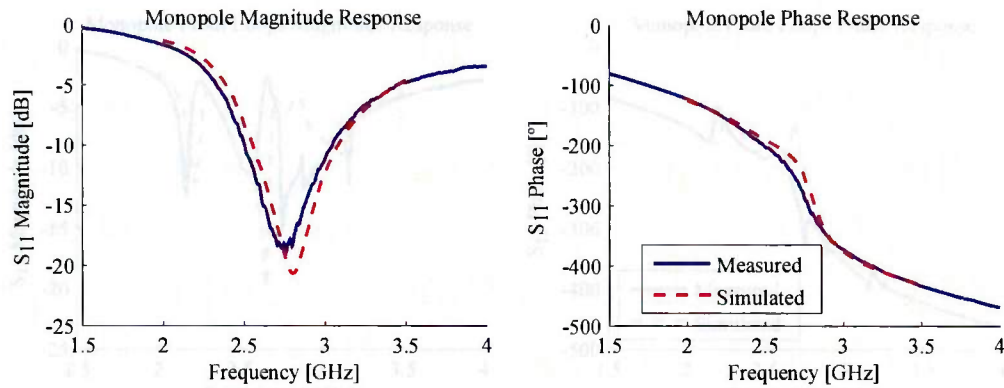
Fig. 3.35: Measured and simulated response of the monopole test fixture showing good agreement.
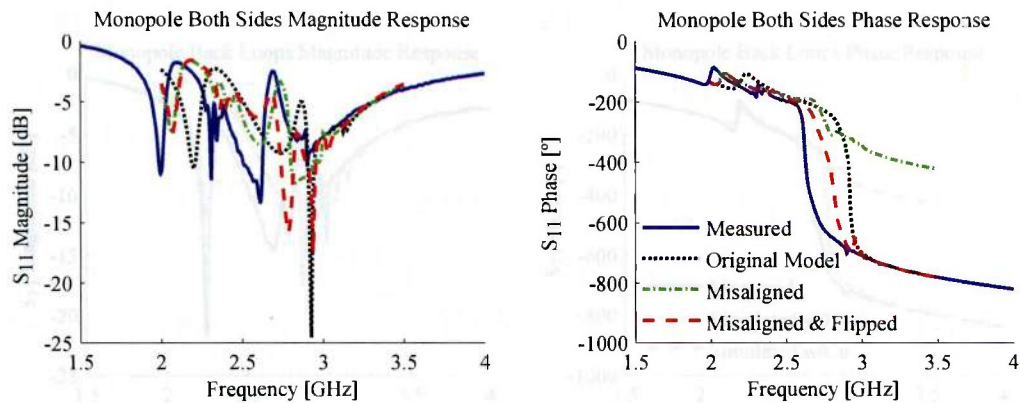
Fig. 3.36: Measured and multiple simulated responses of the dual-sided loops-only sample. The final misaligned and flipped model shows the best agreement with the measurements, with the front loops shifted by 0.7 mm relative to the back. The results show good agreement in both magnitude and phase, with a slight frequency shift due to the loose tolerances.
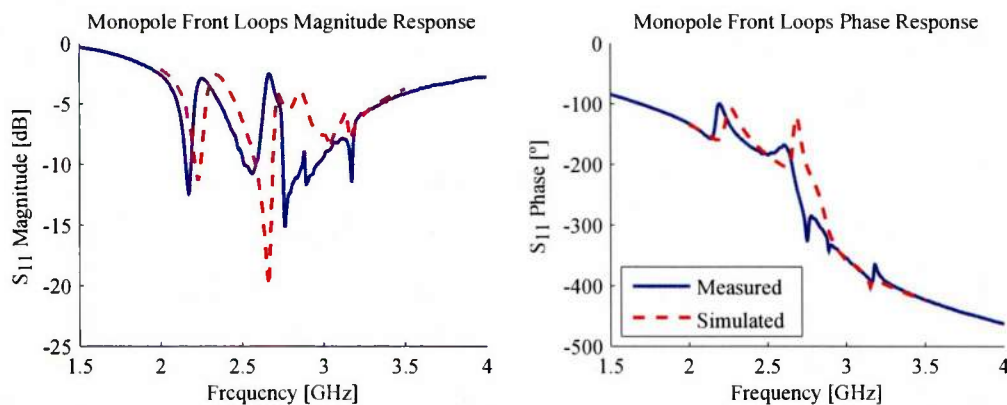
Fig. 3.37: Measured and simulated responses of the sample with only the front loops. This sample shows good agreement with only a small frequency shift.
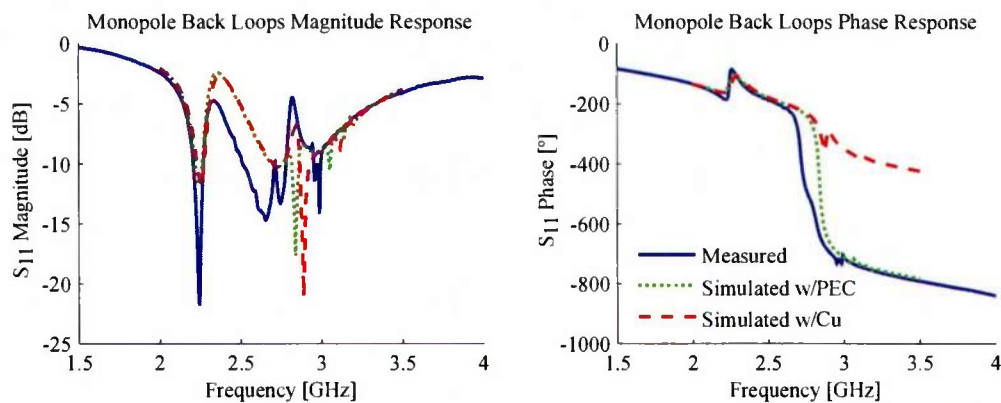
Fig. 3.38: Two simulation results are shown, one with PEC traces and the other with copper. The copper magnitude response matches better, but misses the second large resonance at 2.75 GHz . This resonance is not consistent, and does not appear in all measurements or all simulations.
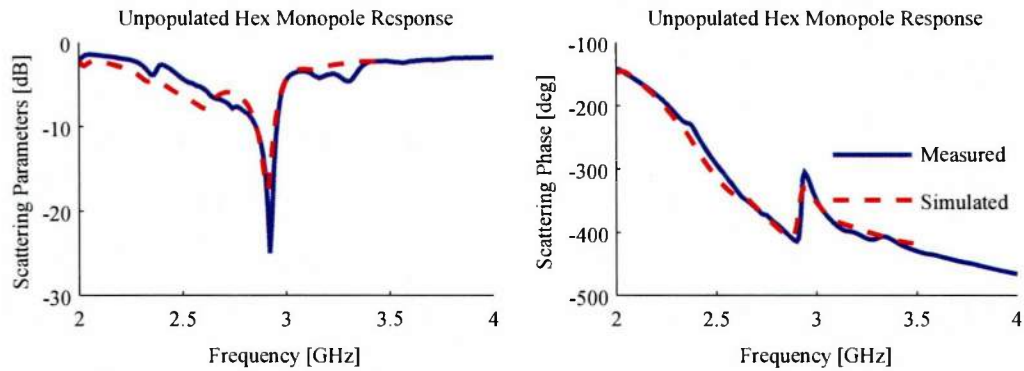
Fig. 3.39: The measured response of the full hex circuit board is shown with the final simulation results, with good agreement.
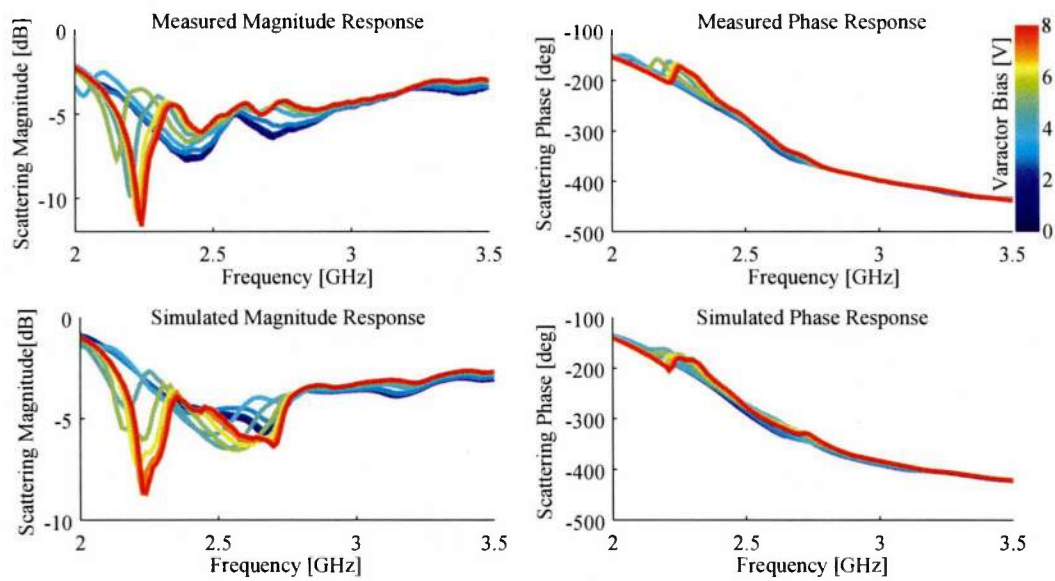
Fig. 3.40: The measured and simulated responses of the full populated hex, swept with respect to the varactor bias voltage. The measurements and simulations show broad agreement.

3.4 Design revisions

With the simulation models and measurements of the prototype metamaterials brought into agreement, the previously-discussed design and simulation rules obtained during the refinement process were applied to new designs to optimize the performance.

The same metamaterial design procedure and hex modeling procedures were repeated with the updated varactor models to obtain the final metamaterial prototype prior to full lens fabrication. Specifically, simulations of the loops alone were run with the measured varactor response before performing the PCB layout with the full control circuitry and re-simulating to confirm the correct performance. Using the measured varactor response and the original dimensions of the unit cells (15 mm side lengths, 8mm loops) resulted in a ZIM frequency response that was too low, at about 1.8 GHz . The hex cells were reduced in size to an edge length of 11.5mm and a loop outer diameter of 6.5 mm in order to push the resonant frequency in the periodic simulation to 2.2 GHz . No further size reduction was possible, based on the control circuitry area requirements and the size of the components. The reduced control circuitry requirements as determined by the results of the initial prototype testing allowed the reduced-size unit cells while also reducing the designs from four to two layer printed circuit boards, which reduced the fabrication cost. Simplifying the control circuitry by eliminating unneccesary components substantially reduced the manufacturing cost and trace density of the unit cells as seen in Fig. 3.41 compared to the original prototype, increasing manufacturing feasibility and reducing the effect of the excess traces on the metamaterial response.

Simulations of the hex cell with and without the control circuitry shows only small differences between the full and loops-only designs. For the full design, the inter-loop inductance proved to be an important parameter. Parameter studies showed that the inductance should be at least 200nH for this operational frequency in order to completely isolate the rings (Fig. 3.46). This result, which was discovered during the design of the second prototype metamaterial, is probably a significant reason for the large change in predicted effective material response between the loops-only and full design for the initial tunable metamaterial prototype,
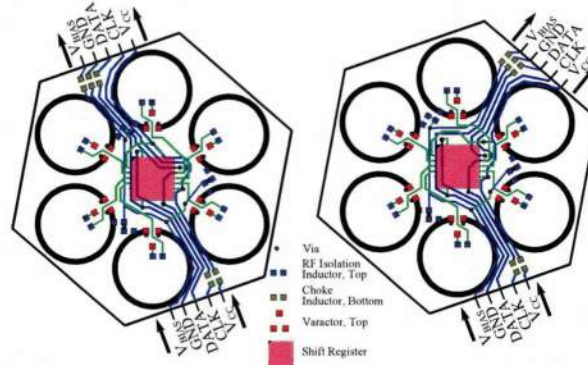
Fig. 3.41: Example hexagonal unit cell layout for the straight (left) and curved (right) configurations. Low current requirements allow thin traces to be used. Inductors are placed at the boundaries of the unit cells to reduce RF coupling. These two unit cells may be cascaded to form a space-filling hexagonal spiral lens.

which used 68nH inductors. Fig. 3.42 shows the final hex cell layout.
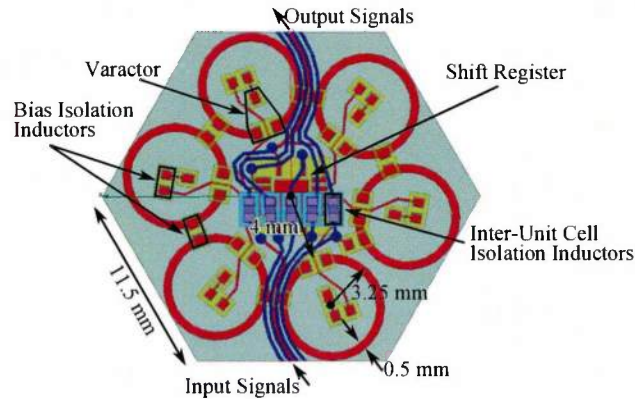
Fig. 3.42: Reconfigurable unit cell geometry and board layout. Red and blue are top and bottom copper layers, while yellow and cyan are the top and bottom soldermask layers, respectively.

After conversing with PCB manufacturers and receiving high (~$24k) initial manufacturing quotes, the lens was restricted to only a nine-hex radius, a Rogers RO3003 substrate was selected instead of Rogers RO5880, and the center three rings of the lens were replaced by static (non-tuning) hexes. These changes were intended to reduce the fabrication cost of the lens prototype by about 30-50%,

which was successfully achieved for the resulting quote of $14k. This lens config-
uration is illustrated in Fig. 3.43.
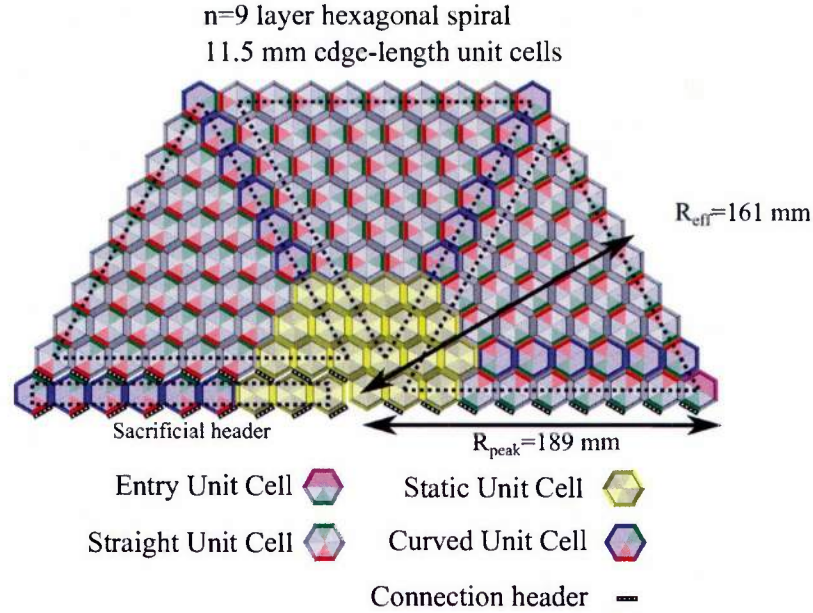
Fig. 3.43: To reduce the fabrication expense, the inner three layers of reconfigurable
unit cells were replaced by static ZIM unit cells, and the lens size reduced to a
radius of nine unit cells.

The static metamaterial design was performed in the same way as the tunable
metamaterial, except that there were no lumped elements in the design. Several
variations were attempted on the simple loops with a single break, including con-
centric loops, loops with multiple gaps, loops with capacitive arms extending both
into and out of the loop body, and adding an additional loop into the center of the
hex. The successful design used loops with long, parallel capacitive arms added
to the gap in the ring. A rectangular patch was placed on the back of the board
beneath the capacitive arms to enhance the capacitive effect. The final dimensions
for the static design are shown in Fig. 3.44, which produces the permeability curve
in Fig. 3.45, which is plotted for comparison with the permeability of the full hex
design.

During simulations on the final metamaterial design, several values of induc-
tance were tested to determine the effects on the response, as plotted in Fig. 3.46.
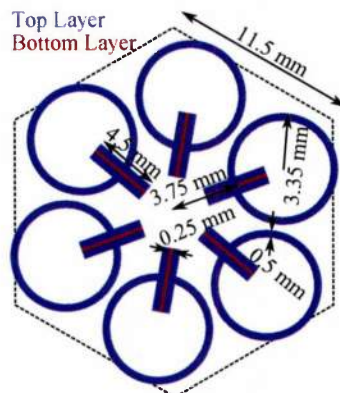
Fig. 3.44: Dimensions and layout of the static hex unit cell used for the inner three layers of the lens to reduce the cost of the lens construction.
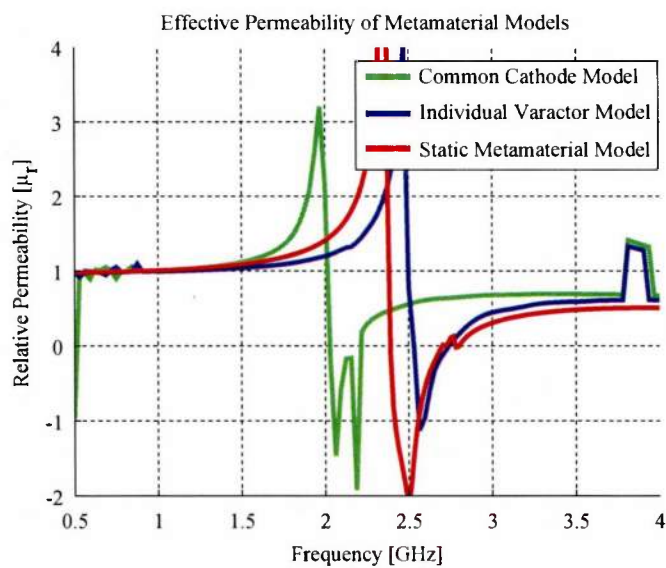
Fig. 3.45: The static metamaterial design was tuned to exhibit a ZIM condition below the predicted resonant frequency of the full reconfigurable hex, so that the final design may be tuned appropriately.

Increasing the inductance to be greater than 200 nH produced negligable changes, and any inductance greater than 100nH was acceptable, but the effects of overly low inductance were very severe. The initial inductor size was chosen based on the impedance of the inductor at 2.4 GHz , but the simulations of the actual unit cell showed that a larger value was needed, and the inter-loop inductors were increased to 200nH. High DC resistance is acceptable for these components, since their only purpose is to communicate a DC bias voltage to the varactor, with zero or nearly zero leakage current.

3.4.1 Voltage Regulator and Level Shifter

In the revised design, both the high and low bias voltages are supplied from outside the lens, with the unit cells only switching between the two levels. Also, the MSP430 microcontroller used for directly supplying the clock and data signals to the lens operates at 3.3v logic levels. A separate circuit board was designed and constructed in order to supply the required voltage levels to the lens while allowing for tuning without using multiple lab bench power supplies, as well as provide the level shifting between the 3.3v and variable voltage signals required by the shift registers. The circuit diagram is included in Fig. 3.47, and an image of the circuit board layout in Fig. 3.48. Two potentiometers are included to allow independent tuning of the -1v and 4v voltage regulators for fine-tuning the ZIM resonance frequency of the lens. Through-hole components were selected to simplify hand assembly, and the actual board will be fabricated on the LED board and separated after assembly.
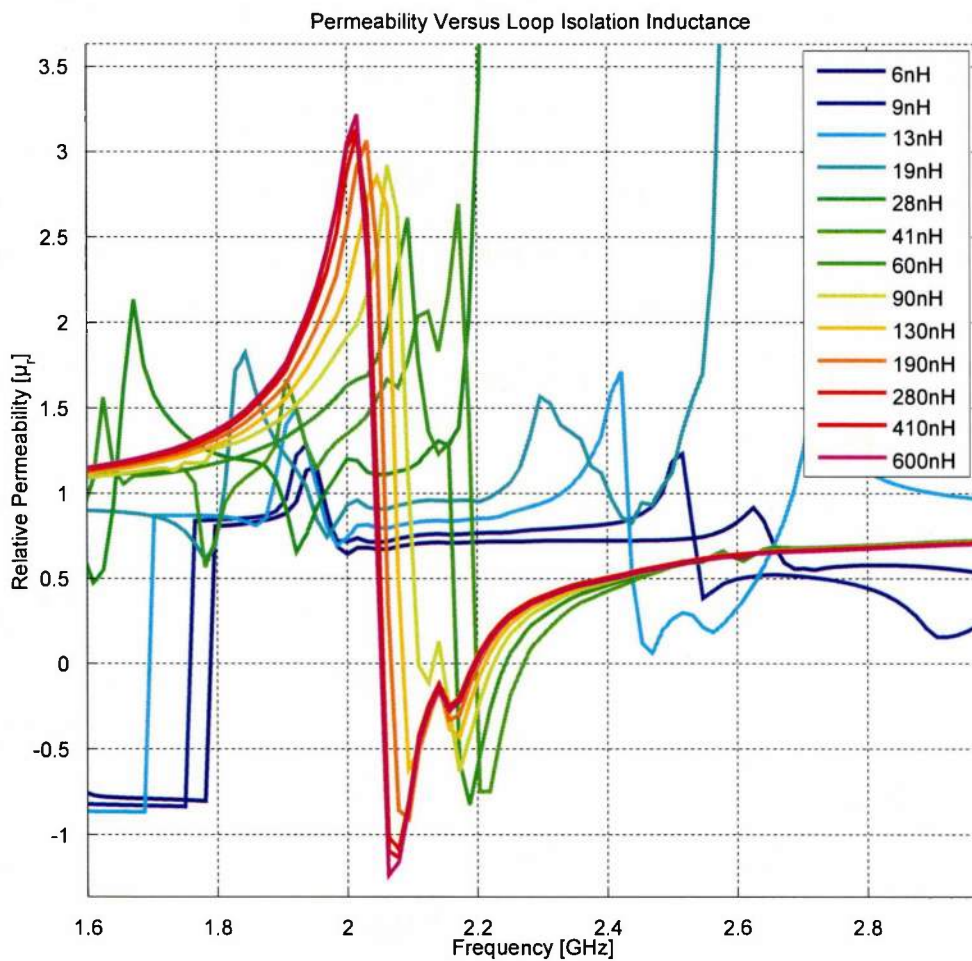
Fig. 3.46: The blocking inductor must be at least 100nH in order to obtain a good permeability response; lower values of inductance allow too much coupling between the loops.
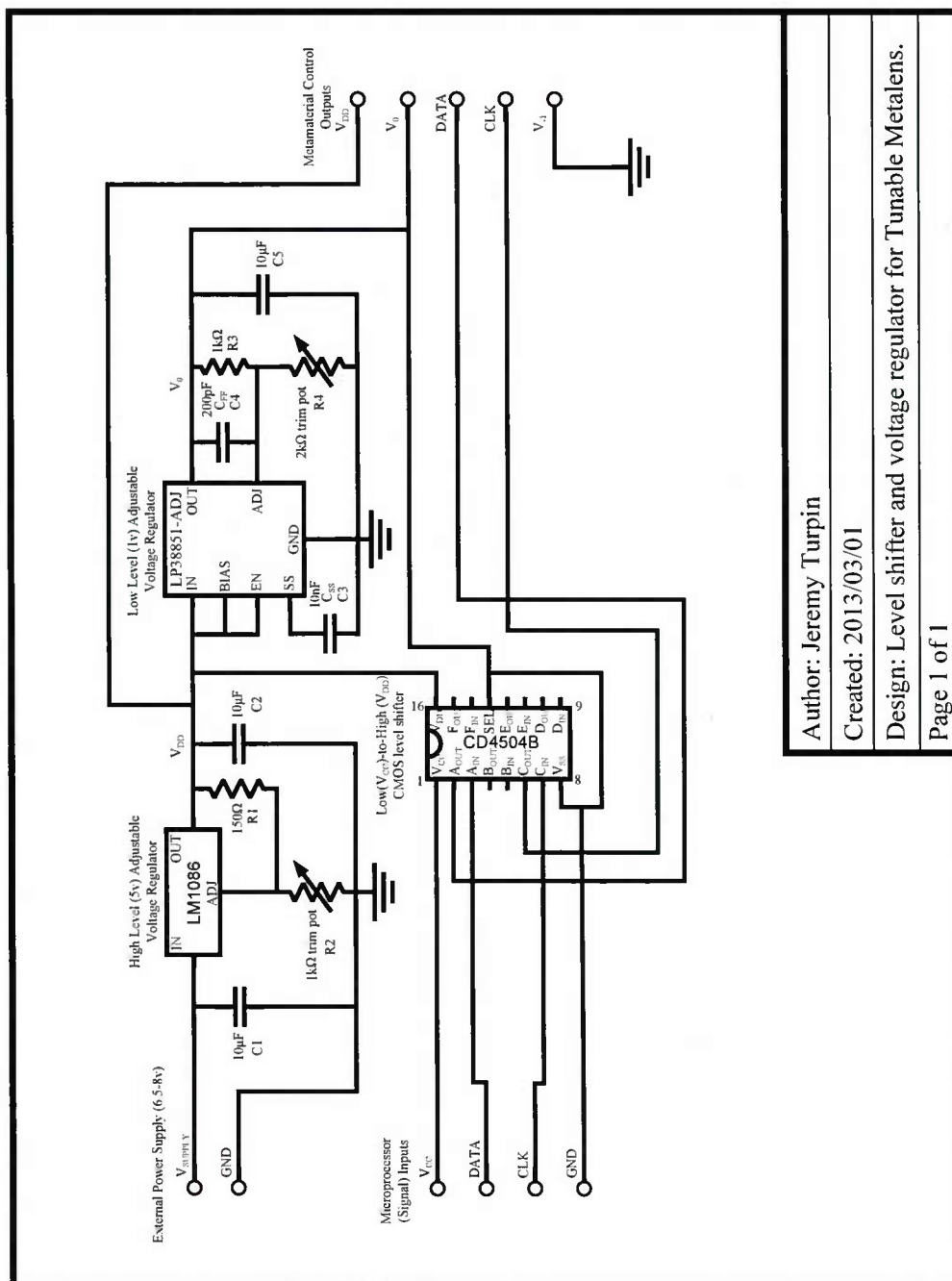
Fig. 3.47: Voltage regulator and level shifter circuit schematic that allows the tuning of the -1v and 4v varactor bias levels via two potentiometers for fine-tuning the resonant frequency of the lens.
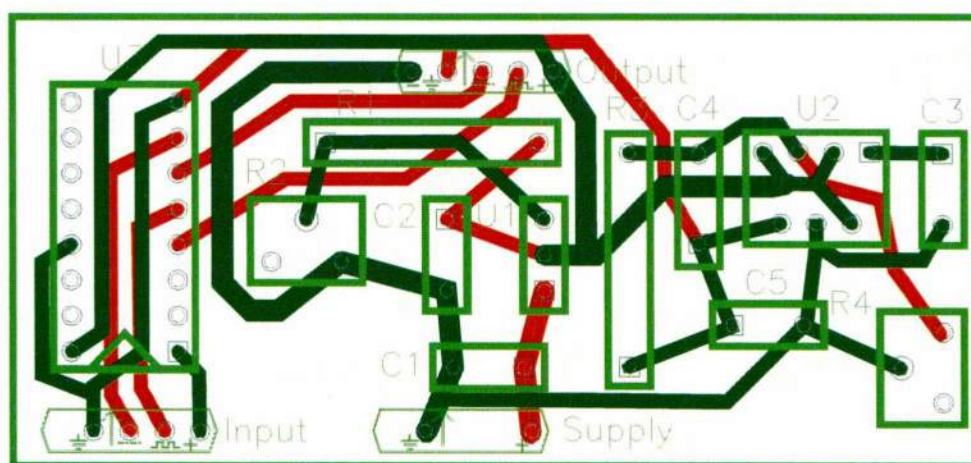
Fig. 3.48: Voltage regulator and level shifter circuit schematic that allows the tuning of the -1v and 4v varactor bias levels via two potentiometers for fine-tuning the resonant frequency of the lens.

Chapter 4

Lens Prototype

After revising the simulation model based on the measurement results of the initial prototype unit cells and adapting the design to satisfy the updated requirements, the second metamaterial prototype was manufactured, assembled, and characterized. This process took place in several stages, with an initial static lens ordered first as a proof of concept of the metamaterial antenna behavior itself prior to building the more expensive reconfigurable lens. The assembly and measurement of the static lens resulted in some small changes to the full lens design, as well as a redesign of the feed antenna.

After testing and evaluation, the prototype lens design was found to have a number of design flaws, primarily in the DC control circuitry, bias voltage regulators, and the geometric layout of the boards. These shortfalls were all resolved in the prototype through one means or another and described below, but full antenna pattern measurements could not be performed due to a problem in the RF design caused by the low self-resonant frequency (SRF) of the inductors that were used throughout the lens.

Even though the antenna could not be fully tested, the experiments centered around the design and testing of this prototype gave significant results for improving future designs. In particular, construction of a full panel of the metamaterial and LED boards revealed many practical issues that would not have been noticed when working only with individual unit cells.

4.1   Feed antenna

The feed antenna is a critical piece of the metamaterial lens antenna. Ideally, the feed geometry should be simple to construct with loose fabrication tolerances, easy to combine with the rest of the lens, and well-matched to a 50 Ohm coaxial transmission line. Planar, printed-circuit-board based antennas are particularly convenient for integration into a metamaterial structure. An electric-mode lens could use a dipole or monopole feed, but there are fewer options for efficient, compact electric metamaterials compared to the magnetic split-ring resonators. The simplest magnetic dipole antenna is the electrically-small loop, but it is an undesirable option due to the low radiation resistance and other detriments. There have been several published designs for electrically-small and efficient magnetic dipole sources, such as the folded slot spherical helix antenna [71] or the spherical split ring (SSR) antenna [72] that greatly improve over the performance of the electrically-small loop. These spherical antennas offer substantial difficulties for fabrication, though. A ground-plane integrated cavity-backed slot antenna offers much simpler construction, unidirectional radiation for the half-cylindrical lens, as well as a good magnetic dipole radiation pattern and reasonable return loss. A magnetic slot would not be feasible for a full cylindrical lens, for which an efficient omnidirectional antenna such as the spherical split-ring would be selected.

The use of a slot antenna (or a dipole/monopole for an electric metamaterial) places an additional constraint on the height of the lens, since the slot or dipole must fit entirely within the lens, and must be separated from the top and bottom ground planes. Shorter slots become necessary for the construction of thinner lenses.

Combining printed-circuit board construction with a coaxial feed allows for several options when selecting the geometry of the radiating slot; three antennas were considered for this design (the competing antenna geometries are shown in Fig. 4.1). The slot could be constructed from a substrate-integrated waveguide (SIW) with microstrip transition [7], but the tapered transition acted as a significant radiating surface in simulations. A closed substrate-integrated cavity with integrated slot and a direct coaxial cable feed eliminates any extraneous radiation and offers good, though very narrowband, performance, but is very sensitive to

the fabrication tolerances of the slot and cavity dimensions and was difficult to excite in practice. A slotted stripline antenna has a good coaxial transition, has no extraneous radiating geometry, and offers broader bandwidth than the full cavity. Each of these three antennas offers similar impedance characteristics when feeding the metamaterial lens, with only small changes in input impedance when placed adjacent to the ZIM structure compared to free space.
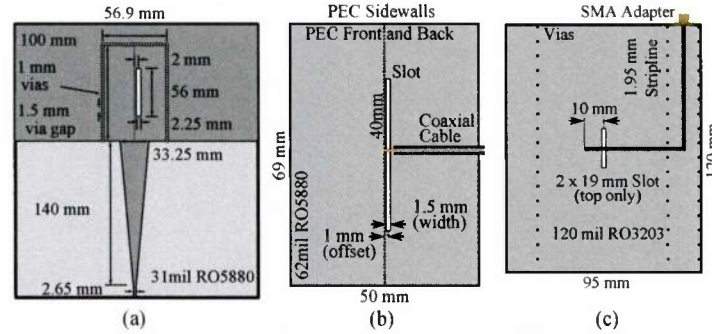
Fig. 4.1: (a) 50 Ω Microstrip-fed substrate-integrated waveguide-backed magnetic slot antenna tuned for 2.4 GHz . (b) Substrate-integrated cavity-backed magnetic slot antenna, with direct 50 Ω coaxial excitation tuned for 2.5 GHz (note-the top, bottom, side, and back of the board are covered in PEC to form a closed cavity, except for the slot aperture). (c) 50 Ω stripline-excited magnetic slot antenna, tuned for 2.8 GHz . The resonant frequencies of the three antennas vary due to changes in the lens structure and targeted frequency throughout the design process.

4.1.1 Substrate-integrated waveguide slot antenna

The design of the SIW antenna may be broken into several pieces: the substrate-integrated waveguide[87], the transition from a microstrip to the waveguide [7], [76], and the slot antenna placement and dimensions [88]. All components were designed for use with a 31mil Rogers RO5880 RF substrate.

A substrate-integrated waveguide is constructed from a section of printed-circuit board with two metalized layers bounded by rows of closely-spaced vias. The cutoff frequency and other characteristics of an SIW are the same as those for a conventional dielectric-filled waveguide. However, the effective size and properties of the SIW will be affected by the diameter and spacing of the vias. Spacing

the vias too far apart or too large will change the effective width of the waveguide for computing the cutoff frequency. For a slot antenna at 2.5 GHz , the TE10 SIW cutoff frequency was selected to be 1.8 GHz according to 3.1 to yield an effective SIW width of $w_e = 56.2$ mm . Selecting a via diameter of $d = 1$ mm and a center-center spacing of $p = 1.5$ mm , the spacing between the via centers according to the SIW design equations 4.1 [76] was $a_s = 56.9$ mm .

$$a_s = w_e + \frac{d^2}{0.95 * p} \tag{4.1}$$

4.1.1.1 Microstrip Transition

The microstrip transition between the 50 Ω microstrip and the very short waveguide was the most troublesome part of the design process. Several papers have documented the design of microstrip transitions [76], [89] based on matching the impedance of a microstrip line and the SIW, from which the width of the transition was determined to be $w_t = 33.25$ mm . At the antenna operating frequency, the SIW was determined to have a wave impedance of 5.6 Ω , from which the final taper width of the microstrip was selected to be 33.25 mm by using the microstrip design tool in Ansoft Designer. The 50 Ω source microstrip had a width of 2.65 mm according to the same design tool. Although nonlinearly-tapered lines (such as Dolph Tchebycheff transformers) can achieve better impedance matches over wider bandwidth [89], a simple linear taper between the thick and thin microstrip lines was used for simplicity. The length of the linear taper between the 50 Ω was determined using Ansoft Designer to simulate the performance for various taper lengths, and evaluating the behavior based on the transmission and reflection in each configuration. Longer tapers achieved better results, with tapers 120mm and greater achieving acceptable results for the antenna transition. The selected length of 140 mm yields less than -14dB reflection over the 2-3 GHz band of interest.

4.1.1.2 Slot Dimensions and Placement

The slot location and size was chosen according to the published design rules for SIW antennas [88] and fine-tuned by parameter study in Ansoft Designer.

The slot length is on the order of $\lambda/2$ and the width of the slot proportional to the desired bandwidth [90], by duality with half-wave dipole antennas. Narrower slots will have reduced bandwidth, but also smaller cross-polarization, as well. The slot location is approximately centered along the length of the waveguide, but slightly to the left of center along the SIW width. The slot must be placed asymmetrically in the SIW in order to produce asymmetrical circulating fields in the metal surrounding the slot for the magnetic field excitation. The length of the shorted waveguide affects the impedance match of the slot, as well, but the length should be minimized to simplify the fabrication. Simulation parameter studies to simultaneously adjust the slot size, slot position, and waveguide length yielded good results for a vertically-centered 2.25x65 mm slot offset by 2mm from center horizontally in a 95 mm waveguide section.

This antenna, simulated on an infinite ground plane, yields a nearly ideal magnetic dipole radiation pattern. Some pattern distortion is expected and demonstrated when evaluated on a finite ground plane. Since the antenna will be radiating into a metamaterial lens, not free space, the far field radiation pattern on a finite ground plane is not critical, however. yields a nearly ideal magnetic dipole radiation pattern. Some pattern distortion is expected and demonstrated when evaluated on a finite ground plane. Since the antenna will be radiating into a metamaterial lens, not free space, the far field radiation pattern on a finite ground plane is not critical, however.

4.1.1.3   Final Tuning and Results

The design equations used to select the initial dimensions and properties of the SIW slot antenna are valid for an antenna radiating into free space. The very low impedance of the near-ZIM lens greatly changes the impedance properties of the antenna. Simulations of the antenna as designed above radiating into a bulk near-ZIM hexagonal lens show a very poor impedance match for the antenna at the design frequency of 2.4 GHz . However, there were resonant dips in the reflection coefficient near 2.1 GHz and 2.6 GHz , which could be shifted by appropriate geometry changes to the structure. Although this antenna was used for initial measurements of the static lens, the design exhibited extraneous radiation from the tapered impedance matching section and proved to be undesirable.

(a) Fabricating the antenna using the PCB mill

(b) Finished Antenna
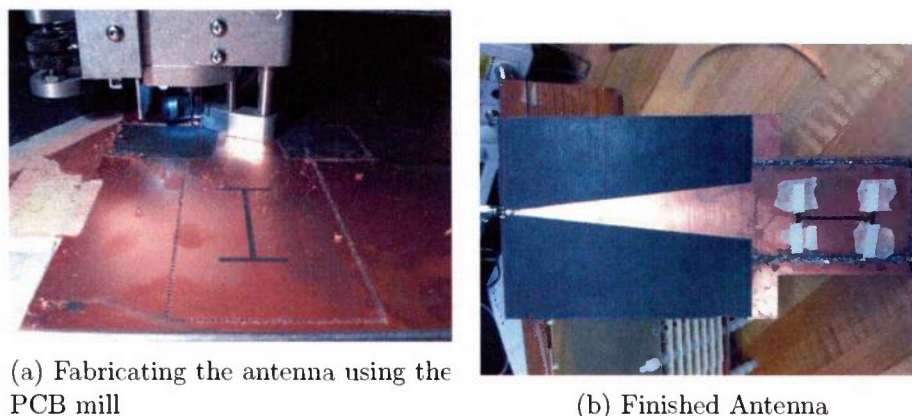
Fig. 4.2: Photographs of the SIW slot antenna.

4.1.2 Substrate-integrated Cavity-backed Slot Antenna

In order to remove the excess radiation from the microstrip taper, the substrate integrated waveguide of the previous design was converted to a closed substrate-integrated cavity. Closing all of the walls greatly restricts the allowed modes, which also significantly restricts the available bandwidth. With a voltage excitation across the slot (implemented by soldering the central conductor of a 50 Ω coaxial cable to one side of the slot, and the sheath to the other) the antenna generated a good though narrowband impedance match.

A copy of the antenna was constructed from Rogers 5880 substrate, but the manufacturing tolerances were not sufficiently good to have the slot resonance frequency aligned with the cavity resonance frequency. In addition, the coaxial feed was very poor, showing significant insertion loss into the antenna. For these reasons, the cavity-based antenna was removed from consideration.

4.1.3 Stripline-integrated Slot Antenna

Since a microstrip-based slot antenna produces bidirectional radiation, a stripline-based design was the next option [91].

A stripline-based circuit by design has its current contained within the two ground planes. By cutting a slot in one ground plane across an open-circuited signal trace, a unidirectional magnetic radiating mode can be achieved. Since the
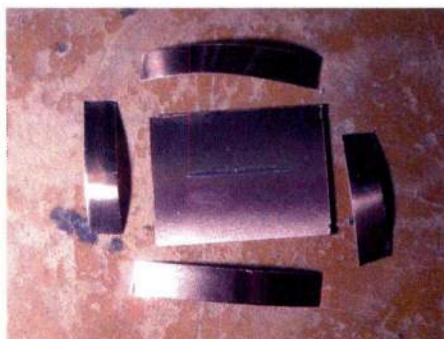
(a) PCB with slot in upper ground plane with pieces of copper tape to form the walls.

(b) Assembled cavity.

(c) Assembled Antenna with coaxial feed.

Fig. 4.3: Photographs of the Substrate-Integrated Cavity slot antenna.

stripline is not a closed metallic box, the bandwidth can be better than the cavity antenna.

Compared to microstrip, a stripline circuit can be slightly more complex. The stripline mode can easily couple to a parallel-plate mode between the top and bottom ground planes unless vias are used to constrain the modes. However, the pattern and spacing of vias also affects the fields generated by the slot; selecting the via placement for an optimal simulated impedance match and good radiation characteristics was the most time-consuming part of the antenna design.

The pattern of the manufactured antenna was measured to find a narrow bandwidth of acceptable magnetic-mode radiation pattern responses. Outside of that narrow band, the cross-pol and sidelobes rapidly increased. More analysis of the antenna is required in order to improve the behavior, although the current design was sufficient for the current experiments. Fig. 4.4 shows the azimuthal field patterns for the antenna.

4.2 Static Metamaterial Lens

Prior to constructing the full metamaterial lens, a static lens was fabricated as a proof of concept for the metamaterial lens itself. Static unit cells for the near-zero-index and near-free-space conditions (shown in Fig. 4.5(a-b)) were tuned and tiled to form a hexagonal lens. The dimensions for the near-free-space unit cell were not sensitive, as the purpose for the resonator was only to be non-resonant at the operational frequency of $\tilde{2}.75$ GHz . Each layer of the lens was constructed from several interlocking pieces, so the angle of the steered beam could be changed by replacing a subset of the metamaterial panels. The metamaterial PCB panels were constructed with mounting holes drilled along the periphery to allow the lens to be assembled with nylon screws and spacers. Photographs of the assembly of the static lens are shown in Fig. 4.6.

Initial measurements of the static lens fed by the substrate-integrated waveguide slot antenna showed encouraging results on the lens performance (as well as indications of the poor behavior of the SIW slot antenna), which prompted the construction of the full metamaterial lens while the static lens testing continued.

Unfortunately, later testing did not improve over the initially promising, but
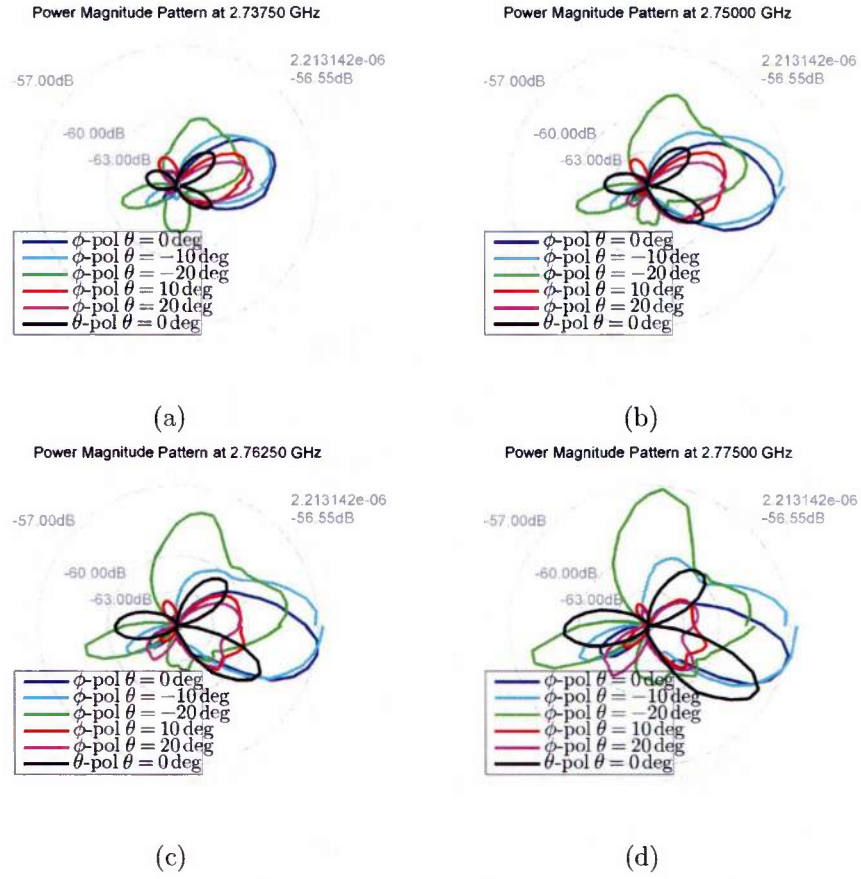
Fig. 4.4: Measured azimuthal pattern cuts for the stripline-integrated slot antenna at (a) 2.7375 GHz (b) 2.75 GHz (c) 2.7625 GHz and (d) 2.775 GHz .
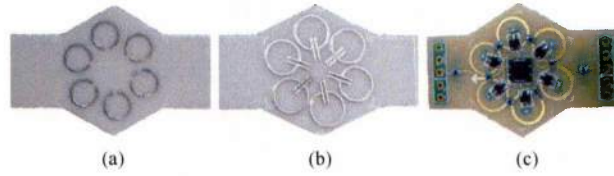
Fig. 4.5: Photograph of individual hex cells for the static near-free-space, static near-ZIM, and reconfigurable metamaterials. The static unit cells were used to construct a test lens, and the near-ZIM hex cells were used to form the inner three rings of the reconfigurable lens.
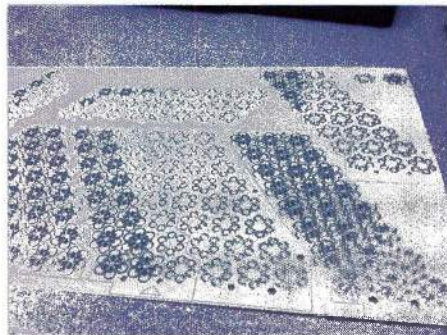
(a) Static metamaterial board
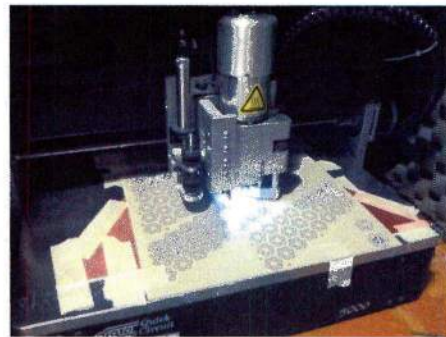
(b) Separating the subelements of the board using the PCB mill

(c) Separated static metamaterial boards
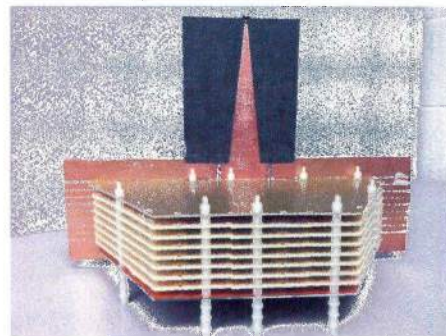
(d) Assembled static lens with substrate integrated waveguide feed, front.

(e) Assembled static lens with substrate integrated waveguide feed, rear.

Fig. 4.6: Photographs of the assembly static metamaterial lens board.

poor-quality measurements. Although the unit cell measurements and simulations agreed very closely and the return loss measurements and simulations of the static lens with the slotted stripline feed also agreed reasonably well, the pattern measurements did not show the expected mainbeam. Simulations using the effective bulk medium properties of the structure predicted a strong mainbeam in the expected direction, depending on the geometric scanning angle. Simulations of the full metamaterial structure were infeasible due to the electrically large but fine-detailed structure of the lens leading to extremely excessive memory requirements (multi-terabyte).

A greatly simplified simulation was performed with only a thin region of the metamaterial unit cells arranged to form a single-beam normally-directed radiation pattern from a slot antenna. When performed with the effective bulk material parameters extracted from the unit cell simulations, it showed a high-directivity normally-directed beam. However, the simulation of the full unit cells did not show a similar radiation pattern. These results indicated that the aggregate of unit cells was not behaving in a way that was consistent with the simulated effective material parameters computed from the results of a single periodic hex cell simulation. Previous work [6], [7], [17] has repeatedly demonstrated the validity of the material parameter extraction routines for predicting the bulk behavior of a periodic near-zero-index metamaterial structure, so additional work is required to determine the reason for this discrepancy.

4.3   Prototype Layout

The reconfigurable metamaterial lens was designed and fabricated from the metamaterial designs discussed in the previous chapter. Although only a half-hexagonal structure was built, the half-circle shown in Fig. 4.7 is the only PCB design necessary for both a half-hexagon and a full-hexagon implementation. The PCB will be cut along the lines of headers, with input signals provided from the edge of the board. To make a circular lens, the leftmost headers and sacrificial unit cells are removed. Then, the two half-circles are rotated and placed back to back to form the full circle, with the headers connected to complete the control loops. Since the same design may be used to fabricate either a half- or a full-cylinder lens, a half-

cylinder is used for the initial prototype to reduce the fabrication cost by reducing the number of required components and PCB boards. The number of layers in the spiral is influenced by both the desired size of the lens, as well as the maximum board size available for manufacturing the PCB layers.

The board layout illustrated in Fig. 4.7 will be combined in a vertical stack with nylon spacers in the same way as the static lens; conceptual illustrations of the final lens structure are shown in Fig. 4.8.
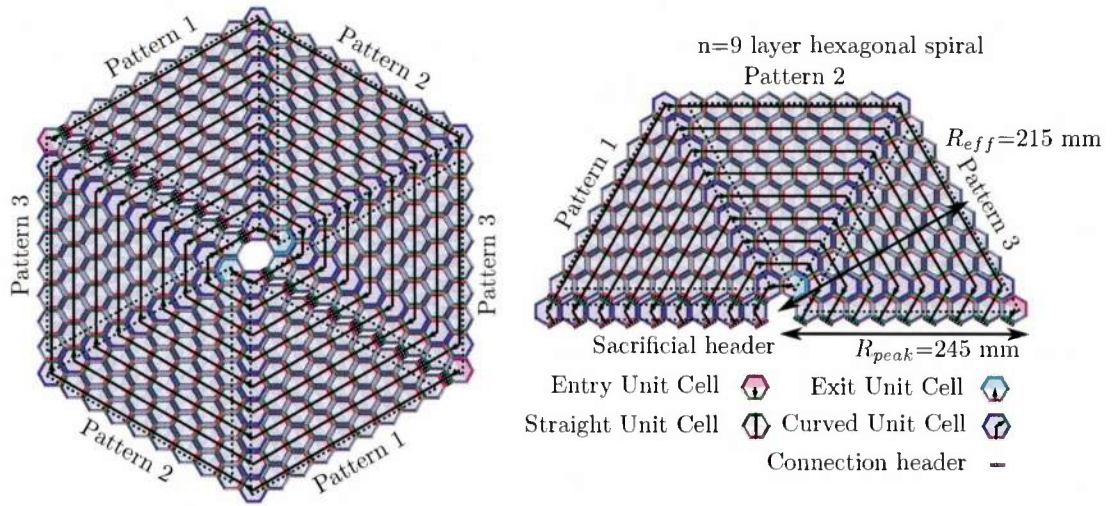
Fig. 4.7: Illustration of a 9-turn hexagonal spiral lens with 270x25 mm unit cells, making a 215 mm radius lens. The lens structure is rotationally symmetric, allowing the design to be fabricated in halves to satisfy PCB board size limitations. The half-lens on the right may be used to construct the half-cylindrical initial prototype, while two halves may be combined to form the entire cylindrical lens.

4.4   Prototype Construction

After receiving the fabricated printed circuit boards in December of 2013, the prototype was assembled. This involved manual assembly of the power regulator board with through-hole components, manual lamination of the top and bottom ground planes with aluminum foil, soldering headers to the circuit boards, and assembling the 5-pin wiring harnesses for distributing power and control signals to the boards.
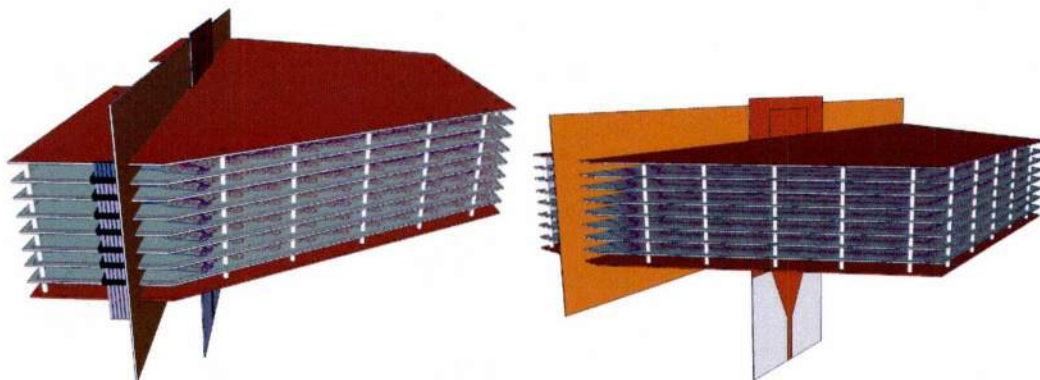
Fig. 4.8: 3D model of prototype lens as half-hexagonal cylinder.

The metamaterial boards are pictured in Fig. 4.9. The boards were received in separated form (unlike the static design), and the headers for the wiring harness added before assembling the lens.

Three finite ground planes are required for the lens - top and bottom for controlling the resonant mode, and a rear ground plane to truncate the half-cylinder and to host the slot antenna. The top and bottom ground planes were ordered from the same company that manufactured the rest of the PCB panels, but arrived without the required copper plating. This was remedied by laminating aluminum foil to the surfaces prior to use (Fig. 4.10).

The rear ground plane is required to have a series of slots and narrow fingers to slide between the metamaterial layers. This does mean that the rear ground plane is not continuous, but has narrow slots for the dielectric substrates. Simulations did not show a major affect of the slotted ground plane compared to a continuous ground plane, due to the parallel orientation of the E-field to the slots. A large number of vias were included to the metamaterial substrates to create an additional effective metal wall between the inside and outside of the lens within the slots, as well. The rear ground plane was manufactured from dual-sided FR4 substrate material using a PCB mill to cut the outline and slots, with photographs shown in Fig. 4.11.
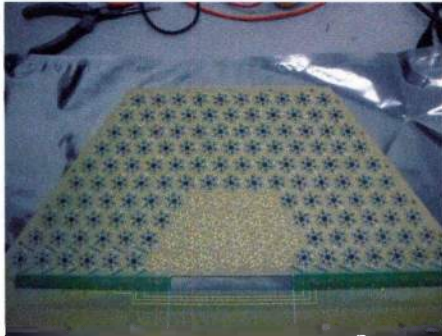
(a) Metamaterial PCB board showing the unit cells with integrated shift registers. Headers for power and control signals were attached manually.
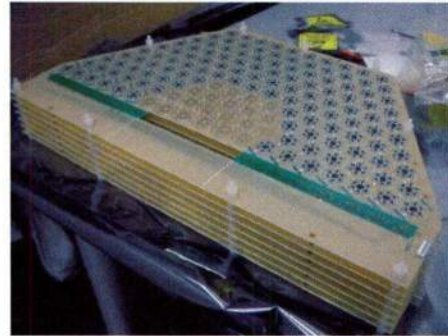
(b) Metamaterial boards stacked vertically, separated by 281 mil nylon spacers.
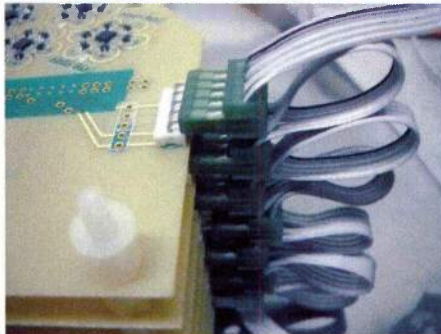
(c) Stack of metamaterial boards connected in parallel by 5-pin wiring harness.

Fig. 4.9: Photographs of the fabricated metamaterial panels and their assembly into a vertical stack.
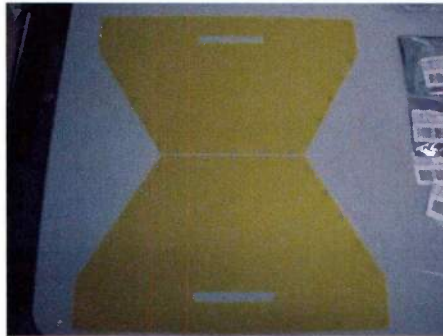
(a) The top and bottom ground panels arrived unplated.

(b) Superglue was used to laminate aluminum foil to the boards to serve as ground planes.

(c) Foil was applied across the entire board and later trimmed to the edge.

(d) One

Fig. 4.10: Photographs of the assembly of the top and bottom ground planes.
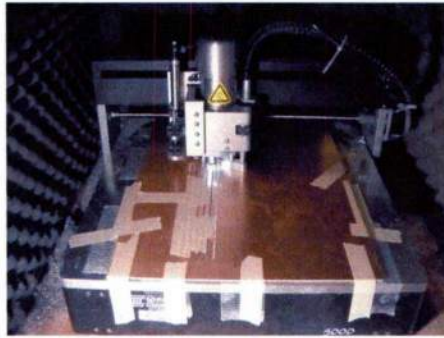
(a) The rear ground plane was machined from double-sided FR4 substrate using a PCB mill.
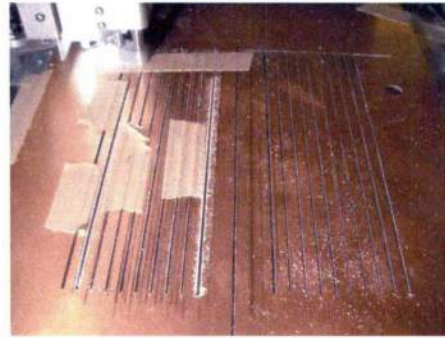
(b) Slots were cut into the substrate to allow installation of the ground between the metamaterial layers.

(c) Two copies of the ground plane are required to cover both halves of the lens; the center of the lens is covered by the slot antenna.

Fig. 4.11: Photographs of the assembly and use of the rear ground plane.

4.4.1 Controller

A MSP430 microcontroller development board (fig:proto:controlphotos) was used as the controller for setting the lens state. The original plan was to use a PC to compute the bit sequence required for a given beam direction, and then transmit that sequence to the lens through the USB-connected MSP430. However, after some revisions, the control logic was capable of being programmed in fixed-point 16-bit arithmetic and included in the MSP430 firmware to allow untethered control of the lens.
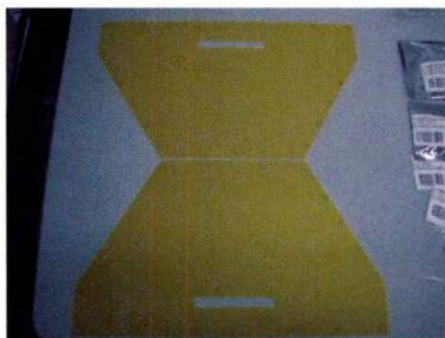
(a) The control wiring harness to the power boards was attached to general-purpose I/O (GPIO) pins on the MSP430.

(b) Although powered by a USB cable, the controller generates all control signals with no communication to a host PC.

Fig. 4.12: Photographs of the MSP430 microcontroller development board used to generate the control signals.

The initial electrical tests focused on the power supply board (Fig. 4.13) and the LED board, which allows for visual feedback of the state of the unit cells within the lens. The original circuit design for the power regulator in Fig. 3.48 turned out to be invalid for the high current required by the LEDs. The single power board was therefore replaced by two boards, one of which was constructed without the -1v bias voltage supply. This change was beneficial, as it allowed the metamaterial (low current, precise voltages) and the LED indicators (high current, imprecise voltages allowed) to be powered independently. Multiple copies of the unpopulated power regulator PCB had been included in the original manufacturing order, and so one of these boards was modified to become the LED power supply.

(a) The power supply PCB was manufactured by a third party, but populated with components manually.
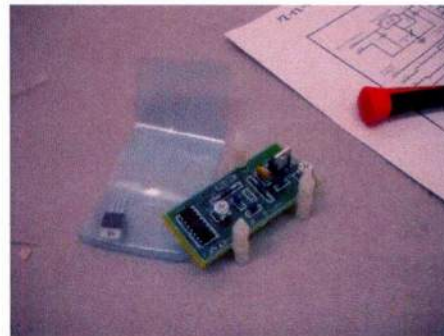
(b) Assembled power board
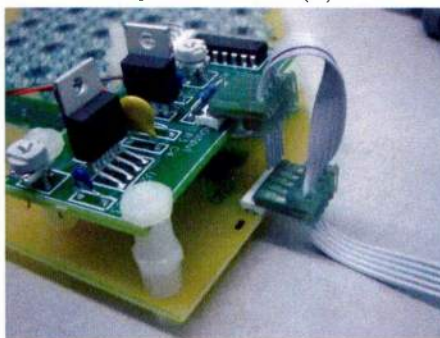
(c) The power board is mounted to the LED board, showing the power supply and control output cable connected to the LED board input.

Fig. 4.13: Photographs of the assembly and use of the power board.

After the power regulator was validated, the LED board was tested (Fig. 4.14). Several bad solder connections to the shift register chips were found and corrected to allow all of the LEDs within the lens to function, and the distributed shift register was tested with a function generator as a clock source, and a momentary pushbutton to control the data signal. With this setup, on-off signals successfully propagated throughout the lens. Clock speeds were increased to 200kHz and greater without obvious clocking errors, given the simple data inputs. At that clock speed, the response of the LEDs throughout the lens to changing the pushbutton state was visually simultaneous and instantaneous.

(a) Assembled LED board.

(b) All LEDs function properly when power is applied.
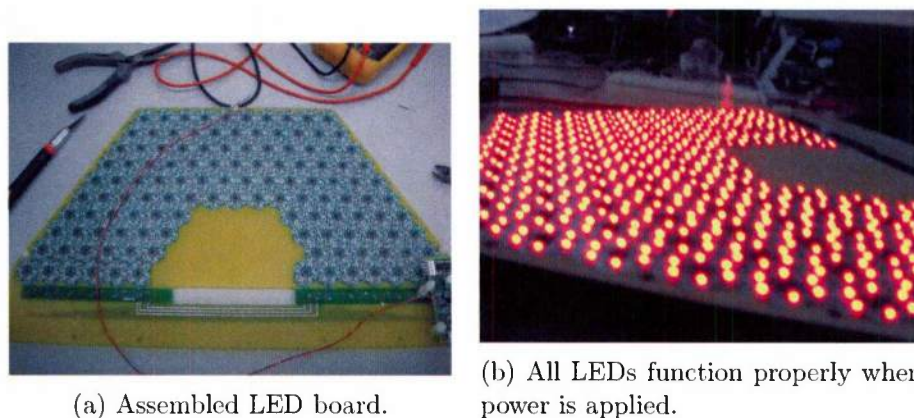
Fig. 4.14: Photographs of the LED board.

However, when sending test patterns with real configuration data through the lens from the MSP430 controller, it was found that the shift registers suffered from severe clock errors due to noise on the clock line, as seen in Fig. 4.15. The errors were most visible when sending individual, isolated bits into the lens, for example, one positive bit in every eight or sixteen bits. The errors were manifested as either dropped bits (a single bit disappearing midway through the lens) or duplicated bits (a single bit mutating to two or more positive bits). These effects were mitigated by inserting additional CMOS buffers into the clock line and adding capacitors at the edge of the lens to reduce the noise (Fig. 4.16). The controller could then successfully set a pattern into the lens for a desired scan angle with a satisfactory accuracy; complete correction of the design flaw would require an additional prototype design so that the buffers and capacitors could be distributed

throughout the lens.

The metamaterial printed circuit boards suffered from similar clock errors, and the same mitigation technique was successfully applied. Each metamaterial PCB was individually tested to ensure that the data signals were propagating throughout the entire lens. In several cases, there were faulty solder joints or inductors that were repaired or replaced to restore correct operation. After verification of the DC response of the lens, the metamaterial boards were stacked vertically and secured by nylon spacers, as shown in Fig. 4.16.

Once the DC control, bias, and power circuitry had been verified, the RF behavior was tested using an individual unit cell and a waveguide test fixture. As seen in Fig. 4.17, there was a strong discrepancy between the measured response of the hex in the unit cell (left) and simulation of the same structure (center). The reason for the difference was determined by destructive testing of the hex cells, which involved sequentially removing components until the results began agreeing with simulations. Based on this process, the shift register and varactors were removed without greatly affecting the response. However, removing the inductors made a significant change. It was determined that the difference between the measurements and simulations was due to the specific inductors selected for the design, which turned out to have a low Self-Resonant Frequency (SRF) of 500 MHz. Simulations performed with the measured two-port scattering parameters of the actual inductors showed the same poor performance as seen in the measurements. The effects of the difference in scattering parameters on the effective material response of the metamaterial are seen in Fig. 4.18; with the original inductor, the ZIM response has been suppressed. Replacing the inductors (Fig. 4.19) in a single hex with higher-quality, high-SRF (2.5 GHz) wire-wound inductors restored the hex behavior to match the simulations after a 200 MHz frequency shift. Fig. 4.20 and Fig. 4.18 show the comparison between the hex response in the waveguide as well as the effective permeability with the original, ideal, and corrected inductors. It was not considered feasible to manually replace the 15,000 0402 SMT inductors on the current prototype, and so the RF testing of the entire lens was postponed until an additional prototype could be designed and built.

(a) A regular input pattern at the upper right is rapidly distorted as it propagates through the array. The input signal was a uniform, regular pattern.

(b) Signal trace of bad clock transition; noise on the clock (yellow) causes a double step of the data (blue) line, erasing a bit.
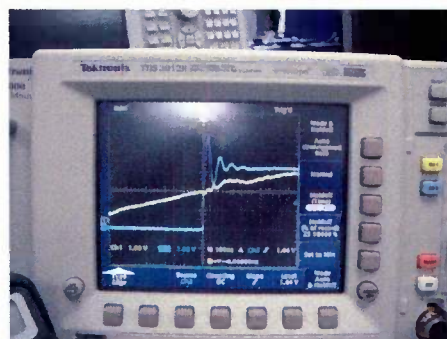
(c) Clock transition with no error. Success and failure was random
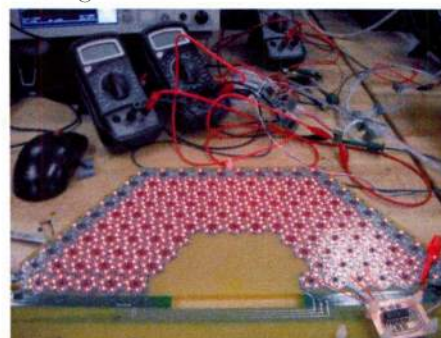
(d) After addition extra capacitance, clock errors were resolved. All single-bit lights in the outer ring are in sync.
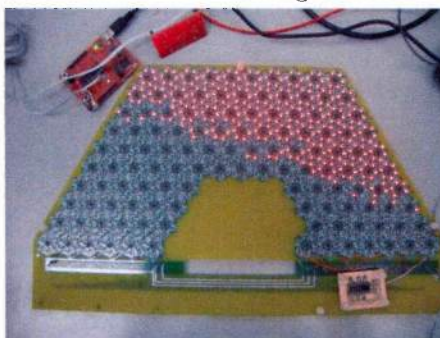
(e) The lens can now be steered with only small errors.

Fig. 4.15: Photographs showing the result of clock noise, and its mitigation.
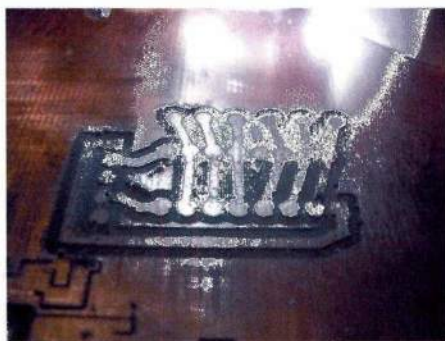
(a) The buffer boards were fabricated using the PCB mill.

(b) One board was created for each layer of the metamaterial lens.

(c) The buffer chips and wires were soldered to the boards.
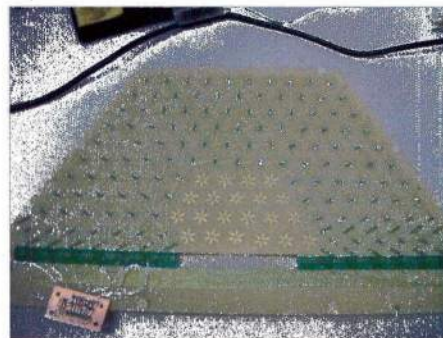
(d) The connection wires (inputs and outputs) were connected to the LED and metamaterial boards after severing the original PCB traces. Additional capacitance between clock and ground was installed, as well.
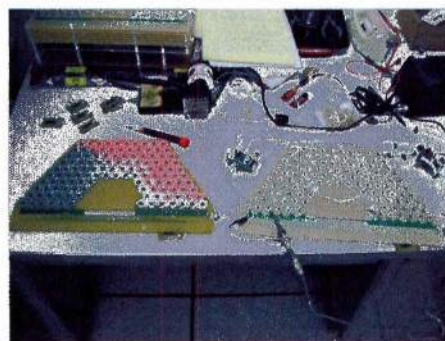
(e) Clock errors in the metamaterial boards were tested by connecting the input of the LED board to the output of the metamaterial board.

(f) The lens was reassembled after connecting and testing each layer.

Fig. 4.16: Photographs showing construction of the buffer carrier boards for mitigating the clock jitter.
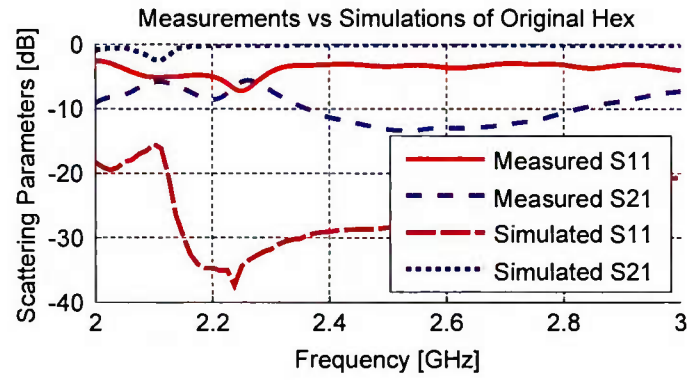
Fig. 4.17: The measured and simulated scattering parameters of the hex show little agreement. In addition to the frequency shift, where the simulations predict a transmission null, the measurements show a transmission peak. This discrepancy was resolved by replacing the inductors of the measured design.

(a) Original low-SRF inductors

(b) Ideal (non-physical) inductors

(c) High-SRF wire-wound inductors
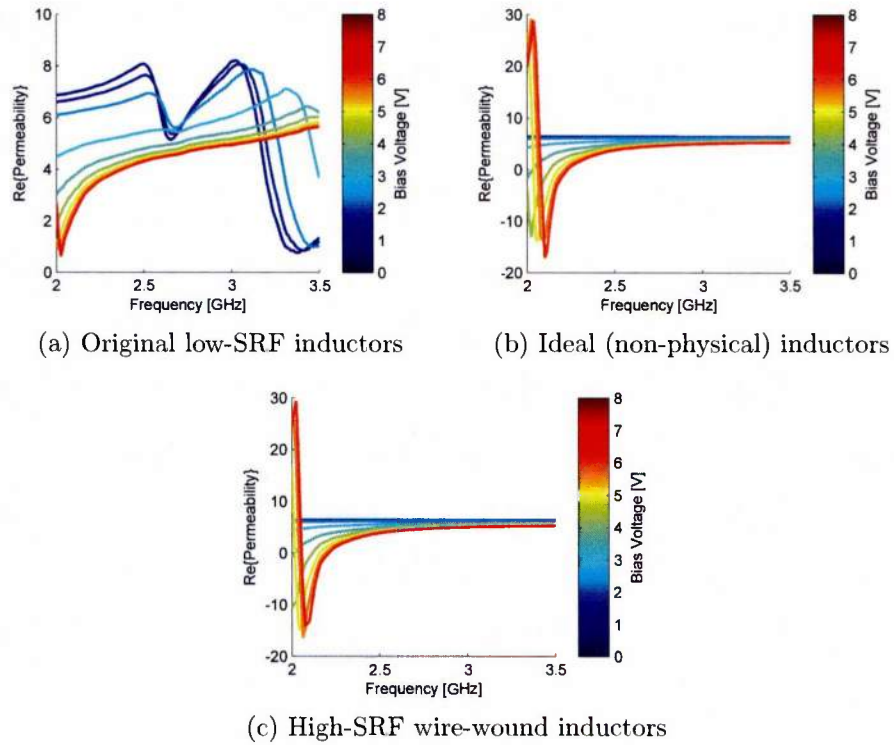
Fig. 4.18: The isolating inductors show a very large effect on the effective metamaterial behavior of the hex cell. Replacing the original, low-SRF inductors by the 68nH high-SRF inductor returns the response to match that of the ideal inductor simulations.
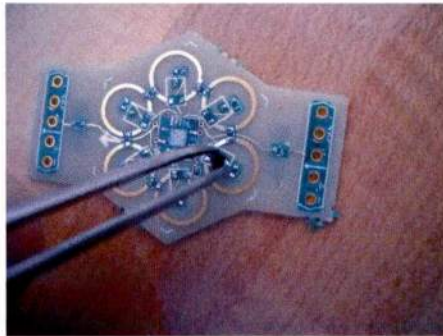
(a) All components were removed from the unit cell in order to determine the cause of the simulation/measurement discrepancy.
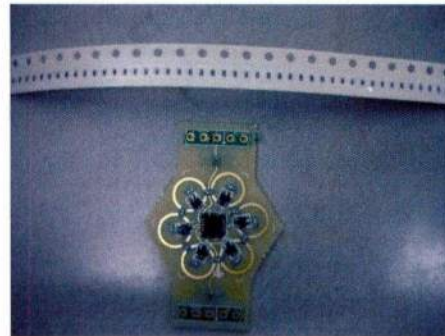
(b) Unit cell prepared for installation of new inductors.
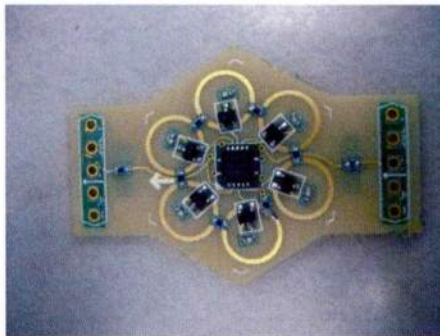
(c) The ceramic inductors have been replaced by wire-wound 68 nH inductors.

Fig. 4.19: Photographs of the single hex cell with corrected inductors.
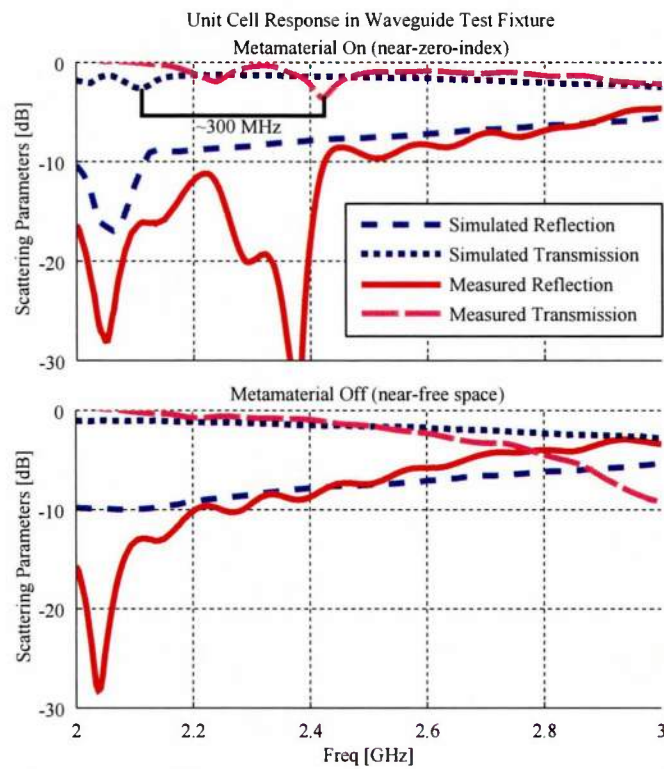
Fig. 4.20: Measured and simulated metamaterial response in the waveguide test cell after replacing the inductors. The measured results show a 300 MHz frequency shift relative to the simulations, as well as increased transmission losses at the upper frequencies (especially for the off state of the metamaterial).

Chapter 5

Conclusions and Future Work

The work described in this dissertation has pushed the boundaries of metamaterial and metamaterial antenna technology. The reconfigurable metamaterial lens antenna offers electronic control over the in-plane radiation pattern, and allows for vertical scanning by extending to a vertical stack of concentric lenses. These designs offer an alternative for high-gain electronic beam scanning when the particular implementation requirements of a many-element phased array are not practical. Like most metamaterial devices, this antenna concept offers additional trade-offs to the designer, but is not suitable as an immediate replacement for all existing scanning antennas. This work will be continued by developing, fabricating, and characterizing a revised prototype of the half-hexagonal antenna as a proof-of-concept for the new technology.

The new hexagonal metamaterial unit cells can be tiled to create an arbitrary-sized metamaterial slab that changes between near-zero-index and near-free space conditions. This work has demonstrated that it is possible to design a spatial control network that may coexist with the resonators of the metamaterial without significant degradation of the behavior. Moreover, tuning of the active frequency and high- and low-index states of the entire metamaterial slab may be adjusted through the external bias voltages. Measurements of the unit cell have confirmed the predicted behavior on an individual unit cell basis, with a slight frequency shift due to imperfect characterization of the varactor diodes and fabrication imperfections. Reconfigurable metamaterials, especially spatially reconfigurable metamaterials, offer many advantages to the electromagnetic designer - the ability to

simultaneously change both effective geometry and effective material parameters will yield a significant increase in advanced device capability as well as broaden the applications space.

Although the metamaterial lens prototype constructed during this project was not successfully tested, the many subcomponents of the design have been tested and verified. The simulations of the lens itself with effective bulk material parameters demonstrate the usefulness of the design approach, and the measurements and simulations of the unit cells show that a spatially tunable metamaterial structure can be achieved.

5.1 Lessons from the Lens Prototype and Future Revisions

Updated designs for a second lens prototype to correct the deficiencies found in the first lens are in progress. The primary correction will be to replace the original inductors by the high-SRF wire-wound inductors. The poor performance caused by the inductor selection in the prototype constructed during this project prevented conclusive testing of the antenna behavior and required a new prototype to finish the tests. In addition to replacing the inductors, the design was revised to address the other issues that were manually corrected in the initial prototype. The primary changes are listed below.

- Verify the computed effective material response of the metamaterial (plotted in Fig. 5.1) and compare the simulated responses of the metamaterial itself to the response of the effective material properties.

- Integrate the separate power supplies for the LED and MTM boards on the LED board.

- Instead of a -1v bias voltage for the LED board, include a +4v high-current supply to act as the power rail for the LED cathodes to enable independent control of the board logic states and the current-consuming LEDs (Fig. 5.2).

- Include quick-disconnect headers for the power supplies and the power supply-metamaterial boards.

- Include toggle switches on the power boards to enable independent control of each voltage rail to reduce power consumption during measurements and simplify testing.

- Include a voltmeter and ammeter on the LED board to allow real-time monitoring in the chamber of the bias and tuning voltages.

- Include both input and output headers for the control signals from the LED and MTM boards, to enable easy monitoring of the control signals.

- Use SMT components for the power boards to simplify assembly and reduce assembly errors.

- Prior to placing the board orders, simulate the metamaterial unit cell with full device characteristics for the inductors, capacitors, and varactors. Ensure that all of the components are rated for high-frequency use.

- Simplify the board layout by transitioning to a bi-directional spiral for the control circuit distribution as seen in Fig. 5.3, which reduces the length and number of traces in back of the board.

- Add Schmitt trigger buffers inside the lens itself to regenerate the clock, at least every 7-8 unit cells. The green borders in Fig. 5.3 illustrate the location of the Schmitt buffers within the interior of the lens.

- Add capacitors between clock and ground and power and ground in each unit cell to minimize noise.

- Update the controller firmware to account for the new control trace layout.

- Remove all of the static hex elements in the center of the lens and replace with the reconfigurable hexes, since the tuning range of the reconfigurable hexes is not large enough to match the static hexes.
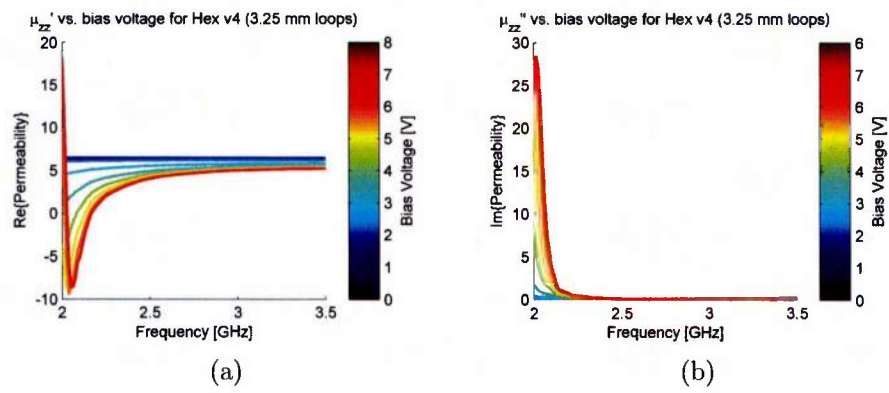
Fig. 5.1: Simulated effective metamaterial parameters for the revised unit cells.
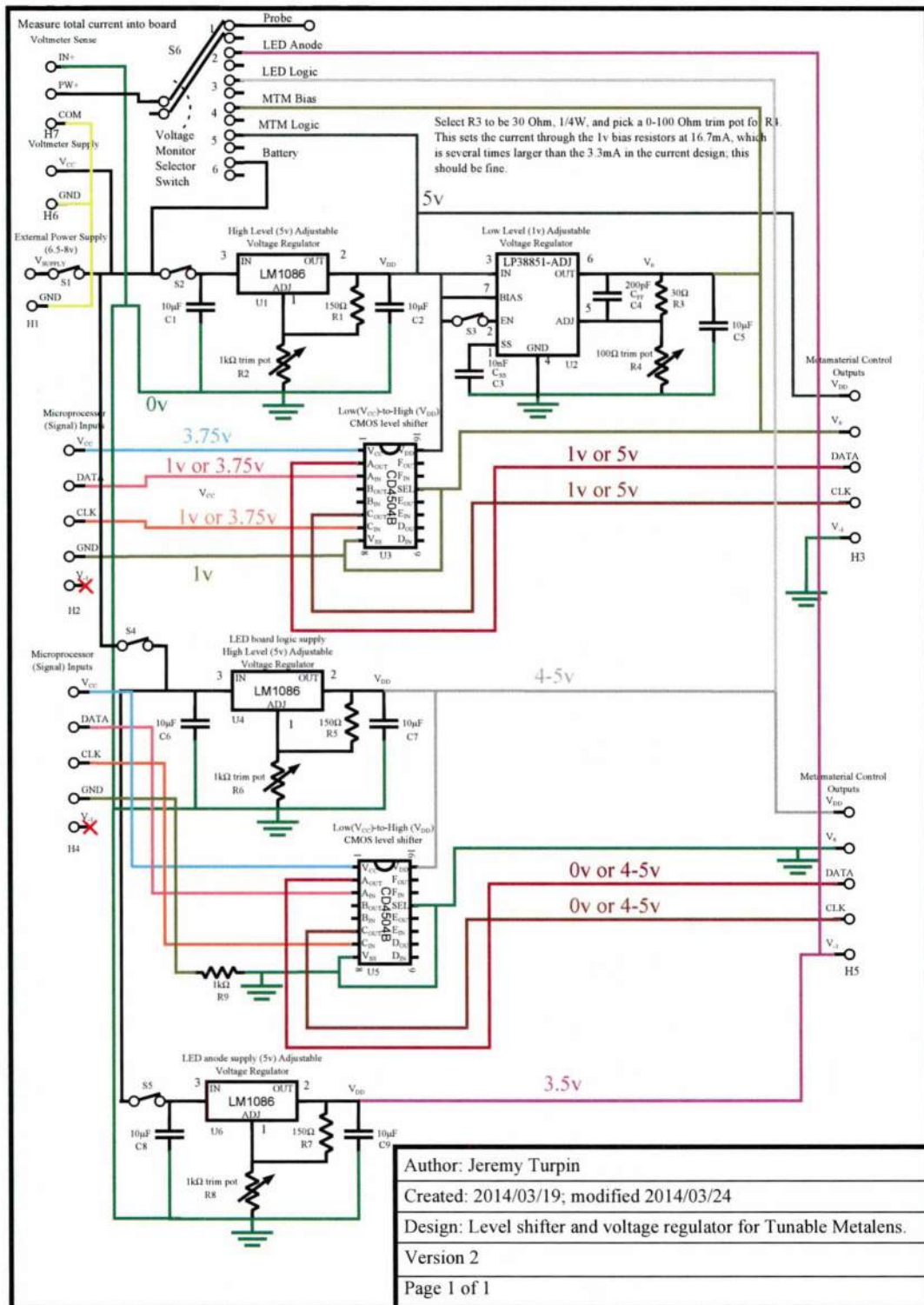
Fig. 5.2: Updated circuit schematic for the voltage regulator and level shifter circuit with integrated power switches for each subcircuit, selectable voltmeter, and ammeter.
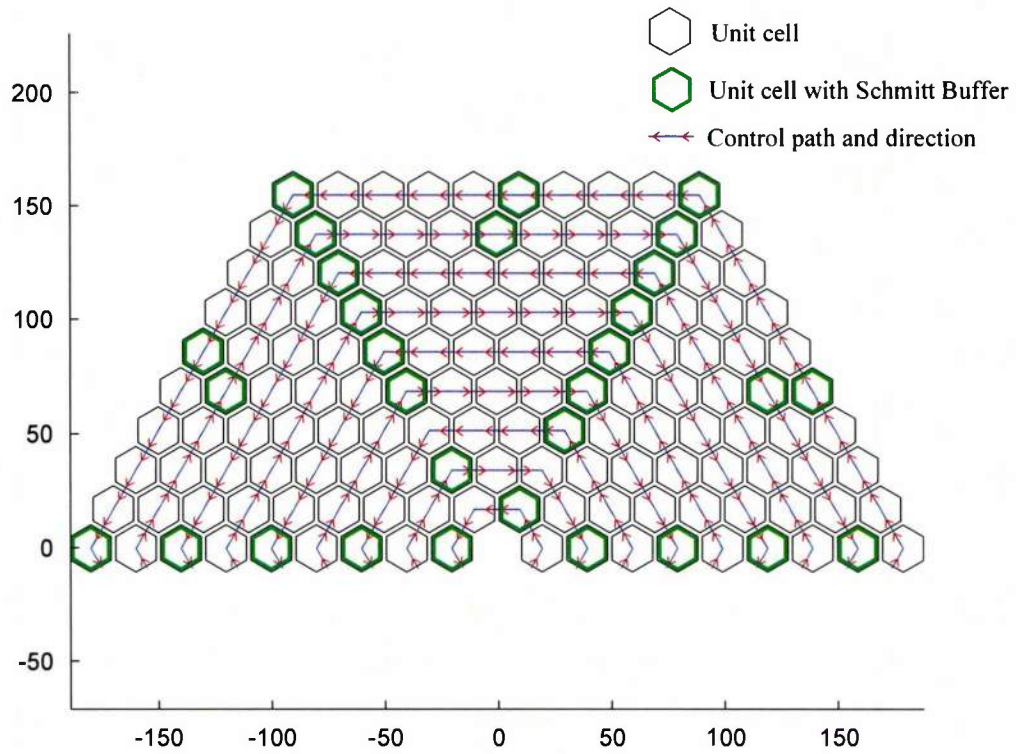
Fig. 5.3: Diagram of the hex orientations for the updated lens design.

References

[1] H. Tao, A. Strikwerda, K. Fan, W. Padilla, X. Zhang, and R. Averitt, "Reconfigurable terahertz mctamaterials," *Physical Review Letters*, vol. 103, no. 14, Oct. 2009.

[2] F. Ellinger, H. Jackel, and W. Bachtold, "Varactor-loaded transmission-line phase shifter at c-band using lumped elements," *IEEE Transactions on Microwave Theory and Techniques*, vol. 51, no. 4, pp. 1135–1140, 2003.

[3] Z. H. Jiang, M. Gregory, and D. H. Werner, "Experimental demonstration of a broadband transformation optics lens for highly directive multibeam emission," *Physical Review B*, vol. 84, pp. 165111/1–6, Oct. 2011.

[4] E. Lier, D. H. Werner, C. P. Scarborough, Q. Wu, and J. A. Bossard, "An octave-bandwidth negligible-loss radiofrequency metamaterial," *Nature Materials*, vol. 10, no. 3, pp. 216–222, 2011.

[5] Z. H. Jiang, M. Gregory, and D. Werner, "A broadband monopole antenna enabled by an ultrathin anisotropic metamaterial coating," *Antennas and Wireless Propagation Letters, IEEE*, vol. 10, pp. 1543–1546, 2011.

[6] Z. H. Jiang, M. D. Gregory, and D. H. Werner, "Broadband high directivity multibeam emission through transformation optics-enabled metamaterial lenses," *IEEE Transactions on Antennas and Propagation*, vol. 60, no. 11, pp. 5063–5074, Nov. 2012.

[7] Z. H. Jiang, Q. Wu, and D. H. Werner, "Demonstration of enhanced broadband unidirectional electromagnetic radiation enabled by a subwavelength profile leaky anisotropic zero-index metamaterial coating," *Physical Review B*, vol. 86, no. 12, pp. 125131/1–7, Sep. 2012.

[8] D. J. Kern and D. H. Werner, "Magnetic loading of EBG AMC ground planes and ultrathin absorbers for improved bandwidth performance and reduced size," *Microwave and Optical Technology Letters*, vol. 48, no. 12, pp. 2468–2471, Dec. 2006.

[9] L. Akhoondzadeh-Asl, D. Kern, P. Hall, and D. Werner, "Wideband dipoles on electromagnetic bandgap ground planes," *Antennas and Propagation, IEEE Transactions on*, vol. 55, no. 9, pp. 2426–2434, Sep. 2007.

[10] Z. Bayraktar, M. D. Gregory, X. Wang, and D. H. Werner, "Matched impedance thin planar composite magneto-dielectric metasurfaces," *IEEE Transactions on Antennas and Propagation*, vol. 60, no. 4, pp. 1910–1920, Apr. 2012.

[11] D.-H. Kwon and D. H. Werner, "Transformation optical designs for wave collimators, flat lenses and right-angle bends," *New Journal of Physics*, vol. 10, no. 11, pp. 115023/1–13, Nov. 2008.

[12] R. Zhou, H. Zhang, and H. Xin, "Metallic wire array as low-effective index of refraction medium for directive antenna application," *IEEE Transactions on Antennas and Propagation*, vol. 58, no. 1, pp. 79–87, 2010.

[13] J. P. Turpin, A. T. Massoud, Z. H. Jiang, P. L. Werner, and D. H. Werner, "Conformal mappings to achieve simple material parameters for transformation optics devices," *Opt. Express*, vol. 18, pp. 244–252, 2010.

[14] J. B. Pendry, D. Schurig, and D. R. Smith, "Controlling electromagnetic fields," *Science*, vol. 312, no. 5781, pp. 1780–1782, Jun. 2006.

[15] D.-H. Kwon and D. H. Werner, "Transformation electromagnetics: an overview of the theory and applications," *IEEE Antennas and Propagation Magazine*, vol. 52, no. 1, pp. 24–46, Feb. 2010.

[16] S. Enoch, G. Tayeb, P. Sabouroux, N. Guérin, and P. Vincent, "A metamaterial for directive emission," *Physical Review Letters*, vol. 89, no. 21, pp. 213902/1–4, Nov. 2002.

[17] J. P. Turpin, Q. Wu, D. H. Werner, B. Martin, M. Bray, and E. Lier, "Low cost and broadband dual-polarization metamaterial lens for directivity enhancement," *IEEE Transactions on Antennas and Propagation*, vol. 60, no. 12, pp. 5717–5726, Dec. 2012.

[18] W. X. Jiang, T. J. Cui, H. F. Ma, X. Y. Zhou, and Q. Cheng, "Cylindrical-to-plane-wave conversion via embedded optical transformation," *Applied Physics Letters*, vol. 92, no. 26, pp. 261903/1–3, 2008.

[19] J. P. Turpin, "Uniaxial metamaterials for microwave far-field collimating lenses," PhD thesis, The Pennsylvania State University, University Park, PA, May 2011.

[20] J. P. Turpin, J. A. Bossard, K. L. Morgan, D. H. Werner, and P. L. Werner, "Reconfigurable and tunable metamaterials: a review of the theory and applications," *International Journal of Antennas and Propagation*, vol. 2014, pp. 1–18, 2014.

[21] O. Reynet and O. Acher, "Voltage controlled metamaterial," *Applied Physics Letters*, vol. 84, no. 7, pp. 1198–1200, 2004.

[22] I. V. Shadrivov, S. K. Morrison, and Y. S. Kivshar, "Tunable split-ring resonators for nonlinear negative-index metamaterials," *Optics Express*, vol. 14, p. 9344, 2006.

[23] M. Lapine, D. Powell, M. Gorkunov, I. Shadrivov, R. Marqués, and Y. Kivshar, "Structural tunability in metamaterials," *Applied Physics Letters*, vol. 95, pp. 084105/1–3, 2009.

[24] F. Costa, A. Monorchio, and G. P. Vastante, "Tunable high-impedance surface with a reduced number of varactors," *IEEE Antennas and Wireless Propagation Letters*, vol. 10, pp. 11–13, 2011.

[25] J. A. Bossard, X. Liang, L. Li, S. Yun, D. H. Werner, B. Weiner, T. S. Mayer, P. F. Cristman, A. Diaz, and I. C. Khoo, "Tunable frequency selective surfaces and negative-zero-positive index metamaterials based on liquid crystals," *IEEE Transactions on Antennas and Propagation*, vol. 56, no. 5, pp. 1308–1320, 2008.

[26] D. Werner, T. Mayer, C. Rivero-Baleine, N. Podraza, K. Richardson, J. Turpin, A. Pogrebnyakov, J. Musgraves, J. Bossard, H. Shin, R. Muise, S. Rogers, and J. Johnson, "Adaptive phase change metamaterials for infrared aperture control," *Proceedings of SPIE*, vol. 8165, no. 1, 81651H/1–9, 2011.

[27] J. Liang and H. Yang, "Microstrip patch antennas on tunable electromagnetic band-gap substrates," *IEEE Transactions on Antennas and Propagation*, vol. 57, no. 6, pp. 1612–1617, Jun. 2009.

[28] F. Costa and A. Monorchio, "Design of subwavelength tunable and steerable fabry-perot/leaky-wave antennas," *Progress In Electromagnetics Research*, vol. 111, pp. 467–481, 2011.

[29] P. Padilla, A. Muñoz-Acevedo, M. Sierra-Castaner, and M. Sierra-Pérez, "Electronically reconfigurable transmitarray at ku band for microwave applications," *IEEE Transactions on Antennas and Propagation*, vol. 58, no. 8, pp. 2571–2579, Aug. 2010.

[30] A. Moessinger, R. Marin, S. Mueller, J. Freese, and R. Jakoby, "Electronically reconfigurable reflectarrays with nematic liquid crystals," *Electronics Letters*, vol. 42, no. 16, pp. 899–900, 2006.

[31] M. Farhat, S. Enoch, S. Guenneau, and A. B. Movchan, "Broadband cylindrical acoustic cloak for linear surface waves in a fluid," *Physical Review Letters*, vol. 101, no. 13, pp. 134501/1–4, 2008.

[32] P. Sheng, J. Mei, Z. Liu, and W. Wen, "Dynamic mass density and acoustic metamaterials," *Physica B: Condensed Matter*, vol. 394, no. 2, pp. 256–261, May 2007.

[33] S. A. Cummer and D. Schurig, "One path to acoustic cloaking," *New Journal of Physics*, vol. 9, no. 3, pp. 45–45, Mar. 2007.

[34] M. G. Andreasen and R. L. Tanner, "Investigation of a square-mesh wire-grid modified-luneburg-lens antenna," Electronics Research Directorate, Air Force Cambridge Research Laboratories, Stanford Research Institute, 2, Sep. 1961.

[35] J. B. Pendry, A. J. Holden, D. J. Robbins, and W. J. Stewart, "Magnetism from conductors and enhanced nonlinear phenomena," *IEEE Transactions on Microwave Theory and Techniques*, vol. 47, no. 11, pp. 2075–2084, 1999.

[36] D. R. Smith, W. J. Padilla, D. C. Vier, S. C. Nemat-Nasser, and S. Schultz, "Composite medium with simultaneously negative permeability and permittivity," *Physical Review Letters*, vol. 84, no. 18, pp. 4184–4187, 2000.

[37] R. Liu, A. Degiron, J. J. Mock, and D. R. Smith, "Negative index material composed of electric and magnetic resonators," *Applied Physics Letters*, vol. 90, no. 26, pp. 263504/1–3, 2007.

[38] D. Schurig, J. J. Mock, and D. R. Smith, "Electric-field-coupled resonators for negative permittivity metamaterials," *Applied Physics Letters*, vol. 88, no. 4, pp. 041109/1–3, 2006.

[39] F. Falcone, T. Lopetegi, M. A. G. Laso, J. D. Baena, J. Bonache, M. Beruete, R. Marques, F. Martin, and M. Sorolla, "Babinet principle applied to the design of metasurfaces and metamaterials," *Physical Review Letters*, vol. 93, no. 19, pp. 197401/1–4, Nov. 1, 2004.

[40] R. Marqués, F. Medina, and R. Rafii-El-Idrissi, "Role of bianisotropy in negative permeability and left-handed metamaterials," *Physical Review B*, vol. 65, no. 14, pp. 144440/1–6, Apr. 2002.

[41] U. Leonhardt, "Optical conformal mapping," *Science*, vol. 312, no. 5781, pp. 1777–1780, 2006.

[42] D. Schurig, J. B. Pendry, and D. R. Smith, "Calculation of material properties and ray tracing in transformation media," *Optics Express*, vol. 14, no. 21, pp. 9794–9804, Oct. 16, 2006.

[43] D. Schurig, J. J. Mock, B. J. Justice, S. A. Cummer, J. B. Pendry, A. F. Starr, and D. R. Smith, "Metamaterial electromagnetic cloak at microwave frequencies," *Science*, vol. 314, no. 5801, pp. 977–980, Nov. 2006.

[44] W. Cai, U. K. Chettiar, A. V. Kildishev, and V. M. Shalaev, "Optical cloaking with metamaterials," *Nature Photonics*, vol. 1, no. 4, pp. 224–227, Apr. 2007.

[45] W. Yan, M. Yan, Z. Ruan, and M. Qiu, "Coordinate transformations make perfect invisibility cloaks with arbitrary shape," *New Journal of Physics*, vol. 10, no. 4, p. 043 040, Apr. 2008.

[46] M. Rahm, D. Schurig, D. A. Roberts, S. A. Cummer, D. R. Smith, and J. B. Pendry, "Design of electromagnetic cloaks and concentrators using form-invariant coordinate transformations of maxwell's equations," *Photonics and Nanostructures-Fundamentals and Applications*, vol. 6, no. 1, pp. 87–95, 2008.

[47] D.-H. Kwon and D. H. Werner, "Polarization splitter and polarization rotator designs based on transformation optics," *Optics Express*, vol. 16, no. 23, pp. 18731/1–8, Oct. 2008.

[48] ——, "Restoration of antenna parameters in scattering environments using electromagnetic cloaking," *Applied Physics Letters*, vol. 92, no. 11, pp. 113507/1–3, 2008.

[49] D. H. Kwon and D. H. Werner, "Flat focusing lens designs having minimized reflection based on coordinate transformation techniques," *Optics Express*, vol. 17, no. 10, pp. 7807–7817, 2009.

[50] S. Cummer, B.-I. Popa, D. Schurig, D. Smith, and J. Pendry, "Full-wave simulations of electromagnetic cloaking structures," *Physical Review E*, vol. 74, no. 3, pp. 036621/1–5, Sep. 2006.

[51] J. Li and J. Pendry, "Hiding under the carpet: a new strategy for cloaking," *Physical Review Letters*, vol. 101, no. 20, Nov. 2008.

[52] D. A. Roberts, N. Kundtz, and D. R. Smith, "Optical lens compression via transformation optics," *Optics Express*, vol. 17, no. 19, pp. 16 535–16 542, 2009.

[53] N. I. Landy and W. J. Padilla, "Guiding light with conformal transformations," *Optics Express*, vol. 17, no. 17, pp. 14 872–14 879, 2009.

[54] Q. Wu, J. P. Turpin, and D. H. Werner, "Integrated photonic systems based on transformation optics enabled gradient index devices," *Light Sci Appl*, vol. 1, e38, Nov. 23, 2012.

[55] Z. Bayraktar, M. Gregory, X. Wang, and D. Werner, "A versatile design strategy for thin composite planar double-sided high-impedance surfaces," *IEEE Transactions on Antennas and Propagation*, vol. 60, no. 6, pp. 2770–2780, Jun. 2012.

[56] D. Sievenpiper, L. Zhang, R. Broas, N. Alexopolous, and E. Yablonovitch, "High-impedance electromagnetic surfaces with a forbidden frequency band," *Microwave Theory and Techniques, IEEE Transactions on*, vol. 47, no. 11, pp. 2059–2074, 1999.

[57] F. Kong, B.-I. Wu, J. A. Kong, J. Huangfu, S. Xi, and H. Chen, "Planar focusing antenna design by using coordinate transformation technology," *Applied Physics Letters*, vol. 91, no. 25, p. 253 509, 2007.

[58] J. Zhang, Y. Luo, S. Xi, H. Chen, L. Ran, B. I. Wu, and J. A. Kong, "Directive emission obtained by coordinate transformation," *Progress In Electromagnetics Research*, vol. 81, pp. 437–446, 2008.

[59] P. H. Tichit, S. N. Burokur, and A. de Lustrac, "Ultradirective antenna via transformation optics," *Journal of Applied Physics*, vol. 105, no. 10, pp. 104912/1–3, 2009.

[60] P. Ikonen, C. Simovski, and S. Tretyakov, "Compact directive antennas with a wire-medium artificial lens," *Microwave and Optical Technology Letters*, vol. 43, no. 6, pp. 467–469, Dec. 2004.

[61] T. Driscoll, D. N. Basov, A. F. Starr, P. M. Rye, S. Nemat-Nasser, D. Schurig, and D. R. Smith, "Free-space microwave focusing by a negative-index gradient lens," *Applied Physics Letters*, vol. 88, no. 8, p. 081 101, 2006.

[62] R. Chantalat, C. Menudier, M. Thevenot, T. Monediere, E. Arnaud, and P. Dumon, "Enhanced EBG resonator antenna as feed of a reflector antenna in the ka band," *IEEE Antennas and Wireless Propagation Letters*, vol. 7, pp. 349–353, 2008.

[63] H. F. Ma, X. Chen, H. S. Xu, X. M. Yang, W. X. Jiang, and T. J. Cui, "Experiments on high-performance beam-scanning antennas made of gradient-index metamaterials," *Applied Physics Letters*, vol. 95, no. 9, p. 094 107, 2009.

[64] W. X. Jiang, T. J. Cui, H. F. Ma, X. M. Yang, and Q. Cheng, "Layered high-gain lens antennas via discrete optical transformation," *Applied Physics Letters*, vol. 93, no. 22, p. 221 906, 2008.

[65] D.-H. Kwon and D. H. Werner, "Beam scanning using flat transformation electromagnetic focusing lenses," *IEEE Antennas and Wireless Propagation Letters*, vol. 8, pp. 1115–1118, 2009.

[66] J. P. Turpin, Q. Wu, D. H. Werner, B. Martin, M. Bray, and E. Lier, "Near-zero-index metamaterial lens combined with AMC metasurface for high-directivity low-profile antennas," *IEEE Transactions on Antennas and Propagation*, vol. 62, no. 4, pp. 1928–1936, Apr. 2014.

[67] Q. Cheng, W. Xiang Jiang, and T. Jun Cui, "Multi-beam generations at pre-designed directions based on anisotropic zero-index metamaterials," *Applied Physics Letters*, vol. 99, no. 13, pp. 131913/1–3, 2011.

[68] J. Turpin, Q. Wu, D. Werner, E. Lier, B. Martin, and M. Bray, "A compact directive antenna combining metamaterial collimating lens and artificial magnetic ground plane," in *Proc. 2012 IEEE Ant. Propag. Int. Symp.*, Chicago, IL, USA, Jul. 8, 2012.

[69] J. P. Turpin, Z. H. Jiang, P. L. Werner, and D. H. Werner, "Tunable metamaterials for conformally mapped transformation optics lenses," in *Proc. 2010 IEEE Ant. Propag. Int. Symp.*, Toronto, Ontario, Canada, Jul. 13, 2010.

[70] J. P. Turpin and D. H. Werner, "Switchable near-zero-index magnetic meta-material for dynamic beam-scanning lens," in *Proc. 2012 IEEE Ant. Propag. Int. Symp.*, Chicago, IL: IEEE, 2012, pp. 1–2.

[71] S. Best, "A low q electrically small magnetic (TE mode) dipole," *IEEE Antennas and Wireless Propagation Letters*, vol. 8, pp. 572–575, 2009.

[72] O. S. Kim, "Low-q electrically small spherical magnetic dipole antennas," *IEEE Transactions on Antennas and Propagation*, vol. 58, no. 7, pp. 2210–2217, Jul. 2010.

[73] A. Ittipiboon, R. Mongia, Y. Antar, P. Bhartia, and M. Cuhaci, "Aperture fed rectangular and triangular dielectric resonators for use as magnetic dipole antennas," *Electronics Letters*, vol. 29, no. 23, pp. 2001–2002, 1993.

[74] P. Kandasamy and N. Okamoto, "Resonant modes of a concentric spherical cavity with conically stratified medium," *IEEE Transactions on Microwave Theory and Techniques*, vol. 49, no. 1, pp. 111–118, 2001.

[75] C. Ho, P. Shumaker, L. Fan, K. Smith, and J. Liao, "Printed cylindrical slot antenna for GPS commercial applications," *Electronics Letters*, vol. 32, no. 3, p. 151, 1996.

[76] D. Deslandes, "Design equations for tapered microstrip-to-substrate integrated waveguide transitions," *2010 IEEE MTT-S International Microwave Symposium Digest (MTT)*, pp. 704–707, 2010.

[77] Z. Szczepaniak and B. Galwas, "Oscillator with photovaractor for optically-controlled phased-array antenna beam steering," in *Proc. 14th Int. Conf. on Microw., Radar, and Wireless Comm.*, vol. 3, Telecommun. Res. Inst, 2002, pp. 882–885.

[78] K. Aydin and E. Ozbay, "Capacitor-loaded split ring resonators as tunable metamaterial components," *Journal of Applied Physics*, vol. 101, no. 2, pp. 024911/1–7, 2007.

[79] L. Boccia, I. Russo, G. Amendola, and G. Di Massa, "Preliminary results on tunable frequency selective surface for beam steering transmit-array applications," *Proceedings of the 5th European Conference on Antennas and Propagation (EUCAP)*, pp. 1002–1005, 2011.

[80] Z. H. Jiang, C. Scarborough, D. H. Werner, P. L. Werner, C. Rivero-Baleine, and C. Drake, "An isotropic 8.5 MHz magneti meta-lens," in *Proc. 2011 IEEE Ant. Propag. Int. Symp.*, IEEE, Jul. 2011, pp. 1151–1154.

[81] E. Daniel, N. Harff, V. Sokolov, S. Schreiber, and B. Gilbert, "Network analyzer measurement de-embedding utilizing a distributed transmission matrix bisection of a single THRU structure," in *ARFTG Conference Digest Spring, 2004. 63rd*, IEEE, Jun. 11, 2004, pp. 61–68.

[82] R. Bauer and P. Penfield, "De-embedding and unterminating," *Microwave Theory and Techniques, IEEE Transactions on*, vol. 22, no. 3, pp. 282–288, Mar. 1974.

[83] H.-J. Eul and B. Schiek, "Thru-match-reflect: one result of a rigorous theory for de-embedding and network analyzer calibration," in *Proceedings of the 18th European Microwave Conference*, IEEE, Oct. 1988, pp. 909–914.

[84] Agilent, *De-embedding and embedding s-parameter networks using a vector network analyzer: appl. note 1364-1*.

[85] J. Laskar, S. Chakraborty, M. Tentzeris, F. Bien, and A.-V. Pham, "Appendix: a compendium of the TRL calibration algorithm," in *Advanced Integrated Communication Microsystems*, Hoboken, NJ, USA: John Wiley & Sons, Inc., Feb. 20, 2009.

[86] J. Bornemann, "De-embedding techniques."

[87] G. Q. Luo, Z. F. Hu, L. X. Dong, and L. L. Sun, "Planar slot antenna backed by substrate integrated waveguide wavity," *IEEE Antennas and Wireless Propagation Letters*, vol. 7, pp. 236–239, 2008.

[88] D. Stephens, P. Young, and I. Robertson, "W-band substrate integrated waveguide slot antenna," *Electronics Letters*, vol. 41, no. 4, pp. 165–167, Feb. 2005.

[89] K. Lu, "An efficient method for analysis of arbitrary nonuniform transmission lines," *IEEE Transactions on Microwave Theory and Techniques*, vol. 45, no. 1, pp. 9–14, 1997.

[90] C. A. Balanis, *Antenna theory, Analysis and Design*, 3rd ed. Wiley New York, 2005, 1117 pp.

[91] C. Locker, T. Vaupel, and T. Eibert, "Radiation efficient unidirectional low-profile slot antenna elements for x-band application," *IEEE Transactions on Antennas and Propagation*, vol. 53, no. 8, pp. 2765–2768, Aug. 2005.

Publications

Journal Articles

[1] X. Wang, D. H. Werner, and J. P. Turpin, "A fast analysis of scattering from large-scale finite periodic microstrip patch arrays arranged on a non-orthogonal lattice using sub-entire domain basis functions," *IEEE Transactions on Antennas and Propagation*, vol. 62, no. 5, pp. 2543–2552, May 2014.

[2] J. P. Turpin, P. E. Sieber, and D. H. Werner, "Absorbing ground planes for reducing planar antenna radar cross-section based on frequency selective surfaces," *IEEE Antennas and Wireless Propagation Letters*, vol. 12, no. 1, pp. 1456–1459, Dec. 2013.

[3] D. Werner, T. Mayer, C. Rivero-Baleine, N. Podraza, K. Richardson, J. Turpin, A. Pogrebnyakov, J. Musgraves, J. Bossard, H. Shin, R. Muise, S. Rogers, and J. Johnson, "Adaptive phase change metamaterials for infrared aperture control," *Proceedings of SPIE*, vol. 8165, no. 1, 81651H/1–9, 2011.

[4] Xiande Wang, Douglas H. Werner, and Jeremiah P. Turpin, "Application of AIM and MBPE techniques to accelerate modeling of 3-d doubly periodic structures with non-orthogonal lattices composed of bianisotropic media," *IEEE Transactions on Antennas and Propagation*, vol. 62, no. 8, pp. 4067–4080, Aug. 2014.

[5] X. Wang, Q. Wu, J. P. Turpin, and D. H. Werner, "Body-of-revolution finite-difference time-domain for rigorous analysis of three-dimensional axisymmet-

ric transformation optics lenses," *Optics Letters*, vol. 38, no. 1, pp. 67–69, Dec. 20, 2012.

[6] J. P. Turpin, A. T. Massoud, Z. H. Jiang, P. L. Werner, and D. H. Werner, "Conformal mappings to achieve simple material parameters for transformation optics devices," *Opt. Express*, vol. 18, pp. 244–252, 2010.

[7] J. P. Turpin, D. H. Werner, and D. E. Wolfe, "Design considerations for microwave-frequency spatially-reconfigurable metamaterials," *IEEE Transactions on Antennas and Propagation (submitted)*, 2015.

[8] G. Oliveri, E. T. Bekele, D. H. Werner, J. P. Turpin, and A. Massa, "Generalized QCTO for metamaterial-lens-coated conformal arrays," *IEEE Transactions on Antennas and Propagation*, vol. 62, no. 8, pp. 4089–4095, Aug. 2014.

[9] Q. Wu, J. P. Turpin, and D. H. Werner, "Integrated photonic systems based on transformation optics enabled gradient index devices," *Light Sci Appl*, vol. 1, e38, Nov. 23, 2012.

[10] X. Wang, J. Turpin, and D. H. Werner, "Investigation of scattering properties of large-scale aperiodic tilings using a combination of the characteristic basis function and adaptive integral methods," *IEEE Transactions on Antennas and Propagation*, vol. 61, no. 6, pp. 3149–3160, Jun. 2013.

[11] J. P. Turpin, Q. Wu, D. H. Werner, B. Martin, M. Bray, and E. Lier, "Low cost and broadband dual-polarization metamaterial lens for directivity enhancement," *IEEE Transactions on Antennas and Propagation*, vol. 60, no. 12, pp. 5717–5726, Dec. 2012.

[12] Z. Bayraktar, J. P. Turpin, and D. H. Werner, "Nature-inspired optimization of high-impedance metasurfaces with ultrasmall interwoven unit cells," *Antennas and Wireless Propagation Letters, IEEE*, vol. 10, pp. 1563–1566, 2011.

[13] J. P. Turpin, Q. Wu, D. H. Werner, B. Martin, M. Bray, and E. Lier, "Near-zero-index metamaterial lens combined with AMC metasurface for high-directivity low-profile antennas," *IEEE Transactions on Antennas and Propagation*, vol. 62, no. 4, pp. 1928–1936, Apr. 2014.

[14] J. P. Turpin, J. A. Bossard, K. L. Morgan, D. H. Werner, and P. L. Werner, "Reconfigurable and tunable metamaterials: a review of the theory and applications," *International Journal of Antennas and Propagation*, vol. 2014, pp. 1–18, 2014.

[15] J. P. Turpin and D. H. Werner, "Reconfigurable beam-scanning near-zero-index metamaterial lens," *Journal of Applied Physics (submitted)*, 2015.

[16] X. Wang, Q. Wu, J. P. Turpin, and D. H. Werner, "Rigorous analysis of axisymmetric transformation optics lenses embedded in layered media illuminated by obliquely incident plane waves," *Radio Science*, vol. 48, pp. 232–247, 2013.

[17] S. H. Martin, I. Martinez, J. P. Turpin, D. H. Werner, E. Lier, and M. G. Bray, "The synthesis of wide- and multi-bandgap electromagnetic surfaces with finite size and nonuniform capacitive loading," *IEEE Transactions on Microwave Theory and Techniques*, pp. 1–11, 2014.

[18] Q. Wu, Z. H. Jiang, O. Quevedo-Teruel, J. P. Turpin, W. Tang, Y. Hao, and D. H. Werner, "Transformation optics inspired multibeam lens antennas for broadband directive radiation," *IEEE Transactions on Antennas and Propagation*, vol. 61, no. 12, pp. 5910–5922, Dec. 2013.

Conference Proceedings

[19] J. Turpin, Q. Wu, D. Werner, E. Lier, B. Martin, and M. Bray, "A compact directive antenna combining metamaterial collimating lens and artificial magnetic ground plane," in *Proc. 2012 IEEE Ant. Propag. Int. Symp.*, Chicago, IL, USA, Jul. 8, 2012.

[20] J. Turpin, P. Sieber, and D. Werner, "Absorbing FSS ground plane for reduced-radar cross section of conformal antennas," in *Proc. 2013 IEEE Ant. Propag. Int. Symp.*, Orlando, FL, USA, Jul. 8, 2013.

[21] Jeremiah. P. Turpin and Douglas. H. Werner, "Active transmitarray antenna based on near-zero-index metalens," in *Proc. 2014 IEEE Ant. Propag. Int. Symp.*, Memphis, TN, USA, Jul. 6, 2014.

[22] J. P. Turpin, Q. Wu, D. H. Werner, E. Lier, B. Martin, and M. Bray, "Anisotropic metamaterial realization of a flat gain-enhancing lens for antenna applications," in *Proc. 2011 IEEE Ant. Propag. Int. Symp.*, Spokane, WA: IEEE, Jul. 2011, pp. 2886–2889.

[23] J. P. Turpin and D. H. Werner, "Beam scanning antenna enabled by a spatially reconfigurable near-zero index metamaterial," in *Proc. 7th European Conf. Antennas Propag. (EuCAP)*, 2013.

[24] D. Werner, Z. H. Jiang, C. P. Scarborough, Q. Wu, M. D. Gregory, and J. P. Turpin, "Broadband low-loss metamaterial-enabled devices," in *Proc. SAMPE 2012*, Baltimore, MD, USA, May 21, 2012.

[25] Jeremiah. P. Turpin and Douglas. H. Werner, "Construction and measurements of a prototype near-zero-index reconfigurable metamaterial antenna," in *Proc. 2014 IEEE Ant. Propag. Int. Symp.*, Memphis, TN, USA, Jul. 6, 2014.

[26] J. P. Turpin and D. H. Werner, "Cylindrical metamaterial lens for single-feed adaptive beamforming," in *Proc. 2012 IEEE Ant. Propag. Int. Symp.*, Chicago, IL: IEEE, 2012, pp. 1–2.

[27] E. Lier, M. Bray, B. Martin, J. Turpin, Q. Wu, and D. Werner, "Demonstration of high gain low profile antenna based on low-index metalens and artificial magnetic ground plane," in *Proc. 2012 IEEE Ant. Propag. Int. Symp.*, Chicago, IL, USA, Jul. 8, 2012.

[28] ——, "Demonstration of low-index meta-lens for high gain low profile antennas," in *Proc. 2011 IEEE Ant. Propag. Int. Symp.*, Spokane, WA, USA, Jul. 4, 2011.

[29] J. P. Turpin, Z. H. Jiang, P. L. Werner, D. H. Werner, and D.-H. Kwon, "Embedded transformation optics lenses for antenna performance enhancement," in *Proc. ACES 2011*, Williamsburg, VA, Mar. 2011.

[30] Q. Wu, J. P. Turpin, D. H. Werner, P. L. Werner, W. Tang, and Y. Hao, "Flat collimating lenses based on quasi-conformal transformation electromagnetics," in *Proc. 6th European Conf. Antennas Propag. (EuCAP)*, Prague, Czech Republic: IEEE, Mar. 26, 2012, pp. 1696–1700.

[31] Q. Wu, J. P. Turpin, X. Wang, D. H. Werner, A. Pogrebnyakov, A. Swisher, and T. S. Mayer, "Flat transformation optics graded-index (TO-GRIN) lenses," in *Proc. 6th European Conf. Antennas Propag. (EuCAP)*, Prague, Czech Republic: IEEE, Mar. 26, 2012, pp. 1701–1705.

[32] Donovan Brocker, Jeremiah P. Turpin, and Douglas H. Werner, "Gradient index lens optimization using transformation optics," in *Proc. 2014 IEEE Ant. Propag. Int. Symp.*, Memphis, TN, USA, Jul. 6, 2014.

[33] D. H. Werner, J. P. Turpin, D. Brocker, X. Wang, Z. H. Jiang, and P. L. Werner, "Gradient-index lens design with quasi-conformal transformation optics for energy concentration," in *Proc. SPIE 8834*, R. Winston and J. Gordon, Eds., Sep. 18, 2013, 88340F.

[34] Douglas H. Werner, Jeremiah P. Turpin, Donovan Brocker, Z. H. Jiang, and Pingjuan L. Werner, "Increasing device and design practicality in transformation optics," in *Proc. 2014 Spring Meeting of the Materials Research Society *KK6.08*, San Francisco, CA, USA, Apr. 21, 2014.

[35] Giacomo Oliveri, E. Bekele, L. Tenuti, Jeremiah. P. Turpin, Douglas H. Werner, Pingjuan L. Werner, and A. Massa, "Metamaterial enhanced arrays by innovative QCTO approaches," in *Proc. 2014 IEEE Ant. Propag. Int. Symp.*, Memphis, TN, USA, Jul. 6, 2014.

[36] Giacomo Oliveri, E. Bekele, Jeremiah. P. Turpin, Douglas H. Werner, and A. Massa, "Metamaterial enhanced arrays by innovative QCTO approaches," in *Proc. 8th European Conf. Antennas Propag. (EuCAP)*, The Hague, The Netherlands, Apr. 6, 2014.

[37] J. P. Turpin, Z. Jiang, D.-H. Kwon, P. L. Werner, and D. H. Werner, "Metamaterial-enabled transformation optics lenses for antenna applications," in *Proc. 4th European Conf. Antennas Propag. (EuCAP)*, 2010, pp. 1–5.

[38] J. Turpin, D. Brocker, and D. Werner, "Optimization of quasi-conformal transformation optics lenses with an arbitrary GRIN-capable ray tracer," in *Proc. 2013 IEEE Ant. Propag. Int. Symp.*, Orlando, FL, USA, Jul. 8, 2013.

[39] Q. Wu, J. Turpin, and D. Werner, "Quasi-conformal transformation electro-magnetics enabled flat collimating lenses," in *Proc. 2012 IEEE Ant. Propag. Int. Symp.*, Chicago, IL, USA, Jul. 8, 2012.

[40] J. A. Bossard, J. P. Turpin, and D. H. Werner, "Reconfigurable angle selective emitters in the near-IR based on phase change materials," in *Proc. 2013 IEEE Ant. Propag. Int. Symp.*, Orlando, FL, USA, Jul. 8, 2013.

[41] J. Turpin and D. Werner, "Semicircular beam-scanning metamaterial antenna with magnetic slot feed," in *Proc. 2013 IEEE Ant. Propag. Int. Symp.*, Orlando, FL, USA, Jul. 8, 2013.

[42] J. P. Turpin and D. H. Werner, "Switchable near-zero-index magnetic metamaterial for dynamic beam-scanning lens," in *Proc. 2012 IEEE Ant. Propag. Int. Symp.*, Chicago, IL: IEEE, 2012, pp. 1–2.

[43] Q. Wu, J. P. Turpin, D. H. Werner, and E. Lier, "Thin metamaterial lens for directive radiation," in *Proc. 2011 IEEE Ant. Propag. Int. Symp.*, Spokane, WA: IEEE, Jul. 2011, pp. 2890–2893.

[44] D. H. Werner, Z. H. Jiang, J. P. Turpin, and P. Werner, "Transformation optics collimating lenses for multi-beam antenna applications," in *Proc. 4th IEEE Int. Symp. Mirow. Antenna Propagat. EMC Technol. for Wirelss Communications*, Beijing, China, Nov. 1, 2011, pp. 458–461.

[45] J. P. Turpin, O. Maksomov, V. Heydemann, J. Robinson, and M. Lanagan, "Tunable interdigital capacitors at microwave frequency," in *Proc. CICMT 2008*, 2008, pp. 148–154.

[46] J. P. Turpin, Z. H. Jiang, P. L. Werner, and D. H. Werner, "Tunable metamaterials for conformally mapped transformation optics lenses," in *Proc. 2010 IEEE Ant. Propag. Int. Symp.*, Toronto, Ontario, Canada, Jul. 13, 2010.

Book Chapters

[47] J. P. Turpin, "Uniaxial metamaterials for microwave far-field collimating lenses," PhD thesis, The Pennsylvania State University, University Park, PA, May 2011.

[48] Xiande Wang, Douglas H. Werner, Jeremiah P. Turpin, and Pingjuan L. Werner, "Efficient hybrid algorithms for characterizing 3-d doubly periodic structures, finite periodic microstrip patch arrays, and aperiodic tilings," in *Computational Electromagnetics: Recent Advances and Engineering Applications*, Raj Mittra, Ed., Springer, 2013, pp. 445–486.

[49] D. H. Werner, Z. H. Jiang, J. P. Turpin, Q. Wu, and M. D. Gregory, "Transformation electromagnetics inspired lens design and associated metamaterial implementations for highly directive radiation," in *Transformation electromagnetics and metamaterials*, D. H. Werner and D.-H. Kwon, Eds., London: Springer-Verlag, 2013.

Patents

[50] "ANISOTROPIC METAMATERIAL GAIN-ENHANCING LENS FOR ANTENNA APPLICATIONS," 20,120,280,872, 2012.

Vita

Jeremiah Paul Turpin

Education

M.S. Electrical Engineering, Specializing in Electromagnetics - May 2011
The Pennsylvania State University Graduate School - University Park, PA
Thesis: Uniaxial Metamaterials for Microwave Far-Field Collimating Lenses
Advisor: Dr. Douglas Werner

B.S. Electrical Engineering, Minor in Mathematics - May 2009
Grove City College - Grove City, PA
Summa Cum Laude, Highest Honors in Electrical Engineering
Advisor: Dr. Frank Duda

Awards

- 2014 James R. and Barbara R. Palmer Fellowship in Electrical Engineering
- 2014 A. J. Ferraro Graduate Research Award
- 2014 Melvin p. Bloom Memorial Outstanding Doctoral Research Award in Electrical Engineering
- 2013 Luther B. and Patricia A. Brown Graduate Fellowship in Electrical Engineering
- 2013 Thomas and June Beaver Fund Fellowship Recipient
- 2012 IEEE Antennas and Propagation Society Doctoral Research Award
- 2012 Fred C. and M. Joan Thompson Graduate Fellowship in Electrical Engineering
- 2011 Society of Penn State Electrical Engineers (SPSEE) Graduate Fellowship
- Applied Research Laboratory (ARL) Exploratory and Foundational (E&F) Graduate Fellow
- 2010 Paul F. Anderson Graduate Fellowship in Electrical Engineering
- Roger Clark Dawes, PE Award, GCC
- GCC Scroll and Key Academic Honor Society
- Kappa Mu Epsilon, Mathematics Honorary, GCC Chapter
- Eagle Scout with Gold Palm, Boy Scouts of America
- Grove City College Dean's List

Patents

- D.H. Werner, E. Lier, B.G. Martin, J.P. Turpin, and Q. Wu, "Anisotropic Metamaterial Gain-Enhancing Lens for Antenna Applications," U.S. Patent 20,120,280,872, 2012

Distribution List

(a) Applied Research Laboratory
    The Pennsylvania State University
    Attn: Dr. Douglas E. Wolfe
    PO Box 30
    University Park, PA 16804
    Email: dew125@arl.psu.edu

(b) Defense Technical Information Center (DTIC)
    Attn: DTIC-BSC
    8725 John J. Kingman Road, Suite 0944
    Fort Belvoir, VA 22060-0944
    Email: TR@dtic.mil

(c) The Pennsylvania State University
    Attn: Douglas H. Werner
    0121 Electrical Engineering East
    Dept. of Electrical Engineering
    University Park, PA 16802
    Email: dhw@psu.edu